NISTIR 6393

Large- and Small-Scale Structures and Their Interactions in an Axisymmetric Jet

William M. Pitts[1], Cecilia D. Richards[2], and Mark S. Levenson[3]

[1]Building and Fire Research Laboratory
National Institute of Standards and Technology
Gaithersburg, Maryland 20899-8653

[2]School of Materials and Mechanical Engineering
Washington State University
Pullman, WA 99164-2920

[3]Statistical Engineering Division
National Institute of Standards and Technology
Gaithersburg, Maryland 20899-8980

United States Department of Commerce
Technology Administration
National Institute of Standards and Technology

NISTIR 6393

Large- and Small-Scale Structures and Their Interactions in an Axisymmetric Jet

William M. Pitts[1], Cecilia D. Richards[2], and Mark S. Levenson[3]

October 1999

[1]Building and Fire Research Laboratory
National Institute of Standards and Technology
Gaithersburg, MD 20899

[2]School of Materials and Mechanical Engineering
Washington State University
Pullman, WA 99164-2920

[3]Statistical Engineering Division
National Institute of Standards and Technology
Gaithersburg, Maryland 20899-8980

U.S. Department of Commerce
William M. Daley, *Secretary*
Technology Administration
Gary R. Bachula, *Acting Under Secretary for Technology*
National Institute of Standards and Technology
Raymond G. Kammer, *Director*

TABLE OF CONTENTS

LIST OF TABLES

LIST OF FIGURES

ABSTRACT

A real-time line camera system has been used to record Rayleigh light scattering along a laser beam passing radially through a propane axisymmetric turbulent jet (Re = 3960) flowing into quiescent air. The measured intensities along with a wavelet analysis designed to minimize digital noise provide quantitative measurements of propane mass fraction with sufficient temporal and spatial resolution to fully resolve the smallest scales over which turbulent concentration fluctuations occur. Direct differentiation of the data in the radial direction and use of Taylor's hypothesis to convert time derivatives to axial derivatives provide axial and radial components of scalar dissipation, χ, as a function of time. An analysis described previously in the literature, which assumes the scalar dissipation is isotropic, has allowed the pdf for $\log(\chi)$ to be determined for the jet centerline. Space-time false-color images for mass fraction, the axial and radial components of $\log(\chi)$, and the angle of the mass fraction gradient in radial-axial plane are shown for various radial locations in the jet. The experimental measurements along with critical analysis of findings from previous investigations are used to address three topics of current interest in turbulent flow studies: 1) the presence and characteristics of organized large-scale turbulent structures in axisymmetric jets, 2) quantitative values of scalar dissipation and their variation with position and flow properties, and 3) whether or not there is coupling between small- and large-scale turbulent structures in shear flows and the implications for the breakdown of Kolmogorov's hypothesis. A listing of the major findings and conclusions for each of these topics is included in the last section.

I. INTRODUCTION

The ability to characterize scalar behavior in turbulent flows has been undergoing revolutionary improvement during the past few years. As a result, a new understanding of mixing processes in these flows is beginning to emerge. In this paper an improved diagnostic for real-time multipoint measurements of concentration along a line in an isothermal, turbulent flow of two gases is described. This technique is used for measurements which, along with critical reviews of previous work, provide new insights into three of the most active areas of research in turbulent flow characterization--organized large-scale structures, scalar dissipation, and interactions between large- and small-scale turbulent structures. The current understanding of these topics is assessed. The findings of this investigation along with numerous earlier studies form the basis for a new qualitative description of mixing in axisymmetric turbulent jets.

A. Large-Scale Turbulent Structures

The presence of large-scale turbulent structures (LSTSs) and the resulting intermittent behavior in turbulent axisymmetric jets has been recognized for many years.[1,2] Intermittency here refers to the experimental observation that there are locations in turbulent shear flows where both turbulent jet fluid and ambient nonturbulent fluid are observed at different times. Another type of intermittency will be described later. Intermittency can be described in terms of the intermittency function ($I(t)$) which is defined to be one when jet fluid is present and zero when only ambient fluid is present. The time-averaged intermittency function ($\bar{I}$) is known as the intermittency factor. Investigations in fully developed axisymmetric jets of gases have shown that there is always a region of the flow near the jet centerline where $\bar{I} = 1$ (i.e., only turbulent fluid is present). As the observation point is moved away from the jet centerline towards the ambient surroundings, a location is reached where ambient fluid is occasionally observed, and $\bar{I}$ begins to decrease towards zero with increasing radial distance.

The radial extent of the jet over which intermittency is observed is substantial, typically extending from $r/(r_{½})_c = 1.0$ to 2.4.[3] Here the radial position, r, is nondimensionalized by the radial distance where the jet-fluid concentration in mass fraction terms has fallen to one half of its centerline value, $(r_{½})_c$. This range can also be expressed in terms of r nondimensionalized with the downstream distance, z, by using an experimental value for the jet spreading rate[4] and assuming that the jet virtual origin lies at $z = 0$, giving $r/z \approx 0.11$ to 0.27. According to Chen and Rodi, $r/(r_{½})_c = 1.28\, r/(r_{½})_u$ where $(r_{½})_u$ is the velocity half width.[5] The fluid consists of roughly 50 % turbulent/50 % nonturbu-

lent fluid (i.e., $\bar{I} = 0.5$) near $r/(r_{1/2})_c = 1.6$. The observation of intermittency over such a large fraction of the turbulent jet requires that large-scale structures be present in the flow.

It is well known that the observation of large-scale structures in the near-field regions of axisymmetric jets (e.g., Crow and Champagne[6]) as well as in fully developed regions of turbulent mixing layers[7] and boundary layers[8] is associated with the presence of well defined large-scale vortical motions. Such structures are often referred to as being "coherent". Here we simply refer to them as "organized". Based on their observation in other types of flows, a number of investigators have attempted to identify, or educe, organized LSTSs in downstream regions of fully developed axisymmetric jets. This has proven to be a difficult task due to the three-dimensional nature of the flow field.

Conventional point measurements (either individually or at several locations) of velocity and concentration have provided indirect evidence for organization in the developed region of axisymmetric jets. Antonia, Prabhu, and Stephenson[9], Chevray and Tutu[10,11], and Sreenivasan, Antonia, and Britz[12] considered the nature of LSTSs on the outer edges of axisymmetric jets where the flow is intermittent. They used simultaneous point measurements of temperature and velocity in conjunction with conditional sampling to show that, on average, turbulent jet fluid moves away from the jet centerline with a radial velocity which tends to first increase with distance from the jet centerline, reaching a maximum near the radial location of maximum turbulence production, before decreasing further away. At the same time, nonturbulent ambient fluid was shown to be moving towards the jet centerline with time-averaged velocities which increased substantially with decreasing radial distance, reaching nearly 7 % of the centerline velocity as the intermittency factor approached one. These findings are consistent with the suggestion of Sreenivasan and Antonia, based on joint probability functions of axial and radial velocities and temperatures, that "ejections" of high momentum jet fluid occur in the intermittency region of an axisymmetric jet.[13]

Additional conditional averaging allowed the structure for a representative LSTS of this type to be characterized.[10-12] The results can be summarized as follows: 1) the upstream and downstream edge of a LSTS move with roughly the same axial velocity, which decreases at larger radial positions, 2) over much of the radial extent of the LSTS, fluid at the downstream edges of the structure is moving radially outward at relatively high velocities which increase with radial position; however, fluid on the downstream edge of the structure nearest the jet centerline is found to be moving towards the centerline, 3) turbulent fluid on the upstream side, i.e. in the rear of the LSTS moves toward the centerline at all radial positions in the intermittent region with a velocity which decreases continuously

as the upstream edge of the LSTS is approached. These behaviors strongly suggest the presence of an organized large-scale motion.

Real-time scalar point measurements in the intermittent regions of axisymmetric jets have a distinctive appearance which has been referred to as a "ramp-like structure".[3,9,18] The time signal consists of rapid increases in concentration from the ambient level followed by a much slower fall off towards ambient values. Following a period during which ambient fluid is observed, the process then repeats. As we shall see, the presence of ramp-like structures provides an important clue to the nature of LSTS's responsible for the intermittent behavior observed in the outer regions of these jets.

Komori and Ueda performed velocity measurements simultaneously at two points in the downstream region of a heated axisymmetric jet.[14] One of the measurement locations was fixed at a radial location near the outer edge of the flow where $\bar{I} \approx 0.16$, while the second sampling position was moved around the fixed point on a grid located in the axial/radial plane. By using a conditional sampling approach in which data were only analyzed when both the radial and axial velocities at the fixed point were large and positive, pattern-averaged measurements of velocity and temperature were obtained over the grid locations. A distinct structure was educed. The downstream edge of the structure, which was inclined upstream at an angle to the centerline of roughly 30°, had radial inflow velocities at its inner downstream edge, but radial outflow velocities at its outer downstream edge. At the rear of the structure there was significant flow towards the jet centerline. Komori and Ueda concluded that strong outward motion occurs from inside the jet at an initial angle of 45° to the downstream axis. The LSTSs educed by this approach were very similar to the ejections of jet fluid discussed by Chevray and Tutu[10,11] and Sreenivasan, Antonia, and Britz[12].

Pattern-averaged measurements were also made on the opposite side of the jet (i.e., in the negative radial direction) from the fixed measurement point in order to determine whether the structures could be educed over the entire flow field. No pattern was identified, and the authors concluded that "the present coherent structure is very weak and the present structure is not similar to the coherent structure of a vortex ring observed in the near field."

Tso, Kovasznay, and Hussain used space-time correlations of up to seven hot-wire signals recorded simultaneously to infer the passage of LSTSs.[15] Two wires were located forty diameters downstream at $r/(r_{1/2})_c = 0.85$ with a 30° separation in the azimuthal direction. This places the measurement locations just inside the inner jet core where $\bar{I} = 1$. The other five hot wires were located fifty jet diameters downstream and were either aligned along the radial direction (2.54 cm spacing centered on $r/(r_{1/2})_c = 0.85$) or located at $r/(r_{1/2})_c = 0.85$ with azimuthal locations separated by 30°. Clear correlations of velocity behavior were observed at the different locations from which the

authors concluded that organized motion was present. Their findings indicated that the detected LSTSs scaled with downstream distance, were localized within one azimuthal quadrant of the flow, had a radial extent of roughly 1.71 $r/(r_{½})_c$, had a longitudinal extent of 5.1 $r/(r_{½})_c$, and were transported at 0.6 of the centerline time-averaged velocity, $\bar{U}_m$.

Later work from this group addressed a similar problem.[16] In this experiment, a rake of seven ×-wires arranged to detect the component of vorticity in the azimuthal direction was placed along the radial direction of an axisymmetric jet at equally spaced locations from 0 to 1.5 $r/(r_{½})_u$. Two additional single wires, aligned to sense axial velocities, were located at radial distances of $(r_{½})_u$ for azimuthal locations $\pm 90°$ from the array direction. The probes indicated that there were periods of time during which high levels of large-scale vorticity were observed simultaneously for the three radial locations $3/8(r_{½})_u$, $5/8(r_{½})_u$, and $7/8(r_{½})_u$. For these locations the intermittency factor should be very close to one. The occurrence of such events was taken to indicate the presence of an organized LSTS and was used to educe the flow structure.

Once a LSTS was detected, its shape was examined by considering the behaviors of space-time correlations of the longitudinal velocities at the azimuthal angles of $0°$, $\pm 90°$. Correlations were observed which indicated the passage of organized structures. The results indicated that the preferred configuration was a helical mode. The educed helical structures were found to have strong radial outward movement with axial distance, such that their size increased with the radial spreading of the jet. It was also concluded that small-scale mixing processes are most intense on the downstream edges of the LSTSs, where the structures experience strong distortion due to large strain rates aligned in the upstream direction. Axisymmetric and double-helical configuration LSTSs were also educed, however, the probability of their occurrence was much smaller than for the helical mode. A conservative estimate suggested the helical structures were present 12 % of the time, while the double helical structures were estimated as occurring up to 3 % of the time. The authors concluded that "axisymmetric vortical structures are not dynamically important in the jet far field, although they are likely to occur sometimes."

Unlike the investigation of Komori and Ueda[14] where the educed structure was almost certainly associated with a localized flow behavior occurring near the outer edge of the jet, the LSTSs discussed by Tso and Hussain appear to be associated with movements of the core jet fluid located close to the jet centerline (i.e., where $\bar{I} \approx 1$). Note that these conclusions clearly suggest the existence of at least two distinctive types of LSTSs. In order to differentiate the two types of LSTSs, those formed by ejections of jet fluid at the outer edge of the jet will be referred to as "ejected large-scale organized structures" (ELSOSs), while the second type will be referred to as "jet column large-scale organized structures"

Table 1. Types of Turbulent Structures Discussed in Text

Abbreviation	Type of Large-Scale Turbulent Stucture
LSTS	Generic large-scale turbulent structure
ELSOS	Ejected large-scale organized structure
JCLSOS	Jet column large-scale organized structure
FJLSOS	Full jet large-scale organized structure

(JCLSOSs). [Several different types of structures will be considered in this manuscript. Table 1 lists the types of structures and their abbreviations.] Interestingly, Tso and Hussain also speculated on the importance of ELSOSs, which they characterized as being of the "mushroom type". They suggested that these local ejections are responsible for significant mixing and spreading of the jet, and, in conjunction with the educed primarily helical JCLSOSs, are responsible for the majority of turbulent mixing and jet spreading.

Optical techniques such as fluorescence, Rayleigh or Raman scattering, and Mie scattering have been shown to be excellent probes of scalar behavior in turbulent flow fields. Simultaneous multipoint images of scalar fields have been used to reveal details of LSTSs in axisymmetric jets. The first of these studies was that of Dimotakis, Miake-Lye, and Papantoniou who used laser-induced fluorescence of dye in water jets to record instantaneous two-dimensional sheet images of jet fluid concentration (sheet lighting) and real-time line images of jet fluid concentration on the jet centerline.[17] These images showed that ambient fluid often reached the centerline, which should be contrasted with the results for gas jets discussed earlier. From the instantaneous images, it was clear that entrainment into the jet was occurring at isolated regions which seemed to be associated with LSTSs. These structures were shown to have either spiral or axisymmetric shapes, or to be in a transition state between these two configurations. The results suggested that jet fluid concentrations were relatively constant over large regions of space and that these regions were separated by sharp concentration gradients. The real-time line measurements indicated that the structures propagated downstream with nearly constant velocities, which were also found to jump dramatically between structures. These structures were estimated to have sizes on the order of one half of the downstream distance. The authors concluded that "mixing is not dominated by a gradient transport mechanism but rather intimately connected with the motion and dynamics of the large scales of vorticity in the flow in a manner reminiscent of two-dimensional shear layers." It is interesting that Gibson et al. had earlier

proposed a similar model for mixing in axisymmetric jets based on the observation of ramp-like structures near the centerlines of heated axisymmetric air jets.[18]

The work of Dimotakis et al. was extended by Dahm and Dimotakis[19] who studied the mixing and reaction behavior (acid/base reactions) within a water jet. This type of experiment is similar to the much earlier work of Hottel who summarized experiments in which a basic water solution containing phenolphtalein formed a jet entering acidified water.[20] The jet fluid remained colored until sufficient acid was molecularly mixed into the jet to neutralize the base, at which point the solution turned clear. Hottel showed that the images of the axisymmetric water jet had a very similar appearance to a turbulent jet diffusion flame and that the "flame length" varied in a similar manner with stoichiometry. In the extended approach of Dahm and Dimotakis, a pH-sensitive fluorescent dye is added to basic water which is used to form a jet flowing into acidified surroundings. When a light sheet interacts with the flow, only fluid having a pH greater than a certain value fluoresces, and the two-dimensional images provide a direct indication of the degree of molecular mixing.

Dahm and Dimotakis showed that the downstream end of the reaction region varied quasi periodically. Isolated regions of unreacted jet fluid were observed to break away from the main flow and move downstream. A given stoichiometric condition in the separated fluid would be reached nearly instantaneously over a region of space extending roughly one local jet diameter, L_{jd} (estimated as 0.4 of the downstream distance, z, by the authors), in both the radial and axial directions. This was taken as additional evidence that there are large regions of space with nearly constant concentration in these flows. It was noted that the reaction tended to proceed from upstream to downstream regions, which was attributed to the fact that entrainment takes place at the upstream ends of LSTSs.

Real-time line measurements of concentration across the jet showed that the time-mean radial concentration profile is a poor representation of the instantaneous concentration field. Indeed, the instantaneous radial profiles seemed to fall into two general types. One had a top-hat character in which the concentration was relatively constant across the entire instantaneous jet width and fell sharply at the outer edges, and the second had a central region with a relatively high concentration and two outer wings of somewhat lower concentration. These observations led the authors to propose an idealized conceptual picture for the instantaneous concentration field, shown schematically in Figure 7 of their paper, which consists of a number of nested axisymmetric LSTSs each of which has a size of roughly L_{jd} and nearly constant concentration. A similar "cartoon" appears in the earlier work of Gibson et al.[18] Since the time-averaged concentration decreases with downstream distance, the relatively constant concentration within a LSTS is lower for structures located further downstream. This model requires sharp concentration gradients between adjacent LSTSs. For a given downstream

distance, the estimated passage time for these structures is $L_{jd}/\bar{U}_m$. As in the earlier study, unmixed ambient fluid was detected deep in the jet core. The amount of ambient fluid on the jet centerline was shown to be a decreasing function of Reynolds number.

This view of LSTSs in axisymmetric jets differs substantially from that discussed above with regards to ELSOSs and JCLSOSs. The mixing behavior at both the jet outer edge and in the core region is viewed as being due to a single type of LSTS which extends over the full jet width. In order to emphasize this difference, this type of LSTS will be referred to as a "full jet large-scale organized structure" (FJLSOS).

A second paper by Dahm and Dimotakis provides additional discussion of FJLSOSs.[21] The authors argue that the general conclusions of the earlier papers are correct, but note that helical modes seem to be more important than suggested by their idealized conceptual model of the concentration field[19]. They also note that "the organization in the jet far field appears to be both topologically and dynamically more complex than that in turbulent shear layers, and may be a consequence of the fact that the jet is simultaneously unstable both to axisymmetric and helical modes, and appears to alternate between these two."

Shlien used planar imaging of laser-induced fluorescence from water-borne dyes to obtain a different view of mixing in axisymmetric jets.[22] In his experiments a flow of dyed water scaled to match the expected entrainment flow rate of the ambient fluid was generated well outside of the jet. The dyed fluid was drawn towards the jet, entrained, and distributed by turbulent mixing. Time-resolved planar imaging of the dye in the entrained fluid provided insights into the entrainment behavior as well as the mechanisms for turbulent mixing of ambient fluid by the jet. Photographs showed that the ambient fluid was initially drawn relatively slowly towards the jet before being rapidly ingested and accelerated by the flow. Shlien argues that this behavior is indicative of engulfment at the upstream edges of LSTSs. The region of entrainment and rapid acceleration was located near a nondimensionalized radial position of $r/z = 0.2$, and the fluid was accelerated nearly instantaneously to $r/z = 0.1$. Ambient fluid was observed to cross the jet centerline at a distance of roughly $1.5(r_{1/2})_u$ downstream of its release. With further increases in downstream distance the ambient fluid tended to spread inwards relatively slowly towards the jet centerline, but, significantly, the vast majority of the fluid was still located on the side of the jet where entrainment had occurred even after the flow had traveled downstream a distance comparable to several large-scale diameters.

An extensive investigation by Papantoniou and List considered mixing in downstream regions of axisymmetric water flows dominated by either the initial jet momentum or by buoyancy.[23] Both instantaneous two-dimensional and real-time line images along axial and radial directions were

recorded. For the momentum-dominated jets of interest for this discussion, the results supported the conclusions of the earlier studies in water jets discussed above. Instantaneous two-dimensional images identified a central conical region of the jet where concentrations were relatively uniform and at a higher concentration than the surrounding fluid. This region of the flow was observed to vary in time with a high degree of regularity.

Instantaneous radial profiles of concentration were very different than the time-averaged profiles, but only twenty-five independent realizations were required to reproduce the time-averaged results. Real-time line measurements of concentration were plotted on a two-dimensional radial coordinate-time axis using a false-color scale to represent concentration. The color scale was chosen to emphasize three concentration ranges in order to try and identify the passage of FJLSOSs near the jet centerline. The lowest concentration fluid was generally observed on the outer edges of the flow or nearer the centerline at the upstream edges of FJLSOSs. Fluid at intermediate concentrations was typically found near the centerline and was present during a large fraction of the time. The highest concentration fluid occurred infrequently near the centerline at the downstream edges of FJLSOSs. Note that these observations suggest the existence of ramp-like structures on the jet centerline which are similar to those discussed above for the intermittent region of gas jets and that very rapid concentration changes should be observed as the interfaces between FJLSOSs pass by. To differentiate the two types of ramp-like behaviors, which are expected to result from different physical processes, the structures now under discussion will be referred to as "internal ramp-like structures".

An ensemble-averaging technique similar to that developed by Sreenivasan et al.[12] was used to educe the form of the LSTSs near the centerline. These ensemble-averaged structures indeed had a ramp-like appearance. The results of these time-resolved measurements are not inconsistent with the earlier conclusion of Dahm and Dimotakis[19] that similar jets have relatively constant instantaneous concentrations over a large region of the flow. In fact, due to entrainment at upstream edges of FJLSOSs, the concentration within FJLSOSs would continually decrease in time as they move downstream and would appear similar to those described by Panpantoniou and List as they pass a given axial location.

The time-resolved data were used to calculate autocorrelation functions at single locations as well as cross-correlation functions for different radial locations. Distinct peaks were observed in these correlations at periods corresponding to the passage time for the large structures (defined in the same way as before as $L_{jd} = 0.4\,z$ divided by $\bar{U}_m$). These results represent perhaps the strongest evidence yet discussed for the existence of FJLSOSs in these flows. Using the correlation results, values of the

integral timescale and lateral spatial scale were also calculated. The resulting integral scales were on the order of 10 % of L_{jd}.

In two-dimensional axial coordinate-time images the propagation of LSTSs can be clearly seen. Locally, these structures have a nearly constant downstream propagation velocity which seems to undergo abrupt changes similar to those observed in the concentration field. These findings are in general agreement with those reported by Dimotakis et al.[17], but Papantoniou and List conclude that the observed structures are roughly twice as large.

Additional differences between the findings of Papantoniou and List and Dahm and Dimotakis should be noted. First, the former authors found that jet-fluid concentration at the jet edges tended to be significantly lower, while Dahm and Dimotakis suggest the radial concentration profiles either are roughly constant all the way across the jet or have two levels. The later work also led to the conclusion that helical FJLSOSs dominate as opposed to the axisymmetric structures observed by Dahm and Dimotakis.

The multi-point measurements discussed thus far were for liquids. Similar techniques have recently been applied to gases. Pitts has reported limited real-time line measurements of concentration in propane axisymmetric jets.[24,25,26] These showed that the concentration fluctuations responsible for the ramp-like structures observed in single-point, real-time concentration measurements at the outer edges of axisymmetric jets are due to LSTSs which extend radially across the entire intermittency region. It was argued that these structures are formed by the ejection of highly concentrated jet fluid from the jet core (i.e., that they are ELSOSs) and that large amounts of air are entrained at the upstream edges of these structures. In the radial-coordinate/time plots, concentration isoplets on the downstream edges of the LSTSs were observed to run parallel to each other over large radial distances, suggesting a great deal of organization in the flow with a corresponding lack of small-scale structure. The maximum concentration across a downstream edge of a given ELSOS fell with increasing radial position. On the rear (upstream) sides of the structures, the concentration was much more diffuse and the parallel concentration isopleths were not observed, suggesting that a different mechanism was responsible for mixing at these locations. Simultaneous plots of concentration and axial velocity indicated that signatures for the ELSOSs were evident in both across the intermittent region of the flow field. Evidence was presented suggesting that jet fluid ejected to the far edges of the flow field can occasionally lose its momentum and be temporarily separated from the jet, before being reentrained at a later time.

van Cruyningen et al. recorded instantaneous two-dimensional fluorescence images of a nitrogen jet seeded with biacetyl.[27] The images had similar properties to those reported for liquid

jets.[19,21,23] Radial cuts tended to have a relatively constant concentration near the centerline and sharp fall offs in concentration near their radial edges. Instantaneous radial profiles were very different than the expected time-averaged profile. The centerline cut of the image had lengths of relatively constant concentration separated by sharp concentration changes.

Schefer et al. recorded 1000 instantaneous images of the two-dimensional concentration field for an axisymmetric jet of methane.[28] Their results were similar to the studies discussed above which were the basis for the hypothesis concerning the presence role of FJLSOSs in jets. For instance, instantaneous radial profiles had very different shapes from time-averaged profiles. Large areas of the flow had relatively constant jet-fluid concentrations, and interfaces between these areas were separated by sharp concentration gradients. Images were observed which were consistent with the presence of both axisymmetric and helical structures. Axisymmetric structures were identified in 40 % of the images, while helical structures were present 30 % of the time. The remaining images provided no clear indication of FJLSOSs. Time averages, root-mean-square (rms) values, and probability distribution functions (pdfs) for mass fraction over the imaged region were consistent with the known self-similar behavior of the jet. The authors concluded that FJLSOSs are vortical in nature and are responsible for a large fraction of entrainment into the jet.

Mungal and coworkers have discussed the presence of FJLSOSs in axisymmetric jets in a series of publications.[29,30,31,32,33,34] In two of these studies, sequential motion pictures of high Reynolds number (*Re*) turbulent jets [one was an acetylene flame ($Re = 76{,}000$)[30] and the second was the exhaust of a rocket motor ($Re = 2 \times 10^8$)[29]] were used to demonstrate that organized motion could be visualized and tracked along the outer edges of these flows. These flows had sufficiently high Re to remain momentum dominated over the entire downstream distance observed. For the case of the combusting acetylene jet, a similar quasi-periodic burn out at the flame tip was found as discussed by Dahm and Dimotakis for water jets[19] even though there was also evidence for the presence of a spiral mode in the flame which occurred with a high probability. The authors provided a schematic diagram for mixing due to the spiral mode which was analogous to that drawn by Dahm and Dimotakis for the axisymmetric mode.[19] The high Re of the flows studied allowed the conclusion that the FJLSOSs are a characteristic of fully developed turbulent flow and not the result of a transition phenomenon.

van Cruyningen et al. introduced volume rendering in order to characterize FJLSOSs in real-time flow visualizations.[31] In this approach real-time two-dimensional images are digitized and then stacked into a three-dimensional object which is viewed using computer graphics techniques. LSTSs appear in the images as a series of ridges and valleys which extend along the edge of the structure.

Volume rendering of the images of turbulent ethylene jet flames was shown as part of a demonstration of the technique.

Volume rendering was used to investigate turbulent jet flames of acetylene and ethylene. Different initial flow velocities were used so that the resulting flows were dominated by either the initial jet momentum or the combustion-induced buoyancy.[32] As above, distinct peaks and valleys were discernible on the surfaces of the rendered volumes which were taken as evidence for the presence of organized FJLSOSs. Two major findings of this investigation were particularly surprising. First, it was possible to track individual structures over a large fraction of the flame lengths (roughly 220 times the initial jet diameters). The ends of the flames displayed the same organized periodic variations observed earlier, and the authors concluded that "tip burnout is the culmination of an event which started in the earliest portions of the flow field." The second surprising finding was that the FJLSOSs appeared to move down the flames with a nearly constant velocity (12 % of the initial jet velocity) instead of showing the expected velocity decay. Three possible causes for such an observation were discussed. The temporal behavior of the flame tips was analyzed, and it was shown that the oscillation rates were comparable to a time scale based on the passage of large-scale structures, again consistent with the conclusions of earlier investigations.

The volume rendering approach was also applied[33] to the very high Re cases of the rocket motor firing described above[29] and a large hydrogen jet diffusion flame. In the case of the nonreacting rocket plume, structures were again observed which seemed to exist over a large fraction of the total length of the observed jet. However, in this case the velocities of the structures decreased with the inverse of the downstream distance as expected, while the size of the structures grew with downstream distance. There were limited indications of pairing of the structures. The images suggested the presence of both axisymmetric and helical modes in the flow. The hydrogen flame also had distinct bands in the visualized structure, but as observed for the acetylene and ethylene turbulent jet flames discussed above, the structures appeared to move with a constant velocity.

Yoda et al.[34] recorded real-time two-dimensional fluorescence images of natural, circularly forced, and axially forced water jets in a manner similar to Dimotakis et al.[17] The resulting images were then analyzed using volume rendering. Once again, structures were observed which could be tracked nearly over the full axial extend of the imaged jet and were attributed to FJLSOSs. Cross-correlation techniques were used to identify axisymmetric and helical structures. Both types of structures were evident in the natural jet, but forcing of either type seemed to favor the observation of helical structures.

In 1991, Broadwell and Mungal reviewed the existing evidence concerning FJLSOSs in axisymmetric jets.[35] Based on their review they proposed a simple model for molecular mixing in these flows which consists of two stages. In the first stage, mixing takes place in the Taylor layers formed along the edges of the FJLSOSs where entrainment into the flow is occurring. This entrained fluid ultimately enters the inner region of the jet, which is viewed as a uniform, well mixed region. The model can be extended to reacting flows, in which case reaction takes place in two environments--a diffusion layer corresponding to the Taylor layers and a perfectly stirred reactor corresponding to the well mixed region. This simple mixing model allows detailed chemical kinetic models to be applied to turbulent reaction problems. No results of modeling axisymmetric jets were discussed, but results for plane mixing layers using a similar approach were encouraging.

Very recently, Yoda et al. have reported a study which has dramatically altered their view of FJLSOSs.[36] These measurements involved three-dimensional measurements of the concentration field in a dyed water jet using a planar laser-induced fluorescence technique in which the plane is rapidly scanned in the third dimension. This approach is similar to that first introduced by Dahm and coworkers to investigate small scale features of turbulent jets,[37,38] but the spatial resolution was degraded to allow imaging of the entire jet volume. Natural, circularly forced, and weakly buoyant jets having Re from 1000 to 4000 were studied. Various analysis procedures including two-dimensional cuts through the volume, three-dimensional views of isoconcentration surfaces, calculation of concentration centroid locations along the downstream direction, and cross-sectional areas of isoconcentration surfaces as a function of downstream distance were employed in an attempt to characterize the FJLSOSs. Instantaneous concentration volumes were chosen for analysis which seemed to offer the best opportunities to observe helical structures.

To the evident surprise of the authors, they were unable to identify obvious helical structures in their measured concentration data. In fact, it was often found that when a particular two-dimensional cross-sectional cut had a helical appearance, there were cuts with different views (e.g., with the observation plane rotated 90° about the centerline) for which the structure appeared to be axisymmetric. Likewise, there was no indication of helical structures in the concentration centroids. On the contrary, the centroid measurements provided evidence that the overall motion was simply a waving back and forth of the jet. Interestingly, the cross-sectional concentration area measurements did suggest the presence of FJLSOSs with roughly uniform concentration which decreases with downstream distance. Regions between these areas typically had much lower concentrations. The authors concluded that the developed region of a turbulent jet is "not in the form of an expanding spiral, but instead appears to be in the form of a sinusoid, even when two-dimensional slices of the

data are clearly antisymmetric in shape." In order to explain the observations, it was proposed that the FJLSOSs have the form of a double helix (i.e., paired ± 1 helices). This represents a dramatic change of view from earlier work.

B. Scalar Dissipation

Another aspect of turbulent mixing which is receiving a great deal of study is scalar dissipation behavior. Scalar dissipation is the parameter which characterizes the rate of molecular mixing in a flow field. It is most often defined* as

$$\chi = 2D\nabla\xi\bullet\nabla\xi \ , \tag{1}$$

where D is an appropriate universal molecular diffusion coefficient and ξ is a conserved scalar, known as the mixture fraction, which is equal to the mass fraction for isothermal mixing of two fluids. There have recently been a number of attempts to measure values of scalar dissipation in turbulent axisymmetric jets. This interest is motivated not only by a desire to characterize this fundamental turbulence property and model its behavior, but also by the central role this parameter plays in models for turbulent combustion.

The most widely employed model for turbulent jet diffusion flames is the laminar flamelet concept.[39] In this approach turbulent combustion is viewed as occurring along stoichiometric contours embedded within the turbulent flow field. Burning along these contours takes place as one-dimensional laminar flames subject to the local stretch introduced by turbulent velocity fluctuations. The scalar dissipation is often employed to characterize the effects of flame stretching. Thus the two most important parameters for laminar flamelet modeling are the local mixture fraction and the scalar dissipation at the stoichiometric contour. Recently, Bilger[40] has argued that turbulent combustion is more likely to occur in broadened reaction zones which have turbulence embedded within. He suggests that such reaction behavior can be modeled if the local mixture fraction and scalar dissipation are known.

It has proven exceedingly difficult to measure mixture fraction and scalar dissipation within turbulent jet diffusion flames. For this reason, it is necessary to attempt to characterize their behavior in nonreacting flows and extend the findings to turbulent combustion systems. Most advances in the understanding of turbulent combustion have occurred in this manner. Very recently, researchers have

---

*χ is also often defined without the factor of 2 shown in Eq. (1).

even attempted to characterize the structure of chemically reacting turbulent flows by superimposing reacting fields on constant temperature images of turbulent mixing.[40,41]

Peters and Williams provided a short, but illuminating, summary of the state of knowledge concerning scalar dissipation in turbulent flows in 1983.[42] They concluded that the theoretical basis for predicting values of average scalar dissipation was available, but untested. Only a single experiment had been reported which attempted to measure scalar dissipation.[43]

Since Peters and Williams' assessment a number of investigations have been reported in which scalar dissipation values have been estimated based on measurements of one or two of the three components of the full three-dimensional values.[41,44,45,46,47,48,49,50,51,52,53,54,55,56,57,58] Findings of these individual investigations will be detailed in the Discussion section. Here the focus is on the various experimental approaches which have been employed and the spatial resolution requirements for scalar dissipation measurements.

Complete characterization of an instantaneous value of χ requires the simultaneous measurement of the three spatial components for the gradient of mixture fraction. For a time-averaged axisymmetric flow field, a natural Cartesian axis system is based on the axial (z), radial (r), and azimuthal (a) directions. The origin is defined as being at the center of the jet exit. The aximuthal axis corresponds to the tangent of the circle formed by the azimuthal angle in a cylindrical coordinate system. In terms of the Cartesian coordinate system, Eq. (1) can be rewritten as

$$\chi = \chi_z+\chi_r+\chi_a = 2D\left[\left(\frac{\partial \xi}{\partial z}\right)^2+\left(\frac{\partial \xi}{\partial r}\right)^2+\left(\frac{\partial \xi}{\partial a}\right)^2\right], \qquad (2)$$

where χ_z, χ_r, and χ_a are the scalar dissipation components along the axial, radial, and azimuthal directions, respectively.

Accurate measurement of the three components of χ simultaneously in a turbulent flow field provides a severe technical challenge. Not only must time-resolved measurements be made in three dimensions, but the measurements must be sufficiently accurate and spatially resolved to measure concentration changes over the smallest distances where fluctuations occur. Dahm et al. have demonstrated time-resolved, three-dimensional measurements of concentration in water flows and have used the results to calculate instantaneous scalar dissipation fields.[37,38,47,59] As discussed below, their spatial resolution may have been insufficient to fully resolve the entire scalar dissipation probability density function (pdf). Prasad and Sreenivasan[60] and Kailasnath et al.[61] reported similar measurements, but their spatial resolution was considerably degraded from that used in the experiments of Dahm et al. While preliminary efforts have been made to develop three-dimensional imaging using two laser sheets

for the gaseous flows of interest to the current investigation,[62,63,64] only limited quantitative measurements have been reported.

All gas-phase values of χ reported thus far are actually estimates based on measurements which did not simultaneously measure all three components. Approximations have been invoked whose effects have not always been fully recognized. The earliest estimates for χ were based on measurements of a single component. Lockwood and Moneib[43] used real-time temperature measurements for two closely spaced positions in a heated axisymmetric air jet to derive time-averaged spatial gradients for the axial and radial directions. (Note that for the purposes of this paper temperature in mildly heated flow fields will be treated as a passive scalar.) Data were simply reported as the square of the gradient.

Dibble et al. recorded instantaneous line measurements of mass fraction along the radial direction of a propane jet flowing into air using Rayleigh light scattering.[44] By averaging a large number of such measurements, time-averaged values for χ_r, $\overline{\chi}_r$, were calculated. In order to obtain an estimate of the full scalar dissipation they made the assumption that the scalar dissipation was isotropic and estimated $\overline{\chi}$ as

$$\overline{\chi}_e = 3\overline{\chi}_r \quad , \tag{3}$$

where $\overline{\chi}_e$ indicates an estimated value of $\overline{\chi}$.

Namazian et al. used two-dimensional Raman images to make instantaneous measurements of mass fraction for an axisymmetric jet of methane from which instantaneous values of χ_z and χ_r were calculated.[28,46] Multiple measurements allowed means, rms, pdfs, and correlation coefficients for the scalar and its dissipation to be calculated throughout the imaged region.[46] In order to estimate $\overline{\chi}_e$, the authors assumed $\overline{\chi}_a = \overline{\chi}_r$ and that the two components were uncorrelated to yield

$$\overline{\chi}_e = \overline{\chi}_r + 2\overline{\chi}_r \quad . \tag{4}$$

Namazian et al. considered the spatial resolution necessary to fully resolve the concentration gradients in their flow field.[46] They assumed the required resolution was equal to the Kolmogorov length scale, η_K (see ahead). Their spatial resolution was only sufficient to a resolve a length ten times longer than η_K. An attempt was made to correct their measurements for limited spatial resolution using an argument based on the results of Corrsin and Uberoi[65] for the scalar variance spectra. Estimates were provided for the uncertainty in individual as well as time-averaged scalar dissipation measurements due to noise in the measurements.

Feikema and Driscoll used Rayleigh light scattering to record instantaneous two-dimensional images of jet-fluid concentration for a propane axisymmetric jet entering air which allowed $\overline{\chi}_z$ and $\overline{\chi}_r$ values to be calculated.[48] Instead of making an assumption concerning the behavior of χ_a, they only reported two-dimensional results (here denoted as χ_p). Correlations of concentration and the two-dimensional χ_p were also reported. In later work from the same group, Feikema et al. used an instantaneous form of Eq. (4) to estimate values of χ from time-resolved planar concentration measurements.[56]

Effelsberg and Peters used real-time Rayleigh light scattering concentration measurements at two closely spaced locations along the radial direction to estimate values of scalar dissipation for an axisymmetric jet of propane into air.[45] Since only values of χ_r were measured, two assumptions were used to estimate values of $\overline{\chi}_e$. The first was $\chi_r = \chi_a$. The second was to invoke Taylor's hypothesis and estimate χ_z using

$$\frac{\partial \xi}{\partial z} = \frac{1}{\overline{U}}\left(\frac{\partial \xi}{\partial t}\right), \tag{5}$$

where $\overline{U}$ is the average axial velocity at the radial location and t is time, to yield

$$\chi_e = 2\chi_r + \frac{2D}{\overline{U}^2}\left(\frac{\partial \xi}{\partial t}\right)^2 . \tag{6}$$

Antonia and Mi have employed parallel cold wires to measure each of the three components of the scalar dissipation independently for a slightly heated axisymmetric jet.[50] These authors found that for a single centerline location in the similarity region that the time-averaged radial and azimuthal components were nearly equal and that the axial component was only slightly smaller. Similar findings for heated flows have been reported by Anselmet et al.[51] and Tong and Warhaft[53].

There are two aspects concerning experimental estimates of χ which have caused a great deal of confusion in the literature. These are the spatial resolution required in order to fully resolve the gradients in concentration and the appropriateness of using measurements of scalar dissipation components for one or two dimensions to estimate $\overline{\chi}$ or $\overline{\log(\chi)}$.

In order to accurately measure a spatial concentration gradient, it is necessary to have sufficient spatial and temporal resolution to ensure that the concentration gradient is effectively constant in space and time during the measurement. In other words, spatial fluctuations in the concentration gradient must occur on scales larger than the measurement volume and the product of the

measurement time and local velocity. Similar criteria apply for measurements of individual components of χ.

Most attempts to estimate the spatial resolution required are based on analogies with measurements of turbulent energy dissipation. The smallest scales on which velocity gradient fluctuations occur are believed to scale as the Kolmogorov scale, η_K, defined as

$$\eta_K \equiv \left(\frac{\nu^3}{\bar{\epsilon}} \right)^{1/4}, \tag{7}$$

where $\bar{\epsilon}$ is the average rate of turbulent energy dissipation and ν is the kinematic viscosity. The corresponding length scale for scalar fluctuations is the Batchelor scale which is defined as[66]

$$\eta_B = \eta_K Sc^{-1/2} , \tag{8}$$

where Sc is the Schmidt number given by the ratio of kinematic viscosity and molecular diffusivity, ν/D.

Values of $\bar{\epsilon}$ are often estimated as

$$\left(\bar{\epsilon}\right)_e = \left(\frac{U'^3}{\ell} \right), \tag{9}$$

where U' is the rms for the axial velocity fluctuations, and ℓ is a characteristic large scale. Equation (9) is derived assuming that turbulent energy generation which takes place in large-scale, inviscid turbulent structures is equal to energy dissipation at the smallest turbulent scales. Substitution of Eq. (9) into Eq. (7) allows values of the Kolmogorov scale to be calculated as

$$\left(\eta_K\right)_e = \left(\frac{\nu}{U'} \right)^{3/4} \ell^{1/4} = Re_\ell^{-3/4} \ell , \tag{10}$$

where $Re_\ell = U'\ell/\nu$ is the local turbulent Reynolds number. Thus the spatial resolution necessary to resolve the smallest spatial scales for turbulent scalar fluctuations is proportional to Eq. (10) and can now be written as

$$\lambda_r = C \left(\frac{\nu}{U'} \right)^{3/4} \ell^{1/4} Sc^{-1/2}. \tag{11}$$

Values of $\bar{\varepsilon}$ can be obtained directly from closely spaced velocity measurements. However, since velocity measurements are often unavailable, $(\bar{\varepsilon})_\ell$ is frequently estimated using an appropriate

large scale of the flow field and Eq. (9). Unfortunately, a variety of scales have been used for ℓ in the literature. Throughout this paper values of ℓ will be defined as the velocity half radius, $(r_{1/2})_u$. Where appropriate, values of η_B from other studies will be estimated in the same manner. Values of U_m' are taken from experimental measurements on the jet centerline available in the literature. With these approximations, it is now possible to consider the experimental evidence for the appropriate value of C to use in Eq. (11).

In most early work in this area it had been assumed that $C \approx 1$. Some experimental support for this conclusion was available. For instance, Gibson et al. showed that the third-order structure function did not converge to the skewness of the temperature gradient until the separation of the two probes used for the measurement was reduced to a value very nearly equal to the Kolmogorov scale.[18] However, a recent study by Dowling and Dimotakis led to a different conclusion.[67] In an experiment designed to fully temporally and spatially resolve the scalar fluctuations in an axisymmetric jet of ethylene flowing into nitrogen, they reported that $C \approx 13.5$ based on the location where spectral analysis of concentration fluctuations showed a break in the spectral falloff behavior. Dahm and coworkers employed this finding to estimate the resolution required to fully resolve concentration gradients.[37,38] Note that the analysis of the latter study is performed in terms of a length scale which is roughly one half of η_B and, as a result, they actually used a value of 25 in their expression. In later work[41] this value was reduced by roughly one half (approximately $5\eta_B$) based on measurements reported in Buch and Dahm[47] and later independently measured by Southerland and Dahm[59]. Building on the work of Dowling and Dimotakis as well as literature measurements of velocity spectra, Miller and Dimotakis argue that the constant in Eq. (11) should actually equal 25.[68] One or the other of these larger estimates for C has been cited recently by a number of researchers trying to estimate the required spatial resolution for scalar measurements in lifted turbulent jet diffusion flames[69] and axisymmetric[56,70,71] and planar jets[72].

If the value for C were actually as large as suggested above, it would have significant practical importance since the spatial and temporal resolution requirements for a given experiment could be greatly relaxed compared to requiring $C \approx 1$. Unfortunately, recent experiments have shown that the suggestion that C is significantly greater than one is incorrect. Lozano et al. used two-dimensional planar images of biacetyl fluorescence doped into an axisymmetric jet to show that the smallest scales on which gradient variations were observed corresponded to $C \approx 2$.[73] Significantly, in an earlier discussion of similar measurements from the same group, it had been suggested that a much larger value of C might be appropriate.[27] Antonia and Mi considered the effects of spatial separation of two cold-wire probes used for temperature gradient measurement and found that small corrections were still

required for spatial averaging when a probe separation corresponding to $C \approx 2$ was used.[50] Work by Anselmet et al.[51] and Tong and Warhaft[53] support this finding. It is significant that based on an extended analysis of the data presented by Dowling and Dimotakis[67], Dowling[49] concludes that the original estimate of $C \approx 13.5$ should be reduced by a factor of 4 or 5. Taken together, these studies support earlier hypotheses that the spatial resolution should be very close to η_B (a value of $2\eta_B$ would seem to be a maximum) in order to fully spatially resolve scalar dissipation fluctuations for flows with $Sc \approx 1$. It is important to note that a value of $C \approx 2$ is consistent with the spatial resolution required for analogous measurements of energy dissipation in air flows.[74,75,76,77]

As discussed above, values of λ_r are often estimated using Eq. (11). For practical estimates of spatial resolution requirements it is important to characterize how well estimates for η_K, which are incorporated into Eq. (11), match actual values of η_K based on Eq. (7). Dowling and Dimotakis[49,67] calculated values of η_K along the centerline of an axisymmetric jet using an estimate for $\bar{\epsilon}$ taken from Friehe et al.[78],

$$\bar{\epsilon} = 48\frac{U_o^3}{d_o}\left(\frac{z-z_o}{d_o}\right)^{-4}, \tag{12}$$

where U_o is the jet exit velocity, d_o is the jet exit diameter, and z_o is a virtual origin. Antonia and Mi[50] used measured values of $\bar{\epsilon}$ to calculate a centerline value of $\eta_K = 0.17$ mm for $z/D_o = 30$ in an air jet. Assuming $z_o = 0$ and using Eq. (12) along with Eq. (7) yields $\eta_K = 0.18$ mm, which is in excellent agreement. Antonia and Mi also report values of U_m' and $(r_{1/2})_u$ for this downstream distance which allow an estimate of $\eta_K = 0.20$ mm using Eq. (9). The close agreement of this estimated value with the η_K calculated using values of $\bar{\epsilon}$ substituted directly into Eq. (7) shows that Eq. (10) with $\ell = (r_{1/2})_u$ provides accurate estimates for η_K. Thus Eq. (11) with $C \approx$ 1-2 should provide valid estimates for the spatial resolution required to make accurate measurements of χ.

Equations (3), (4), and (6) have been used to estimate $\bar{\chi}$ from scalar measurements in one or two dimensions. Dahm and Buch[79] and Dowling[49] have pointed out that pdfs, averages, and higher moments for estimated values of $\log(\chi)$ derived from one- and two-dimensional measurements are biased toward low values. This bias is the result of instantaneous measurements of one or two components of χ yielding zero or near-zero values when the actual value of χ may well be much greater than zero. Dahm and Buch provided a mathematical method, based on assumed isotropy for the three components, for correcting the bias in single- and two-component measurements of χ which allows corrected pdfs and moments for $\log(\chi)$ to be calculated.[47,79] Their estimates suggest that the bias in estimates based on single-component results can lead to an underestimation of $\overline{\log(\chi)}$ by a factor of 7,

with much smaller differences for two-component measurements. The potential need for such corrections must be kept in mind when utilizing estimates of $\overline{\chi}$ or $\overline{\log(\chi)}$ based on measurements along one or two spatial directions.

C. Small-Scale Structure and Interactions Between Large- and Small-Scale Structures

Much of the extensive history of the experimental characterization of scalars in turbulent shear flows has been fueled by efforts to confirm predictions of Kolmogorov's hypotheses concerning the universality of the structure of small-scale velocity[80] and its implications for small-scale scalar fluctuation behavior[81,82]. A recent review of small-scale structure in turbulent flows had been presented by Sreenivasan and Antonia.[83]

One of the principal requirements of small-scale universality is that the skewness of the scalar gradient pdf should be zero. However, numerous investigations have found that the skewness is nonzero (e.g., for axisymmetric jets see Gibson et al.,[18] Sreenivasan et al.,[12] and Pitts and Kashiwagi[3]). The nonzero skewness values have been attributed to the internal ramp-like structures discussed above which occur in regions of the jet where $\overline{I} = 1$. It is the sharp concentration increases associated with the edges of these structures which lead to the finite skewness for the gradient of the scalar field. Since the edges of the ramps in axisymmetric jets are oriented such that the sharp scalar increases occur in the upstream direction, the contribution to the axial component of the gradient is negative, and the resulting skewness has a negative value. The sign of the skewness varies depending on the type of shear flow.

Note that the existence of internal ramp-like structures requires that some mechanism for direct coupling between large and small scales exist. This conclusion is inconsistent with Kolmogrov's hypothesis. Both Gibson et al. and Sreenivasan et al. speculated that the development of the internal ramp-like structure was due to interactions of the scalar field with large scale features of the velocity field (either the mean shear[12] or strain between large eddies having the mean vorticity[18]).

In 1991, Sreenivasan published an influential review of the existing experimental evidence concerning local isotropy in turbulent flows.[84] In addition to the skewness behavior discussed above, he also considered measurements of structure functions for both velocity and scalars, as well as velocity and scalar spectra. He concluded that 1) there is unlikely to be an asymptotic state for small-scale behavior, 2) isotropy of small scales is not to be expected, 3) the small scales tend to be organized over much larger distances than the Kolmogorov scale, 4) structures of very disparate scales can interact directly with each other, and 5) the mechanism for the formation of elongated structures appears to involve direct interactions with either the mean or large-eddy strain rates. Sreenivasan also

discussed the relationship between the ramp-like structures and observations of small-scale structure. He noted that for positions away from the centerline, the edges of the ramps (presumably formed by LSTSs, using the nomenclature of the current paper) are aligned roughly at 135° to the downstream flow direction. Particularly relevant for the discussion which follows, he speculated that this observation is connected with the orientation of the principal strain axis for the corresponding two-dimensional time-averaged flow field which lies along the same direction.

Another manifestation of small-scale anisotropy which has recently received considerable attention is its possible effects on the pdfs for the velocity and scalar as well as their spatial derivatives. In certain turbulent flows (e.g., Castaing et al.,[85] Gollub et al.,[86] Jayesh and Warhaft[87,88]), scalar pdfs have been observed in which the wings are stretched out compared to the expected Gaussian distribution. Similarly, pdfs for scalar gradients do not always display the expected log-normal form, but sometimes have tails which fall more slowly. Modeling studies have also shown that such behaviors are to be expected under certain conditions (e.g., Holzer and Siggia,[89] Pumir,[90] McLaughlin and Majda,[91] Jaberi et al.,[92] Overholt and Pope[93]). To the knowledge of the current authors, these behaviors have not been observed in axisymmetric jets.

Another important concept regarding interactions between small- and large-scale structures in turbulent flow is dissipation or small-scale intermittency. Here the discussion of Sreenivasan and Antonia is followed.[83] Obukhov has attributed the failure of Kolmogorov's hypothesis to a "change of the large scale processes".[94] As a result, the instantaneous local small-scale structure is related to the recent time history and current structure of the surrounding large-scale structure and changes with time as the local large-scale structure varies. These variations in small-scale structure are referred to as dissipation intermittency and represent a mechanism for violation of Kolmogorov's hypothesis. The term "small-scale intermittency" will be used here to differentiate this type of behavior from intermittency at the outer edge of the jet due to the presence of LSTSs.

Recent experimental measurements have revealed that the scalar small-scale structure in axisymmetric jets consists of distinctive sheet-like structures for both liquid (large Sc[38,47,59,84]) and gas ($Sc \approx 1$[47,57]) flows. The small-scale scalar structure signatures are quite different for the two types of jets. For high Sc flows the sheets have little curvature over distances much greater than their thickness. Several adjacent layers, which run parallel to each other, are generally observed. For gas flows, Buch and Dahm find that the layers are much more distorted, having radii of curvature which vary over a few sheet thicknesses.[47,57] In general, nearby sheet-like structures have significantly different orientations. While not emphasized by Buch and Dahm, their two-dimensional images for the gas jet show that the sheets tend to align predominantly along the radial direction.

Buch and Dahm provided an analysis which suggests that the internal structure perpendicular to the sheets should have scalar distributions consistent with the error-function distribution expected for diffusion between locations having different concentrations.[38,47] This distribution leads to an expected Gaussian distribution for the scalar dissipation distribution across the layer. Experimental observations in both high Sc and Sc ≈ 1 flows were consistent with this analysis. Southerland and Dahm's later work supports this conclusion.[59]

A combination of experimental, analytical, and modeling investigations is beginning to provide some insights into the physical processes responsible for the organization of the velocity and scalar small-scale structure. It is important to consider the velocity field because the local strain-rate field is ultimately expected to determine the scalar structure. Early analyses had suggested that the local strain-rate field in a turbulent flow field could concentrate vorticity into narrow tube-like or plane-like structures depending on whether the principal strain axes consisted of one compressible and two extensional components or two compressible and one extensional component, respectively.[95,96,97] Generally, the thicknesses of the tubes or sheets are on the order of the Kolmogorov scale, while the dimensions in the elongated directions can be much greater. While limited experimental evidence (e.g., Kuo and Corrsin[98] and Noullez et al.[77]) is available concerning the development of such structures, considerably more detailed insight has been derived from direct numerical simulation (DNS) of turbulent flows. The works of Kerr[99] and Rogers and Moin[100] with follow-on analysis by Ashurst et al.[101] provide particularly relevant insights into the expected nature of small-scale structure for both velocity and scalar fields.

Kerr's DNS calculations indicated that the highest values of vorticity within a turbulent flow field are organized into tube-like structures which extend over a significant fraction of the integral scale for the flow. As would be expected, the vortex tubes are associated with regions of large strain rate covering relatively large areas. On average, the largest magnitude principal strain rate in the vicinity of the vortex tubes is found to be negative (i.e., compressive) and to be aligned perpendicular to the tubes. Interestingly, the most positive (extensive) principal strain rate is also most likely to be aligned perpendicular to the tubes. Recall that the sum of the principal components of the strain rate must be zero, implying that the vorticity is most likely to be aligned along the positive principal strain-rate axis having the smallest absolute value.

The vortex tubes were found to wrap a scalar into thin sheets around the outer edges of the tube with the scalar gradient aligned perpendicular to the vorticity. Kerr's results indicated that both the vorticity and scalar fields displayed strong small-scale intermittency behavior and that the

intermittency was more intense in the scalar field. A possible connection was drawn between the scalar small-scale intermittency and the presence of internal ramp-like structures.

Ashurst et al.[101] performed more extensive statistical analysis of DNS results based on calculations reported by both Kerr[99] and Rogers and Moin[100]. Their findings substantiated those of Kerr. Intense vortical structures are generated which are stretched primarily in one dimension. Their analysis showed that the local strain fields around the vortex tubes are quasi-two dimensional since magnitudes of the compressive and extensive principal strain rates perpendicular to the vortex tube direction are of comparable magnitude. The vortex direction generally was found to lie along the intermediate principal strain rate axes which was generally positive (extensive). The authors provided an analysis based on an Euler model of vorticity-shear interaction which supports these conclusions. They also showed that the strong scalar gradients which develop near the vortex tubes are most likely to align along the direction of the largest compressive principal strain rate. While not emphasized by the authors, it is worthwhile to mention that the correlations of the vorticity directions with the principal strain-rate axes were not nearly as high for locations where the vorticity was not strongly concentrated.

A major difference between the work of Kerr[99] and Rogers and Moin[100] is that the former utilized isotropic forcing for his calculations, while the latter authors imposed a mean shear along one axis. Significantly, Rogers and Moin discovered that the vorticity field was not isotropic, but that the vorticity tended to align along favored angles in the plane formed by the average flow and shear directions. The degree of alignment varied with vorticity magnitude, with higher vorticity fluid more likely to be aligned in the favored direction. The most likely angles within the plane varied with time. When the structures first formed, they were most likely to occur at angles of 45° and 135° from the flow direction, while at later times the most likely angle decreased by 5°-10° due to rotation of the vorticity by the mean flow. Rogers and Moin noted that "This result illustrates the importance of vortex stretching by *mean* shear to the dynamics of shear flows and indicates that planes inclined near 45° to the mean flow direction are likely to contain strong vortical structures."

Several recent investigations have used DNS to simulate turbulent flow in the presence of a scalar gradient. Holzer and Siggia performed calculations in two dimensions using a pseudo-turbulent velocity distribution.[89] They found that the two-dimensional scalar dissipation was isotropic since both averaged components were roughly equal, but that the instantaneous gradient pdfs differed for directions perpendicular and parallel to the imposed mean scalar gradient. The perpendicular component pdf was symmetric, while the parallel component was strongly skewed towards positive values. Instantaneous snapshots of the scalar field showed that distinct ramp-like structures,

reminiscent of the experimental internal ramp-like structures described above, developed in the direction of the scalar gradient. The sharp edges of the ramps (cliffs) separated much larger spatial regions where the scalar concentration was relatively constant. Detailed comparisons indicated that the cliffs occurred in the region of large-scale flow convergence to a stagnation point for which the compressive principal strain-rate axis had a substantial projection onto the direction of the mean gradient. The cliffs themselves were aligned roughly along the separatrices along the outflow principal directions. The cliff structures were found to exist for periods on the order of the integral time scale. The process was characterized as a continuous formation and decay of the sharp concentration gradients. There is a similarity of the calculated behaviors to experiments showing nonzero skewness values for the scalar gradients. The authors also reported that the tails of the pdfs for the dissipation were not log normal, but could be fit as stretched exponentials.

Pumir reported a similar investigation to that of Holzer and Siggia, but made the calculations in three dimensions.[90] In general, he confirmed the major findings of the two-dimensional investigation despite the more complicated nature of the three-dimensional flow field. Based on the calculations he speculated that "the mechanism of gradient expulsion is highly anisotropic, and that efficient homogenization occurs primarily in planes perpendicular to the mean vorticity vector." Pumir also noted strong similarities between the dynamics of vorticity and scalar gradients, particularly the ability of the flow to concentrate strong gradients for each. Overholt and Pope also have reported extensive DNS calculations of passive scalar behavior in the presence of a mean gradient for a three-dimensional system.[93] Their findings are consistent with those discussed above.

Buch and Dahm have discussed the role of the local strain-rate field in the formation of strong concentration gradients in turbulent flows.[38,47] They point out that depending on the magnitudes and signs of the principal axes, either tube-like or sheet-like scalar structures can be formed. However, their analysis indicates that any tube-like structures formed are dissipated very rapidly, while sheet-like structures can form and exist over long periods of time. This provides an explanation for the observation of primarily sheet-like scalar structures.

The discussion above suggests that there are at least two mechanisms for concentrating scalars into sheets within a turbulent flow field. The first is expected in hyperbolic regions of the flow field between two large-scale vortical structures. This type of behavior should be present relatively infrequently, but is capable of generating very strong gradients. It has been associated with the presence of internal ramp-like structures. The second is the concentration of a scalar into sheets in the vicinity of strong tube-like vortical structures with the scalar gradient aligned predominantly along the most compressive principal strain direction. The latter process would be expected to occur within the

extensive volumes located between the sharp cliffs of internal ramp-like structures, i.e., in regions generally characterized as having relative constant scalar values. This suggests that the scalar gradients associated with tube-like vortical structures will be somewhat smaller that those associated with the large-scale hyperbolic regions. The results of a DNS simulation by Ruetsch and Maxey seem to support this view.[102]

D. Current Investigation

Although there have previously been extensive experimentation and analysis, to date, a comprehensive model for the formation and evolution of large-scale turbulent structures and their role in turbulent shear-flow mixing has not emerged. The behavior of the scalar dissipation and its relation to large-scale structure is also incompletely characterized. This paper describes experiments which contribute to an improved understanding of LSTSs and scalar dissipation for an isothermal axisymmetric jet. A digital line camera capable of real-time (rates > 2 kHz) imaging of Rayleigh light scattering is used to study the instantaneous scalar field of a turbulent propane jet. Similar limited measurements using an earlier version of this camera have been described.[24,25,26]

II. EXPERIMENTAL APPROACH

A. Rayleigh Light Scattering for Concentration Measurement

Rayleigh light scattering (RLS) refers to the scattering of light by molecules at the same wavelength as the incident light. For an isothermal, constant pressure gas consisting of two molecular species, the intensity of light (I_s) scattered from an observation volume can be written as

$$I_s = NI_o(\sigma_1 X_1 + \sigma_2 X_2) \tag{13}$$

where N is the total number of molecules in the volume, I_o is the intensity of light incident on the volume, σ_1 and σ_2 are the Rayleigh light scattering cross sections for gases 1 and 2, and X_1 and X_2 are the mole fractions of gases 1 and 2 in the observation volume.

In practice, relative values of RLS intensities are often determined by recording the scattering signals from two calibration gases, typically gases 1 and 2. Once the calibration intensities are available, the concentration of an arbitrary mixture of the two gases can be obtained simply as

$$X_2(t) = \frac{I(t)-I_1}{I_2-I_1}, \tag{14}$$

where $X_2(t)$ is the time-dependent mole fraction of species 2 in the observation volume, $I(t)$ is the time-varying scattering intensity from the observation volume containing the mixture, and I_1 and I_2 are the average scattering signals from the observation volume for gases 1 and 2.

As first demonstrated by Graham et al.[103] and Dyer[104], when laser beams are used to induce RLS, it is possible to monitor concentration in binary mixtures in a volume with high temporal and spatial resolution. Pitts and Kashiwagi have provided a detailed analysis of the use of RLS for monitoring concentration in turbulent flows of two gases.[3] The maximum temporal and spatial resolution possible depends on the gas pair, but typical values using a high power continuous argon ion laser are 50 μs for an observation volume on the order of 10^{-3} mm^3 with an accuracy of 1 % or better for each individual measurement. A detailed discussion of the various noise sources which limit RLS accuracy can be found in Pitts and Kashiwagi.[3]

B. Line Camera System

1. Background

RLS has been used to record real-time concentration measurements at a single point in numerous studies of turbulent mixing (e.g., see Pitts and Kashiwagi[3], Green[105], Pitts[106,107], Dowling and Dimotakis[67], Dowling[49], Richards and Pitts[4]). RLS also offers the possibility of making multipoint measurements. Many researchers have reported such measurements using intense pulsed lasers as light sources. In some cases (e.g., Dibble et al.[44]) the RLS from a length of a laser beam has been imaged onto a line detector, and the instantaneous concentration fluctuations along the laser beam have been recorded. Others have expanded the laser beam into a thin sheet and used RLS to measure instantaneous concentration in two dimensions.[41,47,48,72,108,109] The authors are unaware of any work which extends RLS line or planar imaging to real-time measurements. In principle this would be possible using multiple detectors and lasers (or multi-pulse lasers) for experiments similar to those of Yip and Long[62,63], Mansour[64], and Su and Clemens[72] who have recorded RLS from two closely spaced sheets. It should be noted that other optical techniques have been used to acquire short time records of planar images for concentration measurements in gas flows (e.g., Winter et al.[110]) and real-time three-dimensional measurements (Dahm et al.[37,59]) have been recorded in liquid flows.

2. Previous Development of an Intensified Line Camera for RLS Measurements

The primary reason that only limited measurements have been reported using RLS for real-time multipoint concentration measurements is that RLS is relatively weak, and intense lasers and sensitive

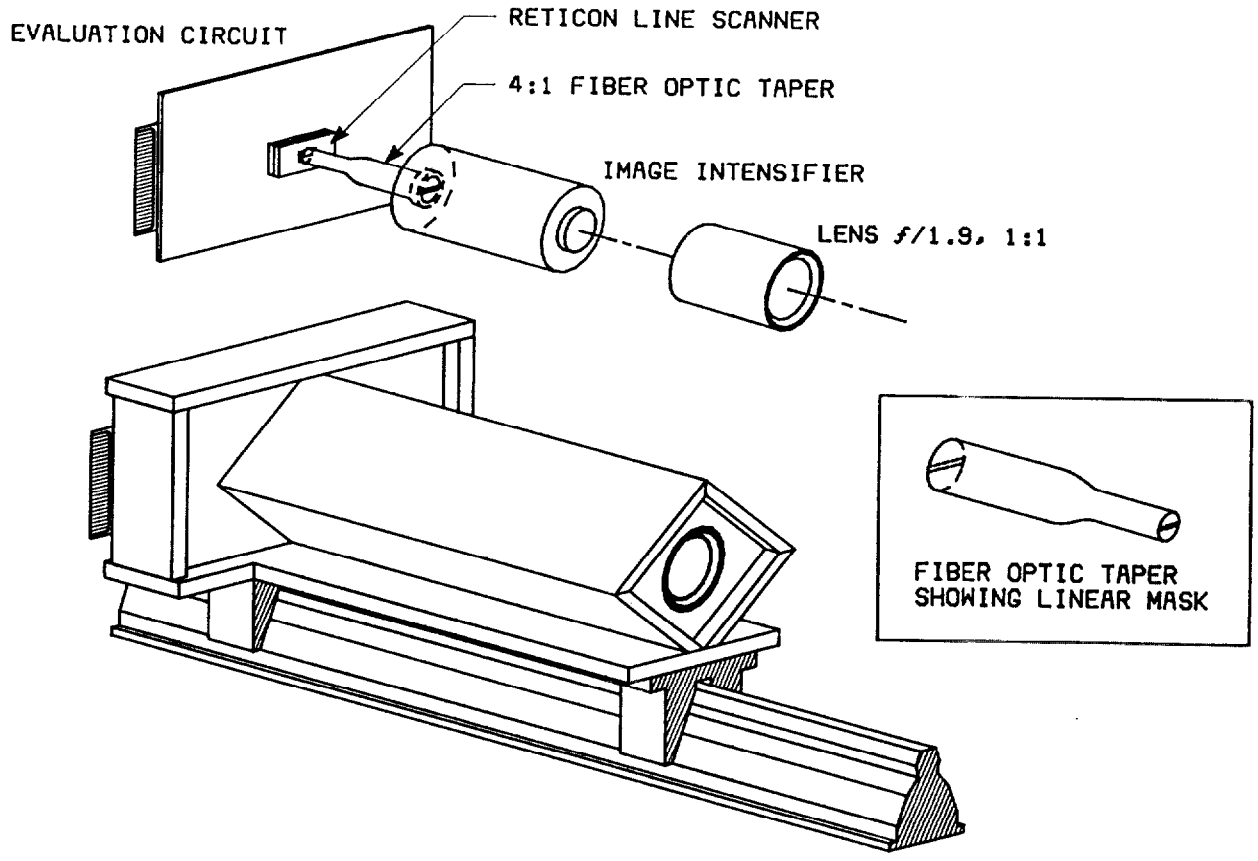

Figure 1. Schematic showing the major components and appearance of the real-time line camera.

light detection are required for time-resolved measurements. Suitable combinations of high pulse-rate lasers and sensitive optical multipoint detectors having high readout rates have not been available. Pitts has discussed many of the technical problems in a published meeting proceedings.[111] The details will not be repeated here, interested readers should consult the original work.

In this earlier paper the development of a line camera capable of recording light intensity for 128 pixels at line readout rates as high as 2.38 kHz was described.[111] This camera system recorded concentration fluctuations for favorable RLS gas pairs (e.g., propane and air) with a reported individual pixel uncertainty of 5 %. Figure 1 is a schematic for the line camera itself and Fig. 2 shows a schematic for the entire camera system including the line camera, interfaces, and data acquisition system.

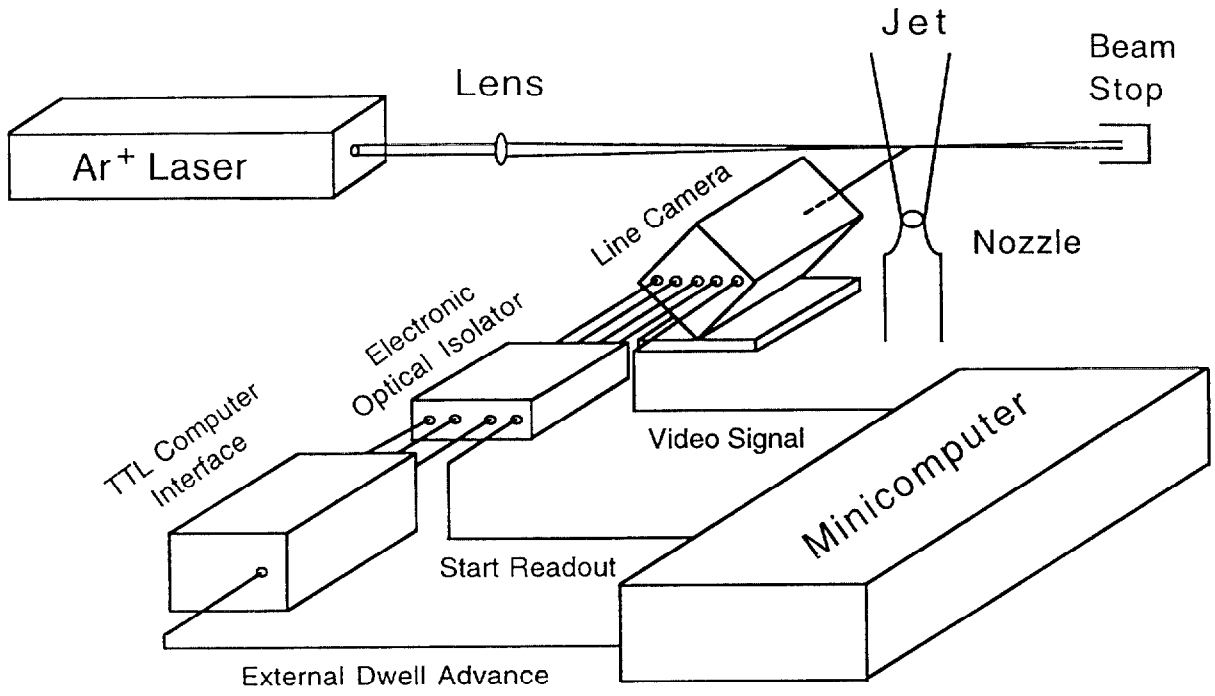

Figure 2. A schematic showing the overall arrangement of the line camera system and associated electronics for recording real-time RLS measurements of concentration.

Figure 1 shows that the real-time line camera included an image intensifier which was required because the line scanner (Reticon** RL128SF line scanner equipped with RC1024S-1 evaluation circuitry) used did not have sufficient signal-to-noise ratio to accurately measure the RLS intensity when imaged directly onto the detector. Image intensifiers have been widely employed for scientific imaging using pulsed laser sources. Most of these experiments have used second-generation image intensifiers equipped with P-20 phosphor screens. As discussed by Pitts, such intensifiers are not suitable for this high speed, real-time application due to current-saturation effects within the microchannel plates used as spatial electron amplifiers in these devices and the relatively long phosphorescent lifetime of the P-20 phosphor.[111] As a result, a two-stage first-generation image intensifier equipped with a P-47 phosphor screen (τ_p = 80 ns and λ_{max} = 400 μm, where τ_p is the

*Certain commercial equipment, instruments, or material are identified in this paper in order to adequately specify the experimental procedure. Such identification does not imply recommendation or endorsement by the National Institute of Standards and Technology, nor does it imply that the materials or equipment are necessarily the best available for the purpose.

phosphor decay time and λ_{max} is the wavelength of maximum spectral output) was used. A first-generation image intensifier employs electrostatic focusing of accelerated electrons released by a photocathode onto a phosphor screen to generate the amplified light output. As a result, it is not subject to the current limitations of a microchannel plate, and higher current densities can be generated while maintaining the spatial resolution. Light was coupled into (photocathode) and out of (phosphor screen) the image intensifier by fiber optic faceplates.

The output of the image intensifier was connected by a 4:1 reduction fiber-optic taper onto the fiber-optic faceplate of the line scanner. The line scanner control circuitry allowed the line read-out rate of the camera to be varied up to a maximum of 2.38 kHz. The output of the line camera was a time-varying analog signal having voltages proportional to the varying light levels across the input face of the image intensifier.

The camera's analog output was interfaced to a minicomputer through circuitry, designed and built in-house, which allowed the voltage output to be digitized and stored for later analysis. Due to the relatively weak signals and the voltage range of the digitizer, roughly one hundred digital levels (signals varied with pixel number) corresponded to the full range of concentration. The memory of the minicomputer used in the initial investigation was limited to 32,768 words, which meant that an individual data record consisted of 256 scans of the 128 pixel array.

Images of concentration along the radial profile of an axisymmetric jet of propane flowing into a slow coflow of air demonstrated the feasibility of real-time line measurements of concentration in turbulent flows. These initial images were sufficient to demonstrate the presence of large-scale structures in the flow. Similar images were reproduced in papers which focused on the mechanisms for the stabilization of lifted turbulent jet diffusion flames.[25,26] A unique aspect of this work was that the concentration data were recast in terms of the combustion behavior of the propane/air mixtures to provide a spatial and temporal map of flammable regions in the jet.[25]

Muck et al. combined the RLS line camera system with a linear array of seven hot wires to form an experimental system capable of simultaneous, real-time line measurements of concentration and velocity.[112] Time-averaged and rms values of radial concentration and velocity profiles for the propane axisymmetric jet flowing into a slow coflow of air were consistent with those expected for this type of flow.

3. Line Camera System Used in the Current Investigation

Subsequent to the earlier work discussed above, the line camera has been modified to increase its sensitivity by replacing the two-stage first-generation image intensifier with a three-stage device

equipped with a P-46 phosphor screen (τ_p = 160 ns and λ_{max} = 530 μm). Improved high-voltage power supplies for the image intensifier were also installed. The use of three stages of image intensification increased the amplification of the detected RLS, and the shift in the maximum spectral output from 400 μm to 530 μm improved the overlap of the phosphor spectral distribution with the spectral response curve for the line scanner as well as the transmission of light through the fiber optics. As a result, the signal-to-noise ratio was improved by a factor of 13 compared to the earlier version of the line camera. Concentration measurements having an accuracy of $\approx$ 1.5 % of the full range were reported for propane/air flows. As discussed below, this camera system has been found to be capable of much higher accuracy.

A further improvement has been made to the line camera system by interfacing the analog output to a Concurrent 5450 workstation. As a result, quite long data records are now possible while recording data at the maximum line read-out rate of 2.38 kHz. For the measurements reported here, the data records consisted of 3000 sequential line scans corresponding to 384,000 individual concentration measurements. For the line read-out rate of 2.38 kHz, the total data acquisition time is 1.261 s.

With the current line camera system, the signals recorded for pure propane correspond to voltages providing roughly 330 to 500 digital counts, depending on the pixel number. Figure 3 shows the recorded digital signals for RLS from propane and air as a function of pixel number. These calibrations indicate that the difference of a single digital level represents a 0.002 to 0.003 step in propane mole fraction. At the time of the experiments, this was judged to be sufficient since the measured noise in an individual concentration measurement was estimated to be 1.5 %, as noted above.

During the analysis of the data to be presented below, it was noted that much of the noise in the camera signal was the result of two repetitive and reproducible electronic waveforms of alternating sign which appeared as short-lived (approximately 180 μs, covering roughly 60 pixels of a single line scan) voltage ramps at a frequency of 120 Hz. The voltage maximum of the ramps gave a false signal corresponding to a propane mole fraction change of $\pm$0.02. The source of the noise is unknown, but it was found that it was sufficiently reproducible to be nearly completely removable from the data by subtraction of a digital ramp having the same sign as the noise signal. Careful adjustment of the phase and frequency of the correction signal allowed an entire data set to be treated. Following this correction, analysis of RLS signals from air indicated that the uncertainty ($\pm 1\sigma$) in individual measurements was now equivalent to $\pm$1 digital levels, i.e. a mole fraction of 0.002 to 0.003. In other words, the precision of an individual measurement in the corrected data was now limited by the voltage range supplied to the digitizer and not by inherent noise in the measurement. A wavelet-based analysis

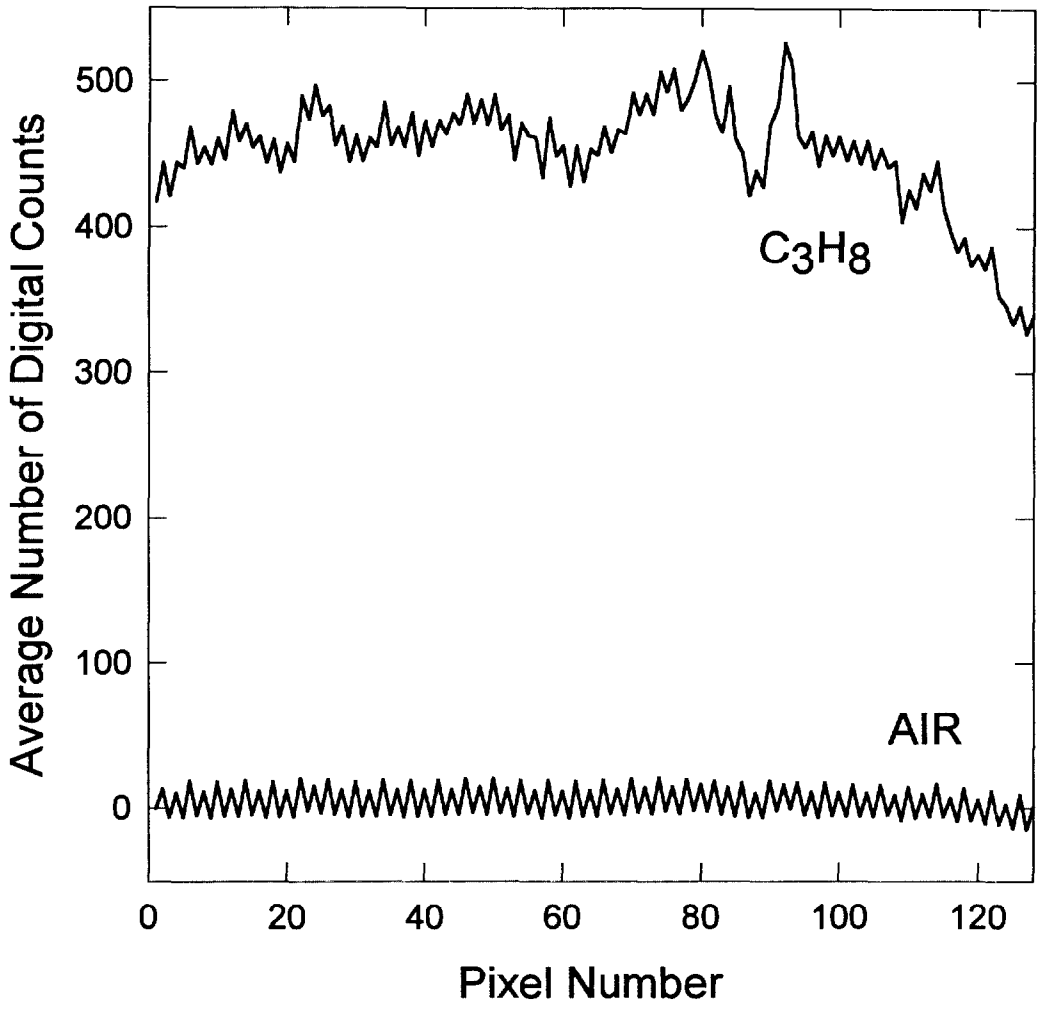

Figure 3. Time-averaged outputs of the line camera for scattering from air and propane are shown. The data are presented in terms of the average number of digital counts recorded by the data acquisition system.

developed to extend the effective digital resolution of the line camera measurements is discussed below.

C. Flow Facility and Optical Arrangement

The current experiments were performed in the quiescent environment of a cylindrical clean room, in contrast to earlier measurements using the line camera[24,25,26,111,112] which were for an axisymmetric propane jet entering a slow coflow of air. The new facility, known as the Rayleigh Light Scattering Facility (RLSF), has been carefully designed to minimize interferences associated with glare

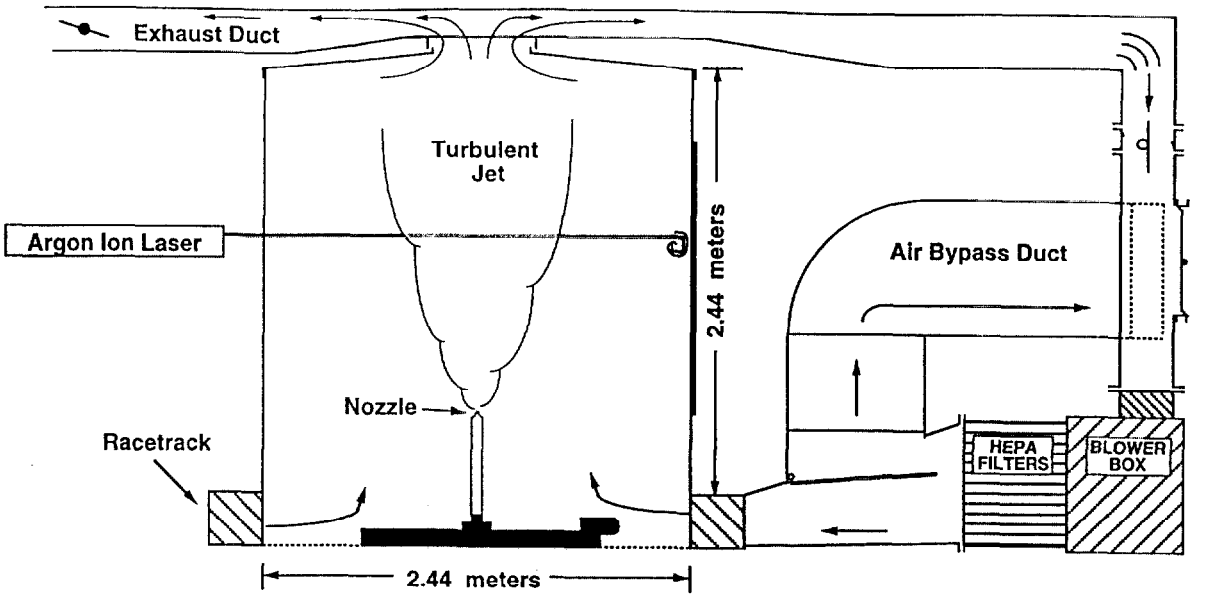

Figure 4. Schematic for the Rayleigh light scattering facility which is described in detail by Bryner et al.[113]

and Mie scattering. It is described in detail by Bryner et al.[113] A schematic of the RLSF is shown in Fig. 4.

The jet was produced by a flow of propane metered by a mass-flow controller which exited through a contoured nozzle with an inside diameter of 6.35 mm and an area contraction ratio of 100:1. The same nozzle was employed for an earlier investigation of similarity behavior in axisymmetric jets.[4] The Reynolds number of the jet flow based on jet exit conditions,

$$Re = \frac{U_o d_o}{\nu_o} , \tag{15}$$

where ν_o is the kinematic viscosity for propane[114] and U_o = 2.78 m/s, is 4079. The flow assembly was mounted on a three-axis, computer-controlled traverse placed on the floor of the test section which allowed the nozzle to be positioned relative to the RLS observation volume. The nozzle was mounted such that the jet gas issued vertically upward (defined as the z axis) into the enclosure as shown in Fig. 4. Propane was supplied from pressurized tanks and was filtered to remove oil, moisture, and particulate.

The experimental configuration is similar to that described by Pitts and Kashiwagi[3], except that the lens and photomultiplier system for measuring the Rayleigh light scattering signal are replaced with the line camera system. A schematic of the RLS optical arrangement is shown in Fig. 5. It consists of

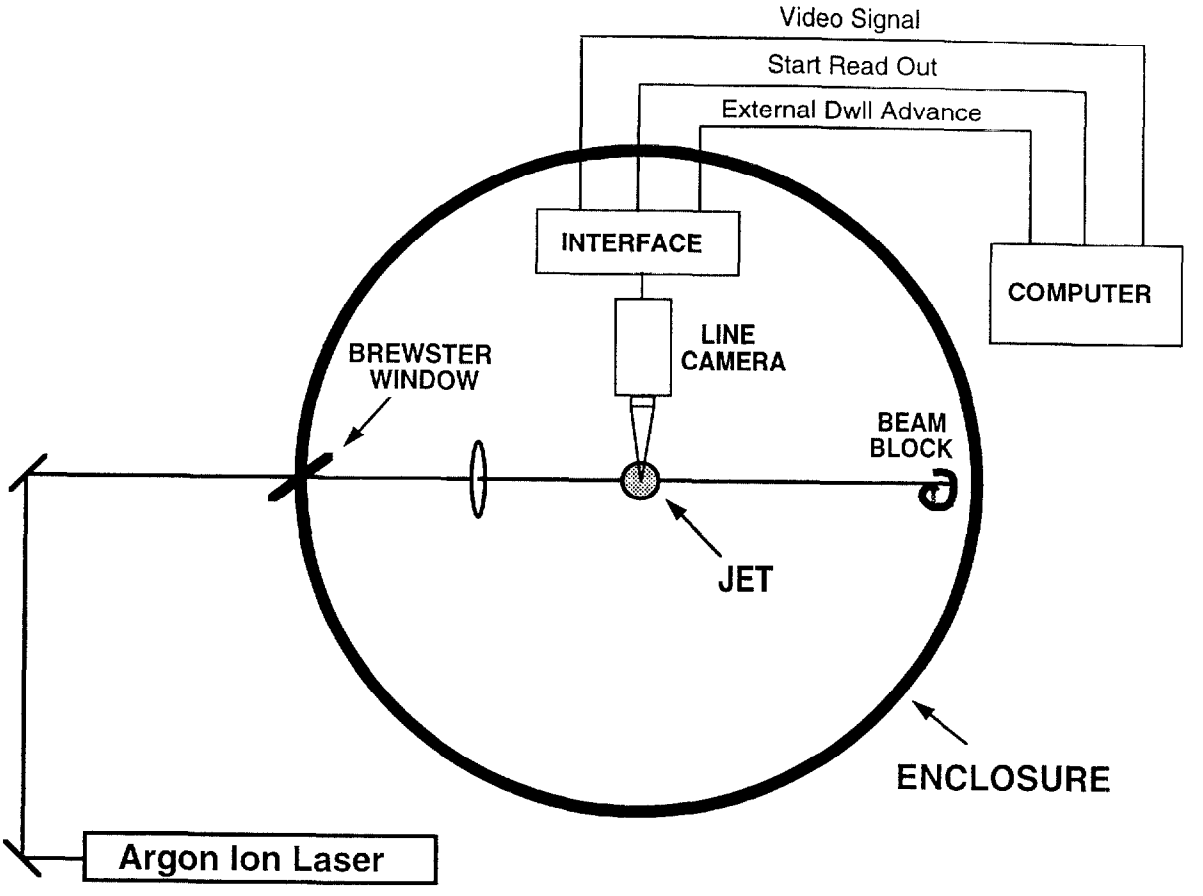

Figure 5. The optical arrangement for real-time RLS measurements of concentration along a line in a turbulent flow field is shown.

a focused laser beam to induce RLS and the line camera system shown in Fig. 2, consisting of the line camera, interface circuitry, and the Concurrent Model 5450 computer which digitizes and stores the voltage output of the line camera. An argon ion laser operating on all lines at a nominal power of 20 W was used to induce RLS. The laser beam was focused to a narrow waist having a diameter of 50 μm by a 25 cm focal length lens, and the diameter was less than 100 μm over the length observed by the line camera. The laser beam was oriented perpendicular to the primary jet flow direction and passed through the jet centerline. The line camera was positioned 90° to the laser beam in the same horizontal plane.

The length of the laser beam imaged onto the line camera is determined by the magnification of the collection lens, a slight demagnification of the image by the image intensifier, the 4:1 image reduction by the fiber optic taper, and the pixel size. The linear array consists of 128 pixels having an

aspect ratio of 100:1 with 25 μm centers. The magnification of the lens system is roughly 1:1. By scanning a narrow wire along the axis of the camera and recording the position, the spacing between pixel centers was measured to be 113 μm. Thus the overall imaged length was 14.5 mm. Due to cross talk between adjacent pixels in the line scanner, the best possible resolution is limited to approximately 180 μm.

The actual spatial resolution of the system was determined using Mie scattering signals from particles which were observed very infrequently during RLS measurements. Since the particles can be assumed to be much smaller than the observation volume for a single pixel, their measured widths should correspond to the effective spatial resolution of the line camera system. Figure 6 shows the radial profile of propane mole fraction recorded during one of these occurrences as a function of pixel number. The line scans recorded immediately before and afterwards are also shown. The sharpness of the peak in the second scan and the fact that it is only present during one scan clearly identifies the signal as being due to a small particle. The adjacent scans allow a baseline for the particle signal to be estimated. The inset in the figure shows the particle signal with baseline subtracted as a function of relative position. The particle signal consists of a sharp center peak and rather long weak tails on either side. The solid line is the result of a least squares fit of the data to a Lorentzian curve,

$$S(r) = \frac{h\left(\frac{w}{2}\right)}{\left(\frac{w}{2}\right)^2 + (r-m)^2} \quad , \tag{16}$$

where S is the scattering signal, r is the radial position, h is a normalizing factor, w is the full width at half maximum (FWHM) for the fit, and m is the value of r for the maximum S. The fit shown in the inset yields a FWHM of 363 μm which is taken to be the effective resolution, R_r, of the system in the radial direction. The weak tails observed in the signal, which extend over relatively large distances, are due to cross talk between fibers within the fiber-optic taper used to connect the output of the image intensifier to the line scanner.

The effective resolution in the axial direction depends on the instantaneous flow velocity at the measurement location. A characteristic value, R_z, can be defined in terms of the product of the average centerline velocity, $\bar{U}_m$, and integration time, τ_m = 420 μs, for the measurement. The centerline flow velocity at z/r_o = 40 was estimated as $\bar{U}_m$ = 1.09 m/s using

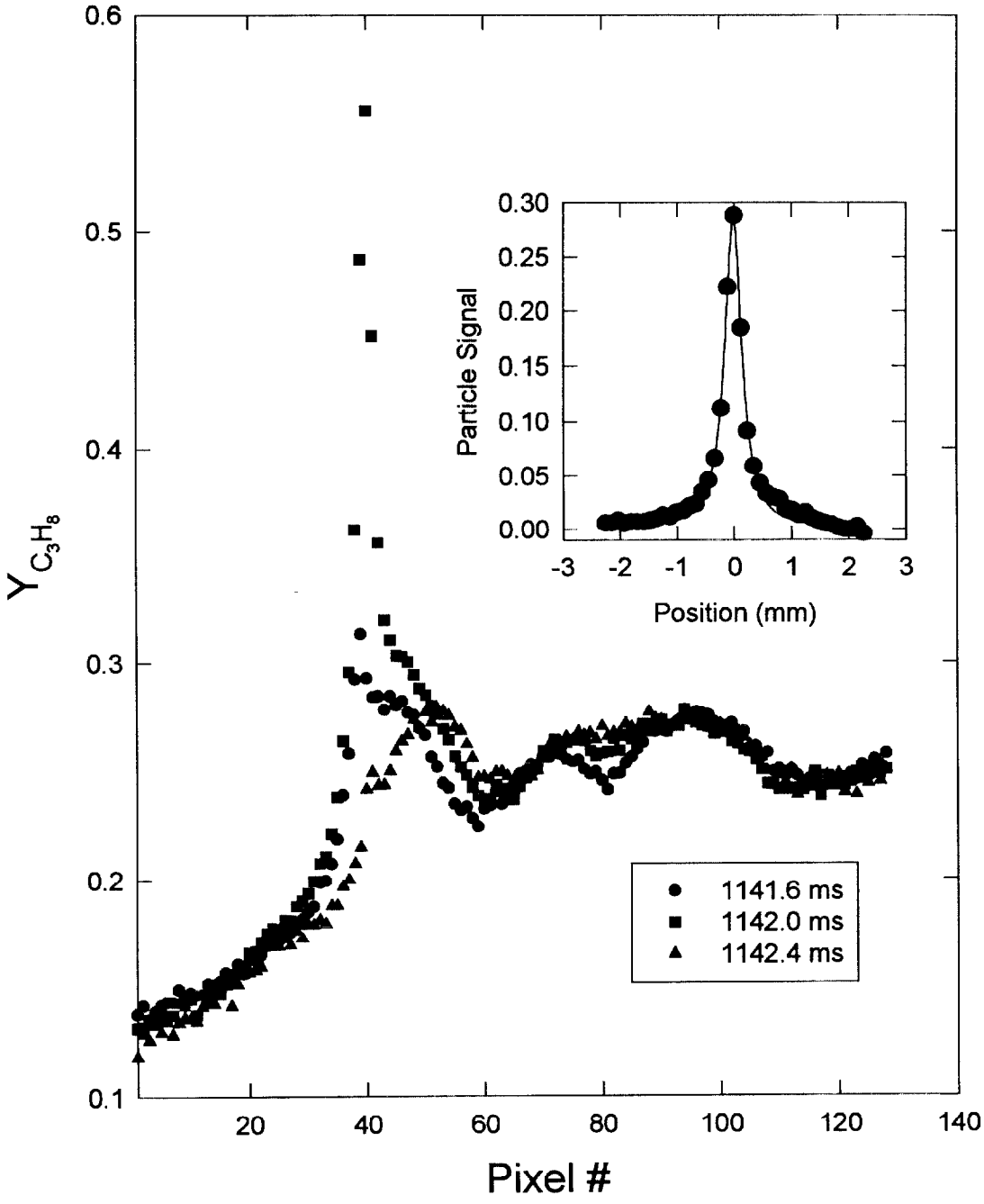

Figure 6. Three radial profiles of relative RLS intensity spaced 420 μs apart are shown in mass fraction terms. The passage of a particle during the second scan is easily identified. The insert shows the signal due to the particle obtained by subtracting the baseline from the signal recorded at 1142.0 ms. The solid line is the result for a Lorentzian least-squares curve fit to the particle signal.

$$\frac{U_o}{\overline{U}_m} = k_u \frac{(z-z_o)}{r_\epsilon} \quad , \tag{17}$$

which assumes the velocity field has a self-similar behavior. r_e is the effective radius defined as

$$r_\epsilon = r_o \sqrt{\frac{\rho_o}{\rho_\infty}} \tag{18}$$

and z_o is a virtual origin which is assumed to be at the jet origin, i.e. $z_o = 0$. A value of $k_u = 0.0794$ based on the review of Chen and Rodi was used.[5] The more recent measurements of Panchapakesan and Lumley agree well with this estimate.[115] A value of $R_z = 458$ μm is the result.

D. Experimental Procedure

Measurements were made in an isothermal propane jet at a downstream distance of $z/r_o = 40$. The jet was traversed across the image plane of the camera to acquire a series of five 14.5 mm image segments which spanned the full diameter of the jet.

The Batchelor scale was chosen as the appropriate scale for characterizing the required spatial resolution. The Batchelor scale for the experimental conditions of this study was estimated using Eqs. (8) and (10) which can be written as

$$\eta_B = (r_{1/2})_u Re_t^{-3/4} Sc^{-1/2} = (r_{1/2})_u \left(\frac{U'_m (r_{1/2})_u}{\nu} \right)^{-3/4} Sc^{-1/2}, \tag{19}$$

where U'_m is taken to be 0.24 times $\overline{U}_m$ based on the recent measurements of Panchapakesan and Lumley.[115] A value of $(r_{½})_c$ was calculated using the mass fraction spreading rate reported by Richards and Pitts[4] and assuming a virtual origin at the jet origin. The corresponding result for the velocity field, $(r_{½})_u = 12.3$ mm, is obtained using the ratio $(r_{½})_c/(r_{½})_u = 1.17$ recommended by Chen and Rodi.[5] The value of Sc was determined from the ratio of the kinematic viscosity for the average concentration on the jet centerline, ν_m, with the mixture dynamic viscosity calculated using the approximation of Wilke,[116] and the binary diffusion coefficient for propane into air, D[117]. The results of these calculations are summarized in Table 2 along with other parameters for the flow and experimental system. The estimated value of η_B is 177 μm. Use of Eqs. (7) and (8) along with Eq. (12) suitably modified for variable density flows yields an estimate of $\eta_B = 164$ μm which is in good agreement. Ratios of the estimated spatial resolution in the radial and axial direction and the Batchelor scale are $R_r/\eta_B = 2.1$ and $R_z/\eta_B = 2.6$. Based on the earlier discussion, it is concluded that the

Table 2. Experimental and flow parameters.

ρ_∞	1.197 kg/m^3	
ρ_o	1.823 kg/m^3	
ν_o	4.33×10^{-6} m^2/s	Reference 114
ν_∞	1.53×10^{-5} m^2/s	Reference 114
U_o	2.78 m/s	
Re	3960	Eq. (15)
D	1.124×10^{-5} m^2/s	Reference 117
$\bar{U}_m$	1.08 m/s	Eq. (17)
U_m'	0.259 m/s	Reference 115
$\bar{Y}_m$	0.294	Reference 4
Y_m'	0.068	Reference 4
$(r_{1/2})_u$	$3.86\, r_o = 0.0123$ m	Reference 5
$(r_{1/2})_c$	$4.52\, r_o = 0.0144$ m	Reference 4
L_{jd}	0.056 m	Eq. (31)
τ_{jd}	0.052 s	Eq. (30)
ν_m	10.92×10^{-6} m^2/s	Reference 116
Sc	0.97	
Re_t	292	
η_K	174 μm	Eq. (10)
η_B	177 μm	Eq. (19)
$\bar{\varepsilon}$	1.91 m^2/s^3	Eq. (12)
η_K	162 μm	Eq. (7)
η_B	164 μm	Eq. (8)
R_r	363 μm	
R_z	458 μm	
R_r/η_B	2.1	
R_z/η_B	2.6	

resolution available in the radial direction will be sufficient to resolve all but the very smallest scales over which changes in the concentration gradient occur, while only minor averaging is to be expected in the axial direction.

The line concentration measurements were performed in a manner similar to the single-point measurements of Pitts and Kashiwagi.[3] The RLS intensity was first calibrated by recording the average signals, $I_a(i)$ and $I_p(i)$, from the unmixed gases, air and propane, for each pixel i (i.e., i = 1 to 128). The turbulent flow was then initiated and the real-time RLS signal, $I(i,t)$, recorded. The resulting data were stored on hard disk for later analysis.

E. Data Analysis

The first step in the analysis procedure was to determine the mole fraction for propane, $X_p(i,t)$ for each pixel as a function of time. Eq. (14) was used for this purpose along with the measured radial profiles of $I_a(i)$ and $I_p(i)$. Following this calculation, the temporal positions of the ramp-like noise voltages were identified and specially written code was used to digitally subtract a voltage signal of the appropriate sign. As noted above, following this correction, the noise level in the measurements corresponded to a difference of one digital count. In other words, the measurement precision was now determined by the limited dynamic range of the digitization process.

Even though the dynamic range and precision of the measurements were quite good (roughly 1 part in 400 to 500 of full scale), it was quickly discovered that the limited number of digital levels available prevented an accurate determination of scalar dissipation pdfs. The reason for this was that the required derivatives were determined simply by subtracting concentrations at two adjacent pixels or times, and only a very limited number of concentration values were possible. The resulting probability density functions were quite spiky and nonphysical. It was clear that it was necessary to apply a procedure which would provide a significantly wider range of possible values, but would maintain the precision of the measurements. Wavelet analysis was found to be ideal for this purpose.

Wavelet transforms have proven to be a valuable tool in many applications. For a short introduction to the method see Strang[118], and for a deeper treatment see Daubechies[119]. The particular approach adopted here has been described in a meeting proceedings.[120] The wavelet transform is similar to the better-known Fourier transform. Each represents the signal as a weighted sum of orthogonal basis elements. For the Fourier transform the basis elements are sine and cosine functions, while for wavelet analysis they are the scaling and translations of a function known as the mother wavelet function.

For a one-dimensional function, f, defined at n discrete points t_i on the unit interval (i.e., $t_1 = 0$ and $t_n = 1$) the wavelet basis representation is

$$f(t_i) = \sum_j \sum_k c_{jk} w(2^j t_i - 2^{-j}k) \quad , \tag{20}$$

where $w(t)$ is the mother wavelet. The index j scales the mother wavelet by 2^{-j}, and the index k translates the mother wavelet by $2^{-j}k$. If n is a power of two, then the ranges of the indices in Eq. (20) are $j = 0$ to $\log_2(n)$ and $k = 0$ to j.

Wavelets can express nonstationary signals with only a few basis elements, while noise is spread out over many coefficients because the transform is orthogonal. Donoho and Johnstone exploited this property to create nonparametric denoising procedures.[121] Their approach was to first estimate the noise level, σ, and then subtract its magnitude from the wavelet coefficients. The procedure followed in the current study was:

1. Compute the discrete wavelet transform,
2. Extract the fine-scale coefficients,
3. Replace each c_{jk} with

$$\begin{array}{ll} 0 & \text{if } |c_{jk}| \le \sigma \\ \text{sign}(c_{jk})(|c_{jk}| - \sigma) & \text{if } |c_{jk}| > \sigma, \end{array}$$

and

4. Compute the inverse discrete wavelet transform.

For the current problem, both the dominant noise source and its magnitude are known. The dominant source is the truncation of continuous mole fraction values to discrete values which are approximately 0.0025 mole fraction units apart. A value of $\sigma = 0.0050$ is used because it is desired to remove the local fluctuations resulting from the digitization noise.

A two-dimensional analog of Eq. (20) was used for the actual implementation of wavelet analysis to the mole fraction measurements. The symmlet-16 basis from Bruce and Gao was employed.[122] Each image was extended by reflecting 5 pixels around the borders and using a constant interpolation rule in order to overcome boundary artifacts. Following the application of the procedure, the transformed and original data were compared. Average residual values were on the order of σ and their magnitudes were randomly distributed. As will be demonstrated shortly, the wavelet analysis proved highly effective in reducing the digitization noise in the pdfs of scalar dissipation.

As already discussed, the uncertainty of a single measurement in the raw data was roughly one part in five hundred (it varies somewhat with radial position) and is very close to that expected for the digitization noise. Following application of the wavelet analysis, a similar noise analysis for the

processed data based on the observed variations in concentration for regions of the flow where only air is present yielded a root mean square of 0.0008, or roughly a factor of three reduction in the uncertainty.

As we shall see shortly, the images of scalar dissipation calculated using the processed data, as well as pdfs based on the results, suggest considerably smaller uncertainties. The nature of wavelet analysis and the correlations of the concentrations provide an explanation for this apparent contradiction. First, structures, both local and global, are well captured by the wavelet processing. This will become evident when images of the scalar dissipation are shown in the Experimental section. As a result, the contours of structures are reproduced smoothly, greatly reducing apparent noise. Second, the underlying concentration values are highly correlated, and the measurement uncertainties of the processed measurements are highly correlated. These correlations create cancellations of error when global quantities such as pdfs are calculated from the processed data. The correlations, both in the concentration and the wavelet analysis errors make it difficult to quantitatively assess the uncertainty, but the ability to generate meaningful pdfs for scalar dissipation, as shown shortly, indicates the effective noise has been substantially reduced compared to estimates based on single measurements in flow regions where the results are expected to be uncorrelated.

Once the wavelet analysis had been applied to the mole fraction measurements, the data were converted to propane mass fraction values ($Y(i,t)$) using

$$Y(i,t) = \frac{\rho_p X_p(i,t)}{\rho_a[1-X_p(i,t)] + \rho_p X_p(i,t)} \quad , \tag{21}$$

where ρ_p and ρ_a are the densities of propane and air, respectively. The results were displayed as images for qualitative evaluation. Average and rms values were calculated as a function of radial position.

Radial and axial components of scalar dissipation values were also calculated from the data. The radial component was determined directly using a finite difference approach to calculate the necessary radial component of mass fraction gradient appearing in Eq. (2),

$$(\chi_r)_{i,j} = 2D\frac{\left[Y_{i+1,j}-Y_{i,j}\right]^2}{\Delta r^2} \tag{22}$$

where the i and j indices refer to radial direction and time, respectively, and $\Delta r = 113$ μm is the spacing of the line camera pixels. The calculation provides χ_r values for 127 radial locations.

A form of Taylor's Hypothesis was used to estimate the axial component of the scalar dissipation. Similar approaches have been used by Dowling[49] to estimate the axial scalar dissipation rate component from real-time single-point measurements and by Effelsberg and Peters[45] to estimate the scalar dissipation in a plane from real-time two-point measurements. Recent work by Mi and Antonia[123] and Dahm and Southerland[124] has provided direct experimental tests for the validity of Taylor's hypothesis. Both groups found that the effect of the approximation is to overestimate the average value of the axial component as compared to the value measured directly. The approximation is most accurate on the jet centerline, while the validity decreases dramatically with radial distance. The centerline estimate for $\overline{\chi}_z$ is within 10 % of the actual value.[123] Time records shown in Dahm and Southerland indicate that the largest absolute values of the axial component of the scalar gradient are consistently overestimated. This suggest a finite correlation between the magnitude of the axial component of the scalar gradient and the instantaneous velocity.

Velocities used for the calculation were the time-averaged local velocities conditioned by the intermittency function, $\overline{U}_t$. These values correspond to the average velocity only during the periods when turbulent fluid is present. Conditioned values were required to prevent the calculated values of χ_z from "blowing up" at the edges of the jet where both the intermittency function and $\overline{U}$ values become very low. The expression used to calculate values of χ_z was

$$\left(\chi_z\right)_{i,j} = 2D\frac{(Y_{i,j+1}-Y_{i,j})^2}{\overline{U}_t^{\,2}(\Delta t)^2} \quad , \tag{23}$$

where Δt = 420 μs is the time between line scans and $\overline{U}_t$ was estimated as

$$\overline{U}_t = \frac{\overline{U}_m h\left(\frac{r}{z}\right)}{\gamma} = \frac{U_o r_\epsilon}{k_u z \gamma} e^{-0.693\left(\frac{r}{(r_{1/2})_u}\right)^2} \quad . \tag{24}$$

The time-averaged centerline velocity, $\overline{U}_m$, was calculated in the same way as above assuming the virtual origin was located at the nozzle exit. The normalized radial velocity profile, $h(r)$, was approximated as a Gaussian function having a half width at half maximum of $(r_{1/2})_u$. The intermittency function, γ, was estimated using the expression given by Pitts and Kashiwagi,[3]

$$\gamma = 0.5 erfc\left(\frac{r-\overline{R}}{\sqrt{2}\sigma_w}\right) \quad , \tag{25}$$

where $\overline{R}$ = 1.6$(r_{1/2})_c$ and σ_w = 0.28$(r_{1/2})_c$.

Once values for the axial and radial scalar dissipation components were available, time records for a given r value could be averaged and pdfs generated from the time records. The two components of scalar dissipation are added to give χ_p,

$$\chi_p = \chi_r + \chi_z \ , \tag{26}$$

the local two-dimensional scalar dissipation in the r-z plane.

The angle (in radians) for the clockwise direction, Θ, between the primary flow direction, z, and the concentration gradient in the r,z plane was also determined. Buch and Dahm have reported similar results for a water jet.[38,47] The first step was the calculation of the radial and axial components of the mass fraction gradient given by

$$y_r' = \frac{\partial Y}{\partial r} \tag{27}$$

and

$$y_z' = \frac{\partial Y}{\partial z} \ , \tag{28}$$

respectively. These components were estimated in the same way as in the scalar dissipation calculations (see Eqs. 21 and 22). Once these values were available, the angles were determined using the following conditions:

$$\begin{aligned}
\Theta &= \arctan(y_r'/y_z') && \text{when } y_r' \geq 0,\ y_z' \geq 0 \\
\Theta &= \frac{\pi}{2} + \arctan(y_r'/y_z') && \text{when } y_r' \geq 0,\ y_z' < 0 \\
\Theta &= \frac{\pi}{2} + \arctan(y_r'/y_z') && \text{when } y_r' < 0,\ y_z' < 0 \\
\Theta &= 2\pi + \arctan(y_r'/y_z') && \text{when } y_r' < 0,\ y_z' \geq 0
\end{aligned} \ . \tag{29}$$

Images of the angles as a function of radial location and time were created using an eight-level false-color scale.

III. RESULTS

Five sets of measurements recorded along different radial sections of the jet profile at z/r_o = 40 are discussed. Figure 7 shows the measured time behavior of propane mass fraction for one of the data sets situated near the center of the jet. The data are presented as a two-dimensional image where the horizontal axis represents the radial direction, and the vertical axis corresponds to time. Propane

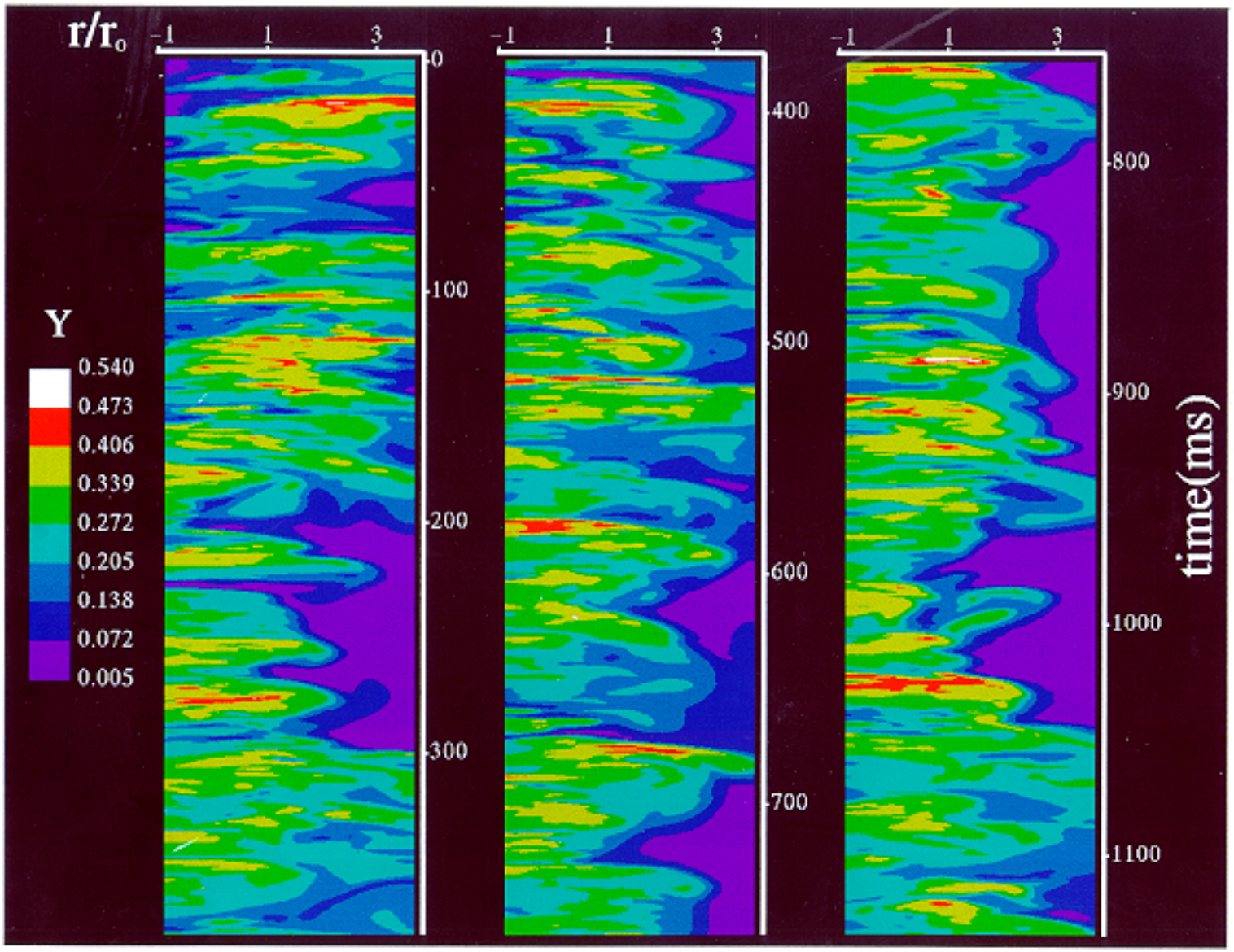

Figure 7. Time records of propane mass fraction (represented by an eight–level false–color scale) are shown for 128 adjacent points extending from $r/r_o = -0.89$ to 3.69. The axial location is $z/r_o = 40$.

mass fraction is represented by an eight-level false-color scale which covers the range of mass fractions observed. The displayed time record has a total duration of 1.13 s (i.e., 2700 out of a total 3000 scans are shown).

The four remaining mass fraction images are shown together in Fig. 8. The five sets of data shown in Figs. 7 and 8 partially overlap and, taken together, cover the entire radial extent of the jet. The time records for each pixel have been time averaged over the 3000 scans, and the resulting mass fraction average and rms values are plotted as functions of radial position in Figs. 9 and 10, respectively. The solid lines in the plots represent the predicted behaviors assuming the flow is self similar with a virtual origin located at $z = 0$. The radial profiles used for the calculations are taken from Richards and Pitts.[4] The dependencies on radial distance are reproduced well, but it is clear that the agreement is not perfect. Differences between the experimental data and predicted behaviors are particularly evident at the edges of the jet and in the rms behavior near the jet centerline. Even though each average and rms is formed from 3000 measurements, the data are recorded over the relatively short time of 1.26 s. Based on the criteria of Dowling and Dimotakis[67], the average passage time, τ_{jd}, for a large-scale structure can be estimated as the local jet diameter, L_{jd}, normalized by the time-averaged centerline velocity, i.e.,

$$\tau_{jd} = \frac{L_{jd}}{\overline{U}_m} . \tag{30}$$

Defining L_{jd} to be

$$L_{jd} = 0.44z \tag{31}$$

leads to an estimate of $\tau_{jd} = 0.051$ s for $z/r_o = 40$. During the 1.26 s period for the data collection, only 25 LSTSs are estimated to pass through the observation volume. Due to intermittency, the number of passages at the outer edges of the flow is much lower than nearer the center. It is likely that the major differences between the similarity curves and experimental measurements are the result of statistical nonconvergence. Minor differences may also arise from assuming z_o lies at $z = 0$.

Strong temporal and spatial variations in propane mass fraction due to turbulent mixing are evident in each of the images in Figs. 7 and 8. The presence of large-scale structures is suggested by the organization of the concentration field which can be seen over significant fractions of the full radial extent of the images (14.5 mm, 4.6 r_o). Due to intermittency at the outer edge of the flow, the passage of large-scale structures is particularly evident in images a, c, and d of Fig. 8. In general,

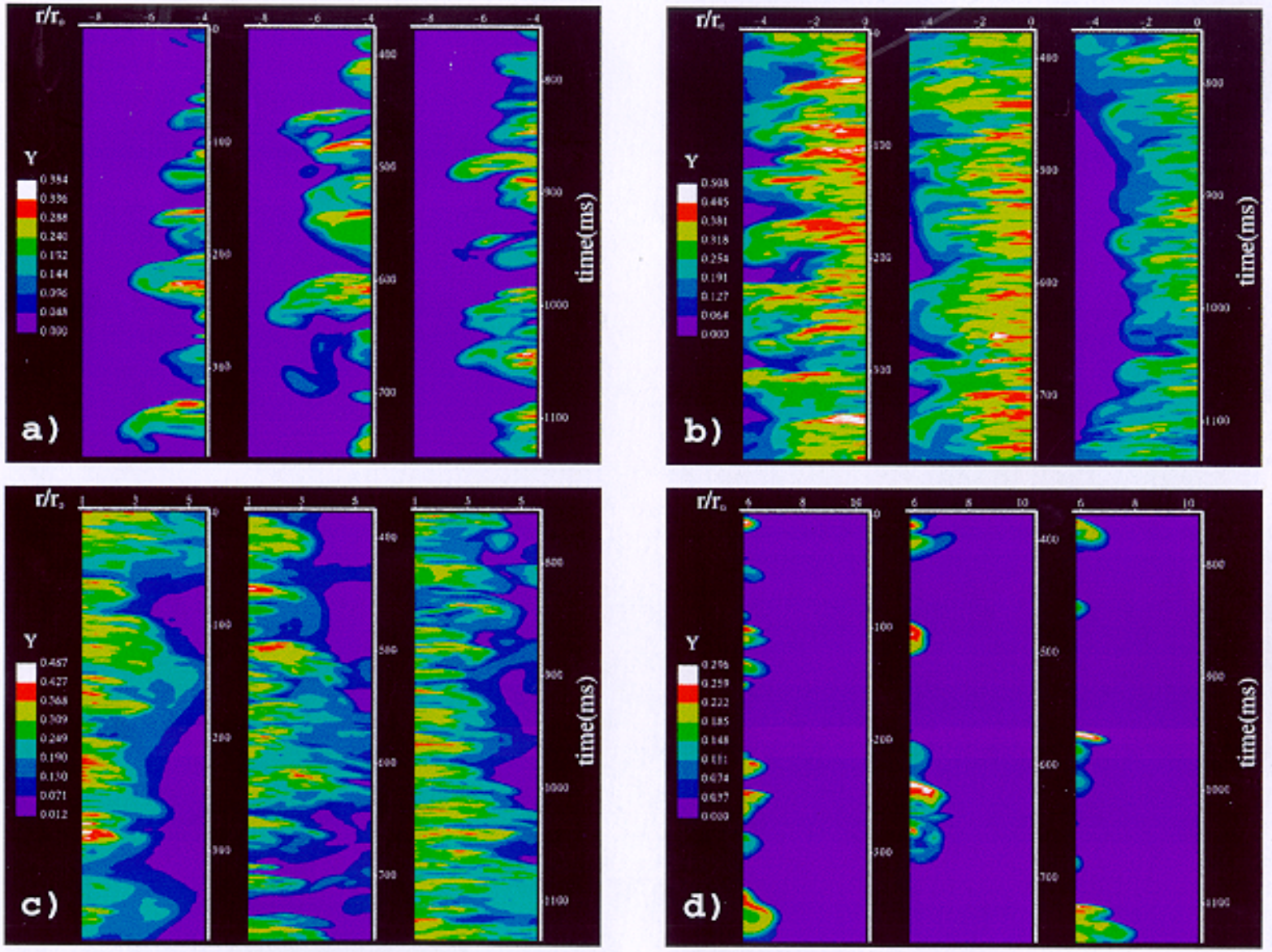

Figure 8. Time records of propane mass fraction (represented by eight–level false–color scales) along lines formed from 128 pixels positioned at four different radial locations across the jet flow are shown. The axial location is $z/r_o = 40$.

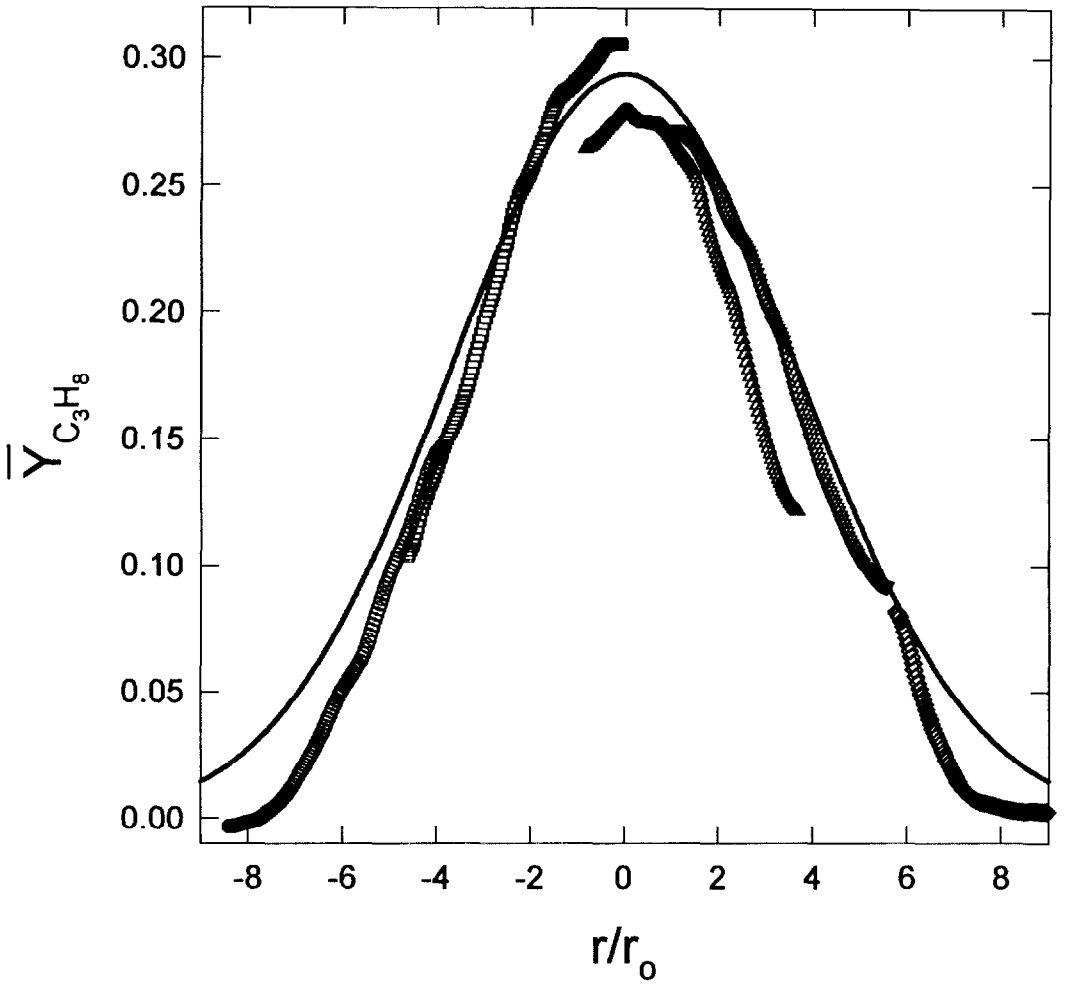

Figure 9. Time-averaged values of propane mass fraction based on line camera measurements at five radial locations are plotted as a function of the radial distance from the jet centerline. The solid curve is the expected behavior assuming a self-similar flow with a virtual origin at the jet exit.

concentrations tend to be high on the leading (downstream) edges of these structures and to fall towards the rear(upstream) edges. This observation is consistent with earlier observations of ramp-like structures in concentration time records of single-point measurements, and demonstrates that the ramp-like structures in this region of the flow field are indeed due to organized LSTS.[3,18,24]

The radial position of the outer edge of the jet fluid varies substantially during the 1.13 s periods shown in the figures. Consider the data shown in Fig. 8b. For times between 0 and 400 ms, the structures extend well beyond $r/r_o = -4$. From 400 to 800 ms the radial extent of the structures is about $r/r_o = -4$. For times greater than 800 ms, the jet necks in, and the jet fluid extends only to $r/r_o = 3$. Such behaviors can be seen in all of the mass fraction images. The record length for a single

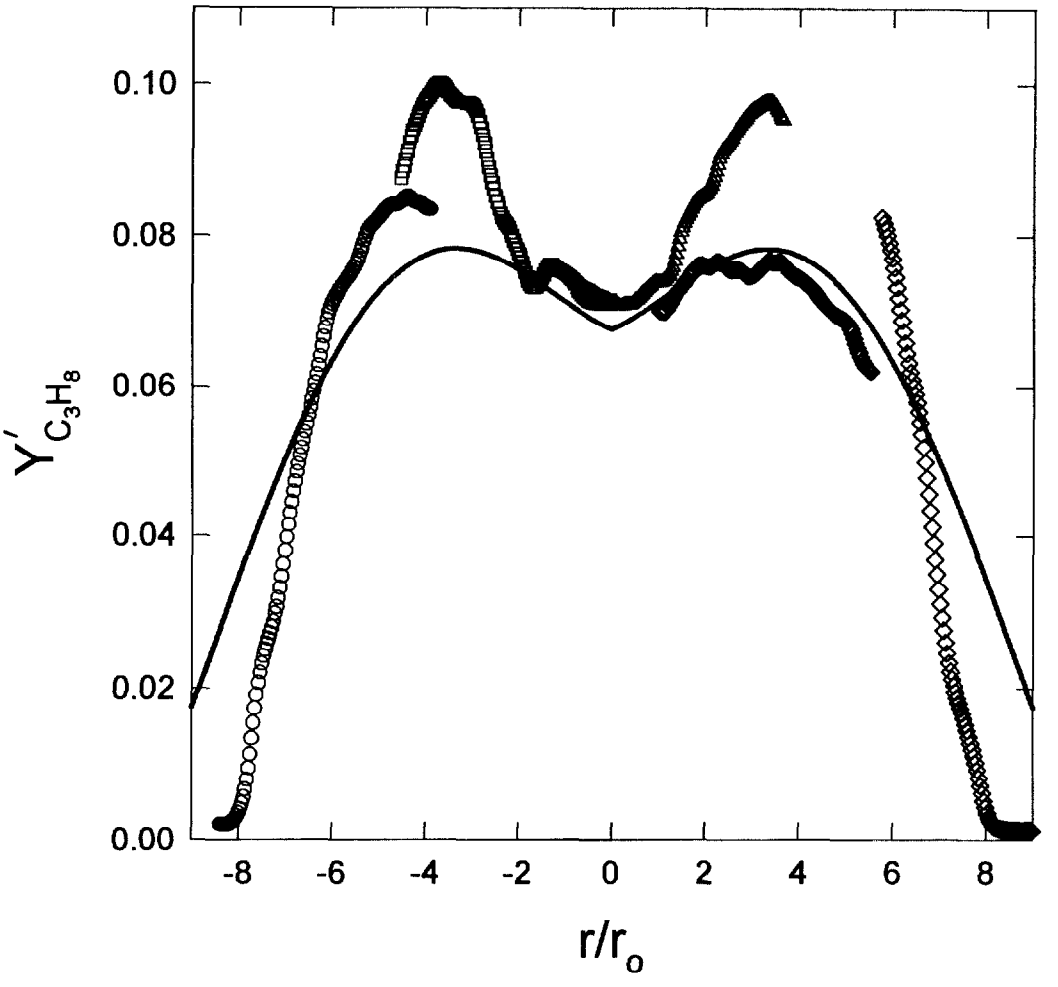

Figure 10. Root mean square values of propane mass fraction based on line camera measurements at five radial locations are plotted as a function of radial distance from the jet centerline. The solid curve is the expected behavior assuming a self-similar flow with a virtual origin at the jet exit.

data set, 3000 scans, is insufficient to identify any temporal pattern or frequency for the movement of the outer edge of the jet.

In Fig. 11 the two data sets located nearest the jet centerline are replotted using a three-level false-color scale chosen to highlight the possible presence of JCLSOSs which have been previously reported to extend across the entire jet diameter in water jets by Dimotakis et al.[17] and Papantoniou and List[23]. The three levels are based on centerline average, $\overline{Y}_m$, and rms, Y'_m, mass fractions and represent concentrations which are less than $\overline{Y}_m - Y'_m$ (blue), fall between $\overline{Y}_m - Y'_m$ and $\overline{Y}_m + Y'_m$ (green), and are greater than $\overline{Y}_m + Y'_m$ (red). If present, the full-diameter FJLSOSs should result in regions of the images where high concentration and low mass fractions are localized close together and which appear

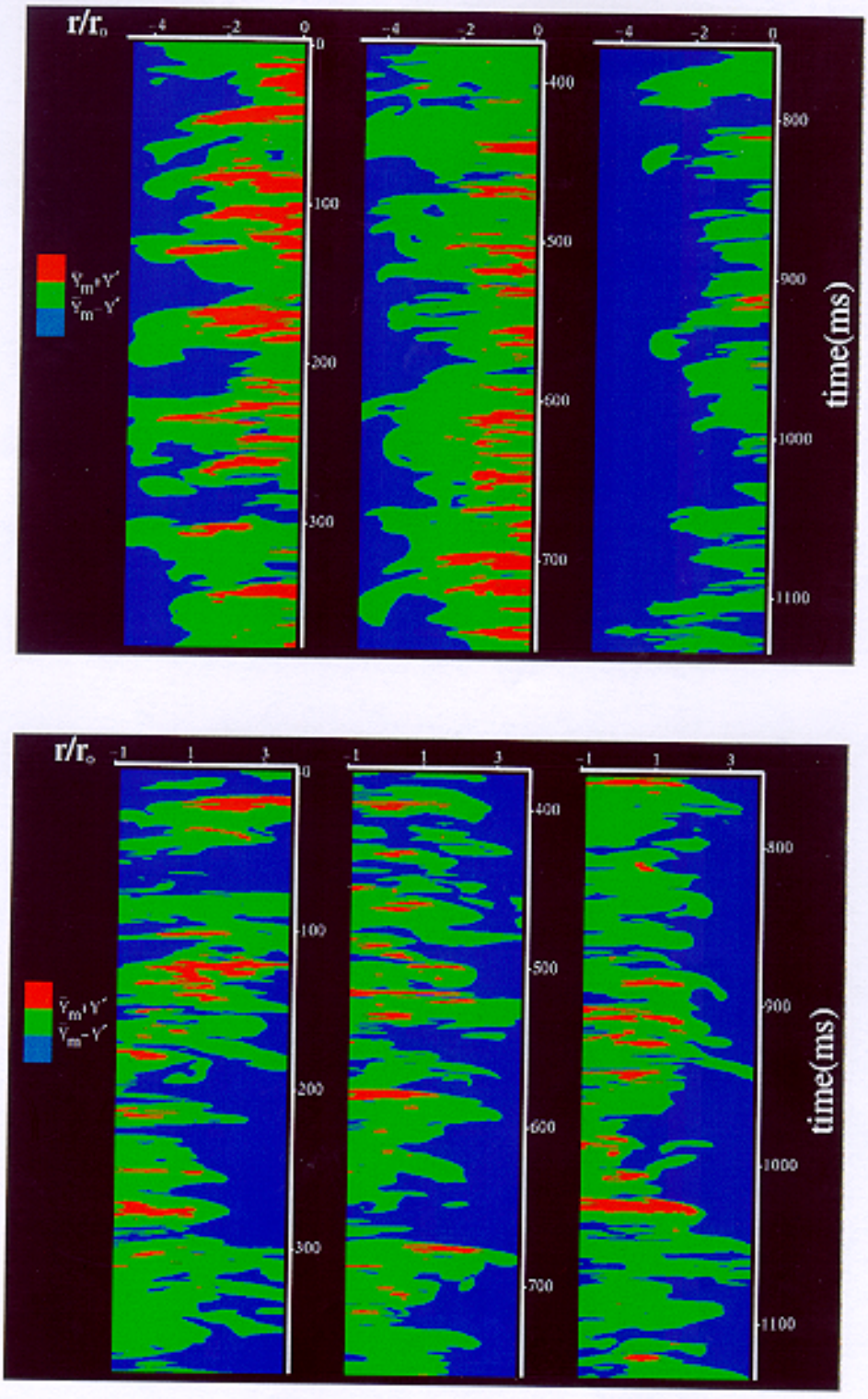

Figure 11. Propane mass fraction values for 128 radial locations are plotted as a function of time for the two data sets recorded with the line camera observation volume located nearest the jet centerline. Mass fraction is represented by a three–color false–color scale where a given mass fraction values is less than or equal to $\overline{Y}_m - Y_m'$ (blue), falls between $\overline{Y}_m - Y_m'$ and $\overline{Y}_m + Y_m'$ (green), or is greater than or equal to $\overline{Y}_m + Y_m'$ (red).

repetitively at a frequency which is roughly the inverse of the expected time required for the passage of the structures, $f_{jd} \approx 20\ s^{-1}$ for $\tau_{jd} = 0.051$ s. It is clear from the figure that regions of both high and low concentrations do occur near the jet centerline. However, it is not obvious that the occurrences of high and low concentration regions are correlated or that they occur at a distinct frequency having a period of roughly $1/\tau_{jd}$. Based on the limited data reproduced here, JCLSOSs are not nearly as evident for a propane jet entering air as for the high Sc flows discussed in the Introduction.

Figure 12 shows the behavior of the radial component of scalar dissipation for the mass fraction results reproduced in Fig. 7. The data are displayed as a r-t image using an eight-level false-color scale to represent χ_r on a base 10 logarithm scale. This scaling is appropriate because of the extensive range (> 8 orders of magnitude) covered by the χ_r values, as well as the fact that scalar dissipation pdfs are often fit to log-normal distributions. The lower limit is set to $\log(\chi_r) = -4$ because noise in the measurements becomes more evident for lower values.

Images of $\log(\chi_r)$ for the four remaining data sets are combined in Fig. 13. Several trends are evident in the five images reproduced in Figs. 12 and 13. As the sampling position moves outward from the jet centerline, the appearance of the images changes dramatically. Continuous regions of high χ_r (marked by red and white) which extend over significant fractions of the jet width become evident. The majority of these regions have similar "fishhook" shapes, appearing as narrow, well defined bands which are roughly linear for locations closer to the jet center and ultimately develop a convex curvature near the jet outer edge. The straight edges nearest the jet center are oriented with angles of roughly 100°-110° relative to the downstream axis (i.e., earlier times). In general, the regions of high $\log(\chi_r)$ do not form closed "loops" but instead tend to dissipate after reaching their maximum radial extent, even though it is often possible to discern the completion of a loop formed by significantly reduced χ_r values. A great deal of apparently organized structure is usually present in the areas "enclosed" by these large structures. Similar structures near the edge of a methane jet are evident in an instantaneous two-dimensional image of χ_r shown by Schefer et al.[28]

Additional, more subtle, effects are also present in the images. In regions of the jet closer to the centerline there are two distinct alternating periods during which χ_r values first display very intense, apparently random, small-scale temporal and spatial variations, followed by ones during which the variations in χ_r are much less vigorous and relatively constant values of χ_r (as indicated by an area of the same color) exist over larger temporal and spatial time scales. The periods between 100 ms and 160 ms and just before 300 ms in Fig. 12 are good examples of the first type of behavior, while the periods around 50 ms and 350 ms are representative of the second. While these descriptions are qualitative in nature, the behaviors are distinct enough to suggest that there are significant differences

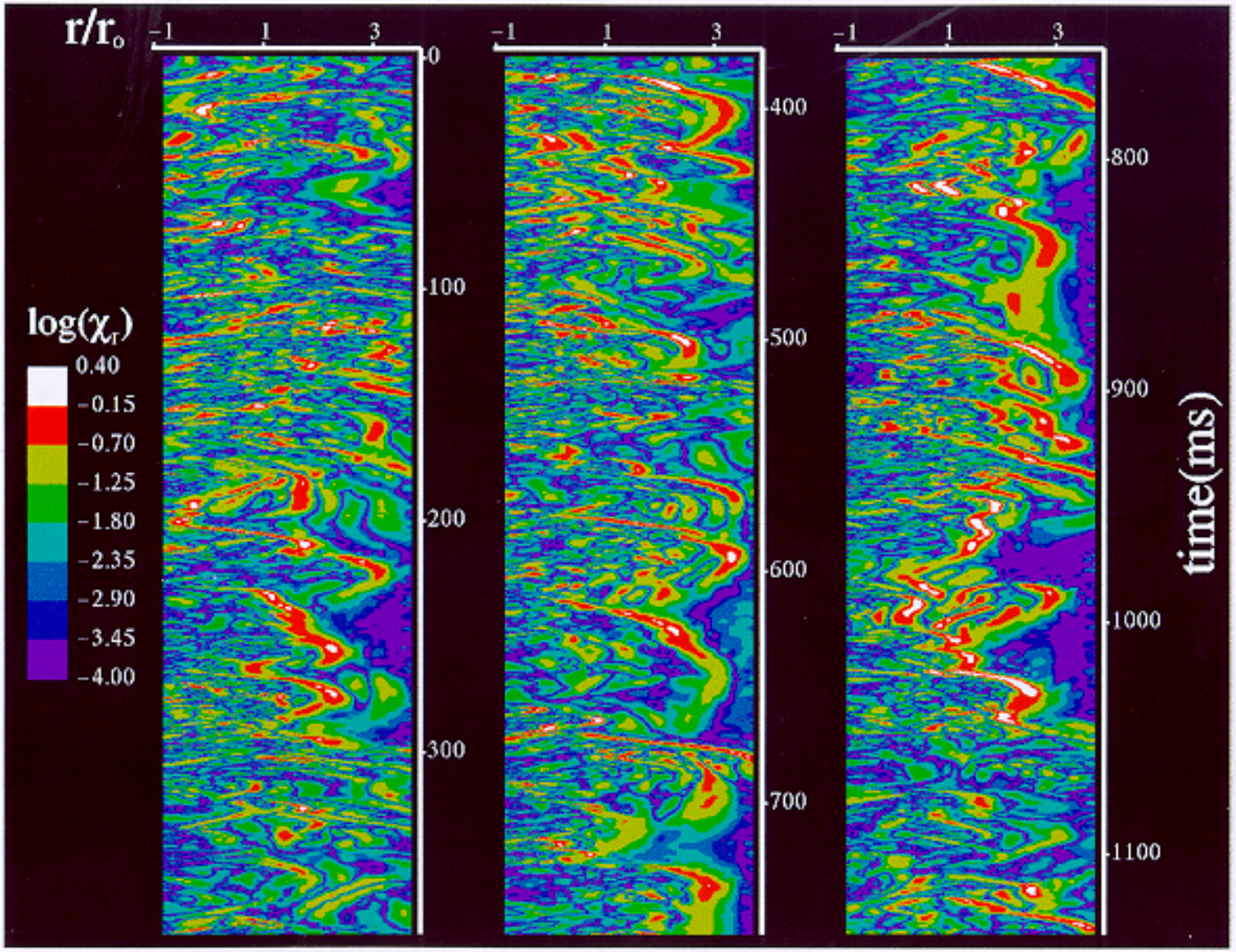

Figure 12. The time behavior of $\log(\chi_r)$, represented by a eight–level false–color scale, is shown for 128 adjacent points extending from $r/r_o = -0.89$ to 3.69. The axial location is $z/r_o = 40$.

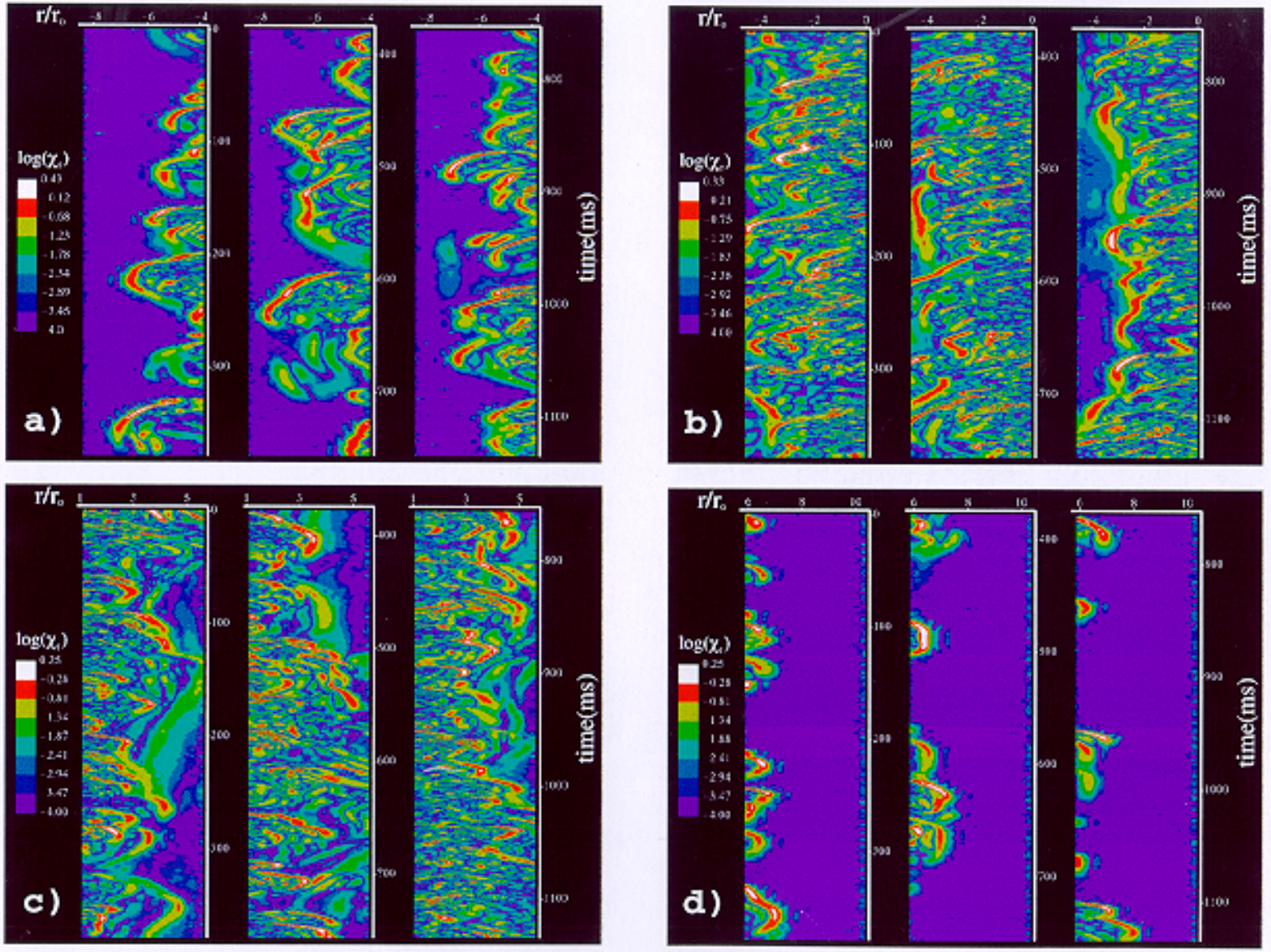

Figure 13. Time records of log(χ_r) (represented by eight–level false–color scales) along lines positioned at four different radial locations across the jet flow are shown. The axial location is $z/r_o = 40$.

in mixing mechanisms and rates for regions of the flow field undergoing high and low intensity χ_r fluctuations.

The mass fraction images shown in Fig. 11 failed to provide convincing evidence for the presence of JCLSOSs in the flow field. However, hints for the presence of such structures can be found in the χ_r images. Again considering Fig. 12, there are numerous examples of short periods during which particularly high values of χ_r occur across the entire width of the image. Examples are observed near (36, 118, 205, 308, 495, 582, 670, 800, 872, 921, 1020, and 1118) ms. While high values of χ_r are clustered across the observed region, there are frequent discontinuities and breaks. These breakups seem to be more likely near the jet centerline. The discontinuities in high scalar dissipation regions could be responsible for the inability to easily discern JCLSOSs in Fig. 11. It is interesting that while some of the high χ_r clusters are clearly associated with fishhook LSTSs at the jet's outer edge, at other times such a correlation is not evident. Note that similar behaviors are evident in Figs. 13b and c.

At the outer edge of the jet, such as emphasized in Figs. 13a and d, the mixing within and upstream of the fishhook structures is much less robust than closer to the centerline. In fact, the majority of the mixing seems to be result of "stirring" motions, using the description of Broadwell and Mungal.[35] The mixing behavior for the LSTSs observed near 500 ms and 650 ms in Fig. 13a are striking examples. The clear difference in mixing behavior between regions in the central region of the flow field and within the LSTSs at the jet's outer edge indicates that the structure of the turbulence in these two regions is quite different.

The effectiveness of wavelet analysis in reducing noise due to the limited digitization range of the experimental data is assessed in Fig. 14, where χ_r images determined from mass fraction data both before (a) and following (b) application of wavelet analysis are compared. The improvement due to the use of wavelets is dramatic. Regions of high χ_r are evident in both Figs. 14a and 14b, but regions of smaller χ_r which are impossible to distinguish in the untreated data are clearly discernible in Fig. 14b. A simple analysis in which the propane concentration along the radial direction is assumed to be constant, and which uses the experimentally observed individual pixel signals for scattering from air and propane (see Fig. 3), allows the magnitude of the expected variations in mass fraction due to the limited digitization range to be estimated. The resulting fluctuations in χ_r can then be determined by differentiating and applying Eq. (21). The variations in χ_r appear to be random with values centered near $\log(\chi_r) \approx -3$. Such levels are consistent with the noise evident in Fig. 14a.

The wavelet analysis does introduce some artifacts into the results shown in Figs. 12 and 13. These are most evident at the jet edges such as in Figs. 13a and 13d where there are small areas of

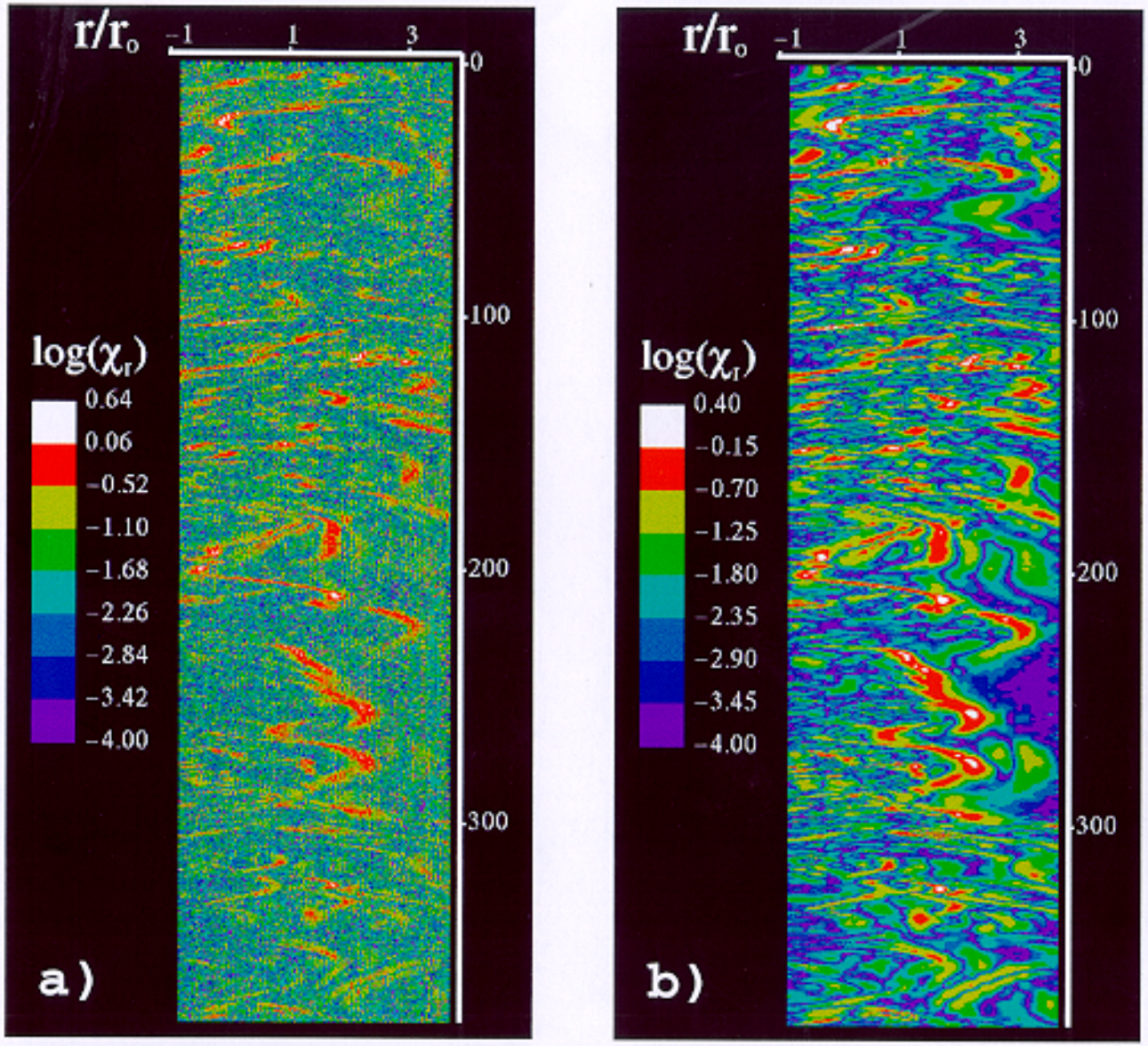

Figure 14. Line measurements of $\log(\chi_r)$ are plotted as a function of time for a period of 0.38 s using the propane mass fraction results reproduced in Fig. 7. The two frames show the results of the calculations using the data before (a) and after (b) the application of wavelet analysis.

slightly increased χ_r along the high concentration edges of the LSTSs. The appearance of these artifacts seems to be associated with a fixed pattern noise in the camera which is barely observable in the data before the wavelet analysis is applied. Even though the structures appear to be prominent, it should be kept in mind that a value of $\log(\chi_r) = -4$ corresponds to a mass fraction difference of 0.00023 between adjacent pixels. A second artifact results from the procedure employed to remove the voltage ramps present in the line camera. The procedure is not perfect, and the residual signals result in nonreal increases in values of χ_r which appear occasionally over short distances in individual radial scans. Again, the increases in χ_r are small, indicating that the correction for the voltage ramps, while not perfect, is effective. Finally, some structure is evident at the edges of those images which are positioned well away from the jet centerline where χ_r values are expected to be vanishingly small (see Figs. 13a and 13b) since no propane is expected to be present. These small increases are associated with the end corrections employed during the wavelet analysis. Even though some noise is introduced by these corrections, it will shortly be shown that average values and pdfs for χ_r do not appear to be affected by the correction procedure.

The large number of measurements precludes detailed consideration of either temporal or radial profiles. However, it is worthwhile to consider a few cases to obtain insight into the observed behaviors. Figure 15 shows the time dependence of Y, χ_r, and $\log(\chi_r)$ over a 200 ms time period at the radial location $r/r_o = 0$ for the data shown in Fig. 12. The wavelet-corrected mass fraction values are smooth, and there is little indication of noise in the measurements. The corresponding values of χ_r fluctuate at a much higher frequency. Most values of χ_r are relatively low, but there are short periods during which much larger values occur. When the χ_r are plotted on a log scale, the time record has a much more random appearance, and it is clear that the average value of $\log(\chi_r)$ lies near -2.

Time records for individual radial locations were used to generate pdfs of $\log(\chi_r)$ along with average and rms values. Figure 16 shows two pdfs of $\log(\chi_r)$ calculated from single pixels at $r/r_o = 0$ using the data shown in Figs. 12 and 13b. While there is some scatter in the results, the two pdfs agree fairly well. In an effort to reduce the scatter observed for pdfs from single pixels, eight time records located within $0.1r_o$ of $r/r_o = 0$, corresponding to 24,000 individual measurements, were combined and used to generate the pdf for $\log(\chi_r)$ shown in Fig. 17. It can be seen that the resulting pdf is well defined with sharply reduced noise compared to the individual pdfs in Fig. 16. The pdf is clearly asymmetric with a long tail extending towards low values of $\log(\chi_r)$. Average and rms values for the data represented by the pdf in Fig. 17 are -2.329 and 1.076, respectively.

Dahm and Buch[79] showed that pdfs for $\log(\chi_z)$ approximated from real-time single-point mass fraction measurements by Dowling and Dimotakis[125,126] had very similar shapes to that seen in Fig. 17.

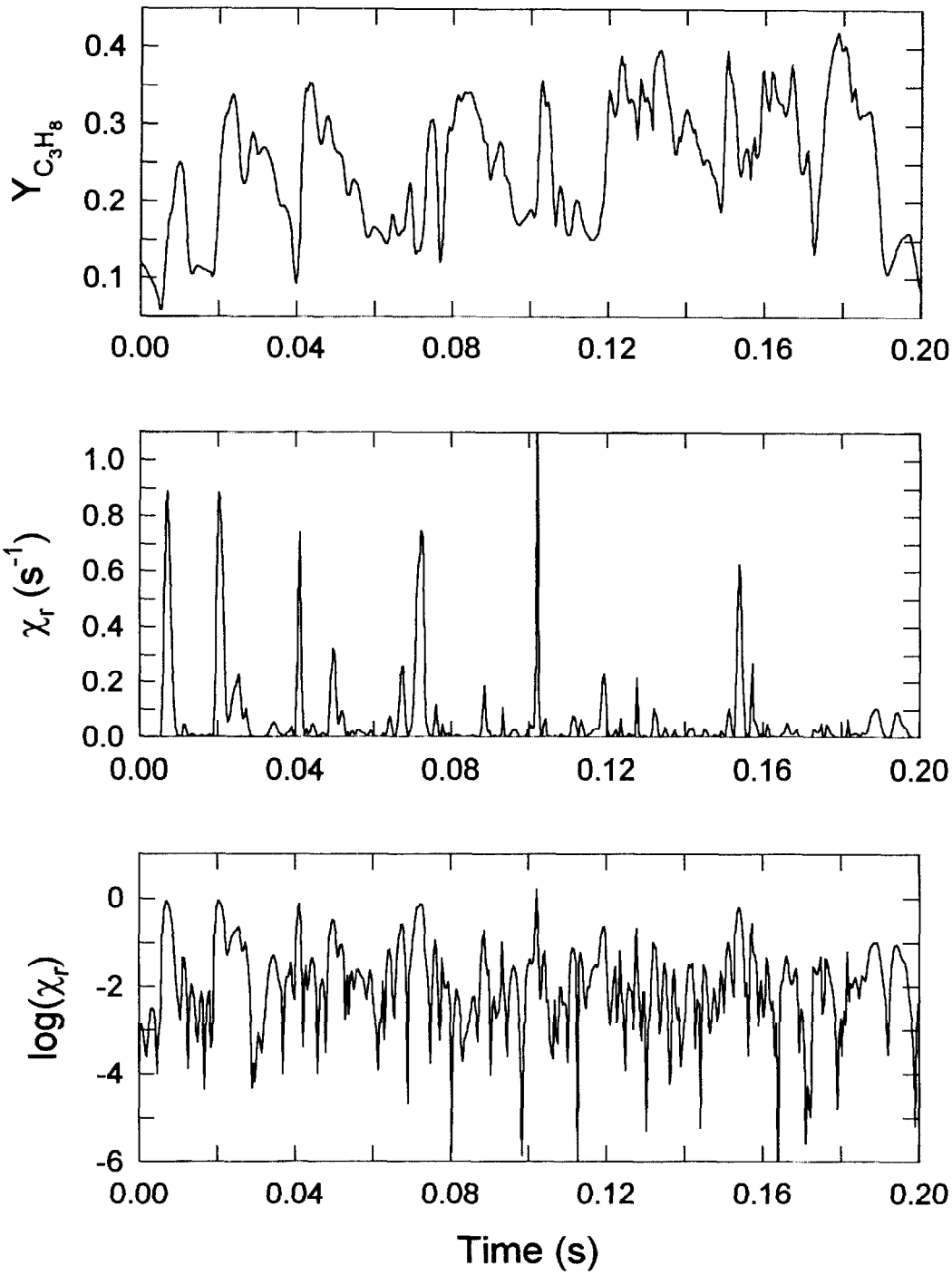

Figure 15. Centerline ($r = 0$) values of Y, χ_r, and $\log(\chi_r)$ are plotted for the mass fraction data shown in Figs. 7 and 12. Results for the first 200 ms of the time record are shown.

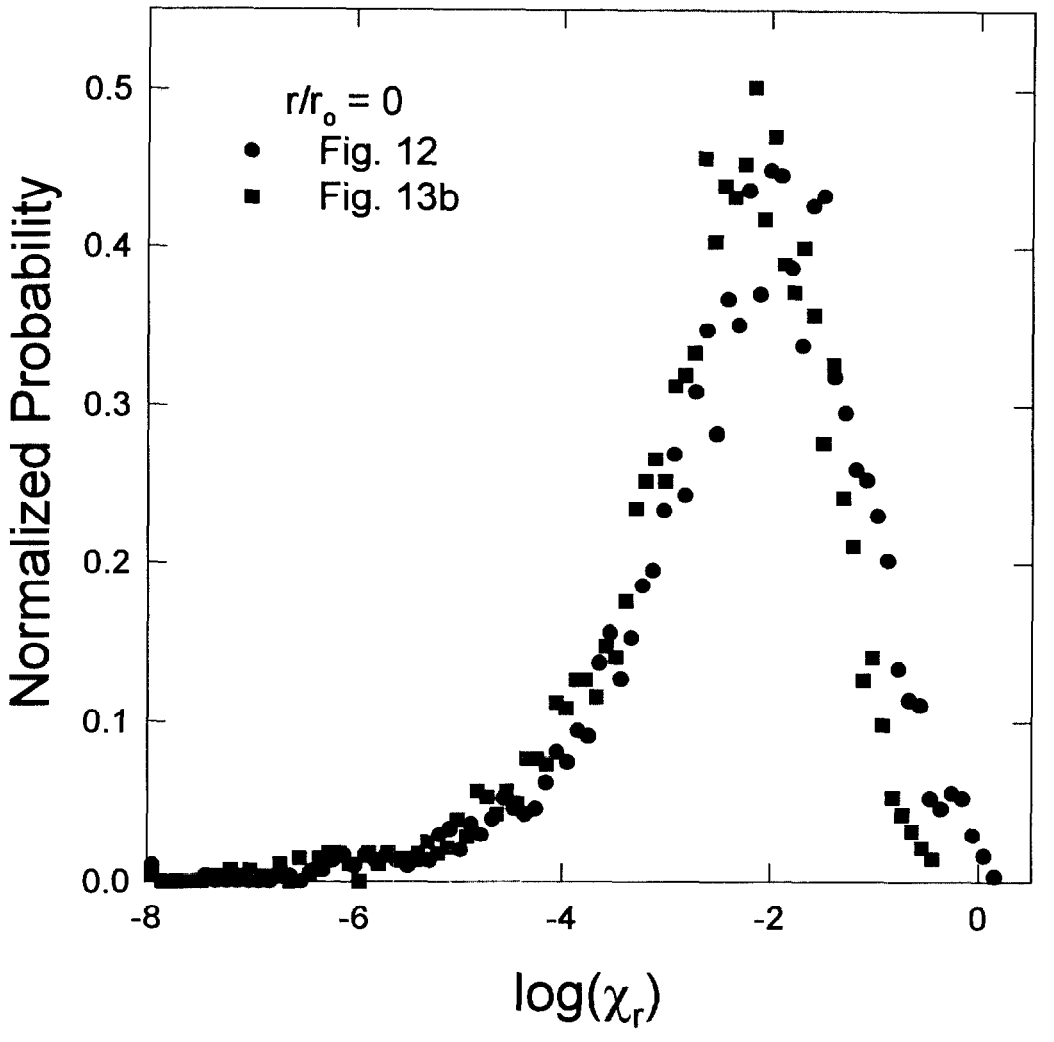

Figure 16. Two probability distribution functions of $\log(\chi_r)$ are shown for the pixels corresponding to the jet centerline locations in Figs. 12 and 13b.

They performed an analysis which demonstrated that such a shape is to be expected when a single component of a log-normally distributed χ is experimentally determined. A mathematical prescription, based on assuming that χ is isotropic, was provided for calculating the corresponding $\log(\chi)$ pdf from the pdf for the log of one of the three components, i.e., $\log(\chi_{1D})$.

It was confirmed that the algorithm of Dahm and Buch is capable of generating the desired three-dimensional pdf, but it was found that the mathematical procedure is very sensitive to noise in the one-dimensional pdf and easily becomes numerically unstable. As an alternative, a reverse transformation has been used in which a log-normal distribution is assumed for χ and is then used to calculate the expected distribution of χ_{1D} by numerically integrating the expression derived by Dahm

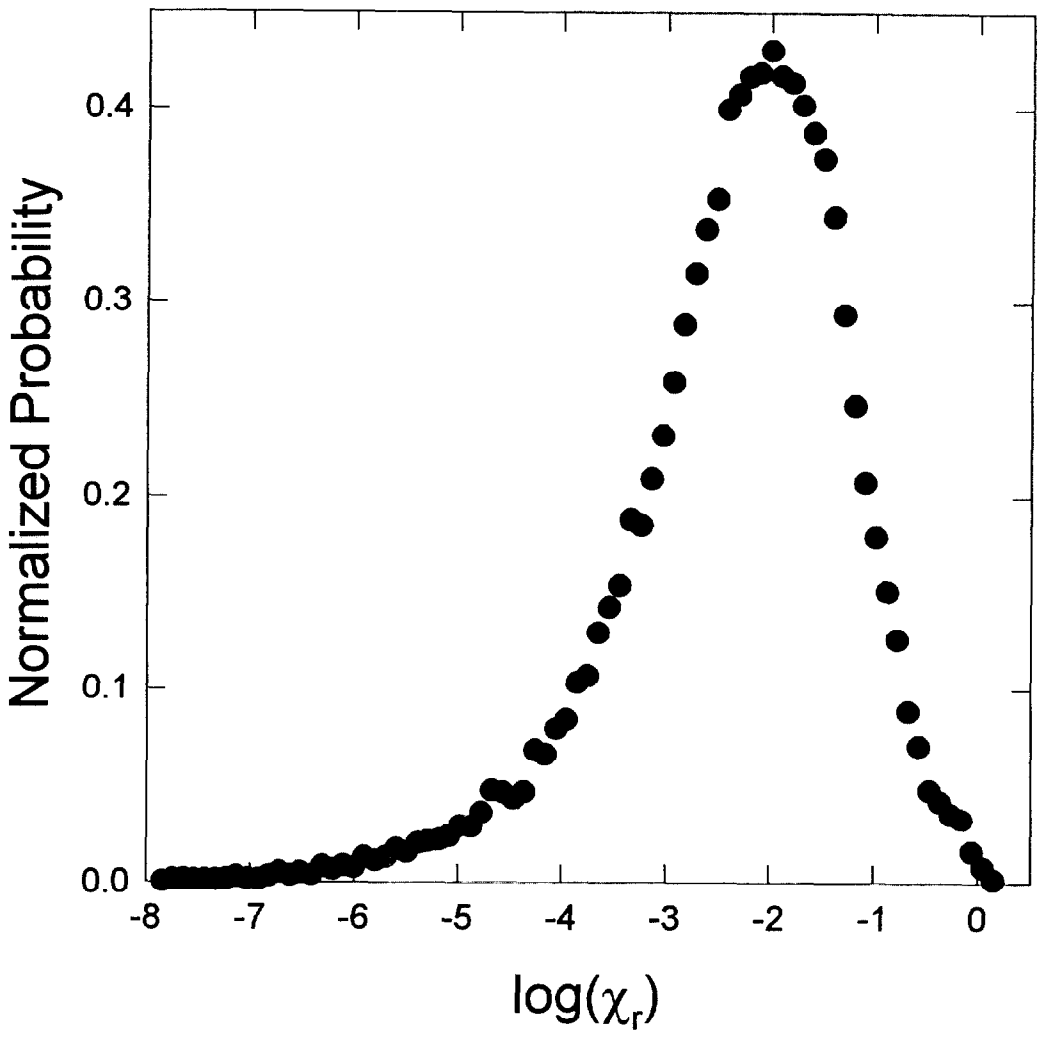

Figure 17. The pdf for $\log(\chi_r)$ is shown for 24,000 measurements recorded within $0.1r_o$ of the jet centerline in the propane jet.

and Buch[79] for the probability of measuring a value of χ_{1D} given a known value of χ,

$$\beta(\log\chi_{1D};\chi) = 1.15129\times 10^{0.5\log(\chi_{1D}/\chi)}, \tag{32}$$

over the assumed χ pdf. The values of the average and rms for the assumed log-normal distribution for χ were varied until the average and rms for the calculated distribution of χ_{1D} matched those for the experimental pdf shown in Fig. 17. It was found that assumed average and rms values for $\log(\chi)$ of -1.472 and 0.694, respectively, were required to generate a calculated distribution of $\log(\chi_{1D})$ having the required characteristics.

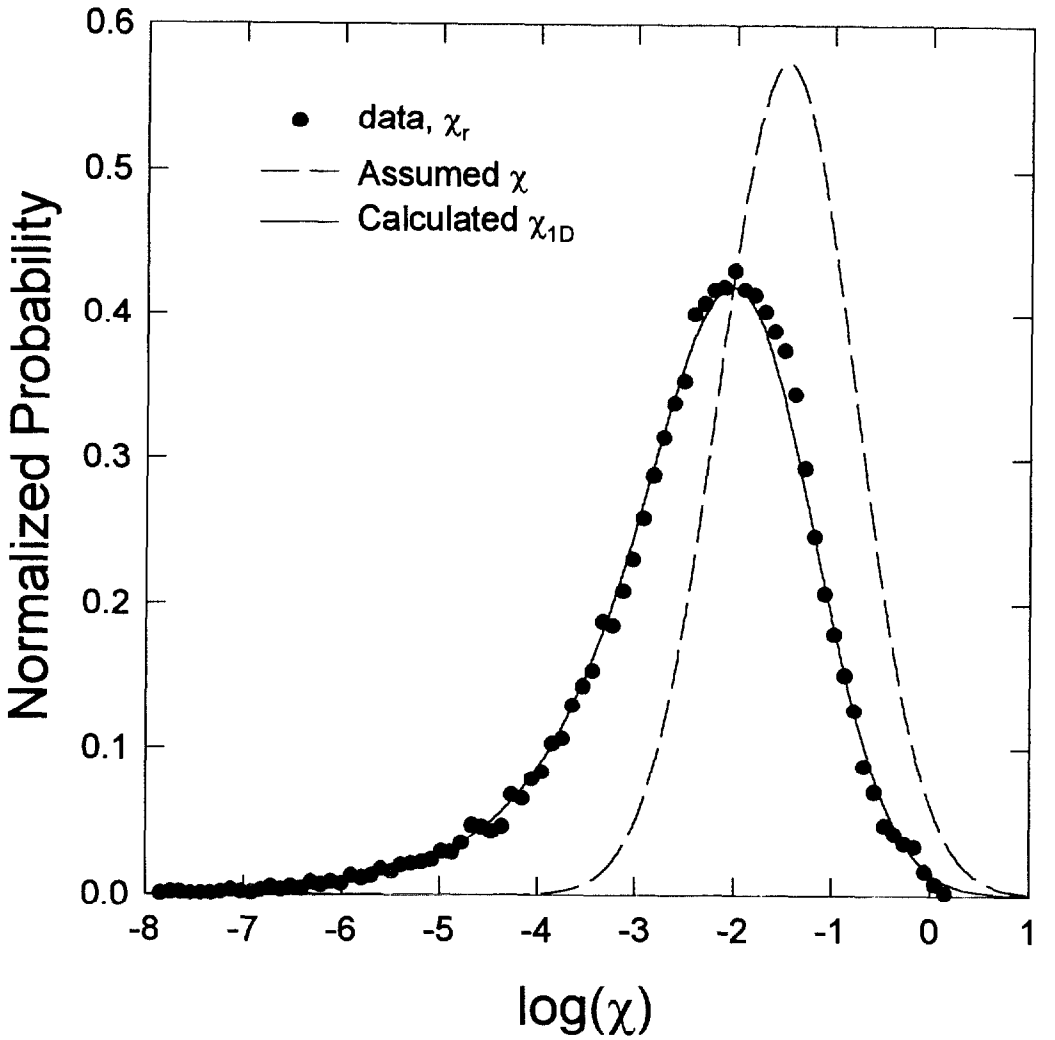

Figure 18. The experimental pdf (symbols) for $\log(\chi_r)$ is compared with an estimated pdf for $\log(\chi_{1D})$ (solid line) derived from an assumed log-normal distribution for χ (dashed line) having average and rms values of -1.472 and 0.694, respectively.

Figure 18 compares the assumed Gaussian distribution for $\log(\chi)$, the corresponding calculated distribution of $\log(\chi_{1D})$, and the experimental pdf for $\log(\chi_r)$. The agreement between experimental and calculated single-component distributions is very good. This is particularly true in the region of the long tail toward low values of $\log(\chi_{1D})$. The close match of the experimental and calculated distributions not only provides strong evidence that scalar dissipation near the jet centerline is isotropic, but also that the experimental measurements are accurately capturing the behavior of χ_r.

Dahm and Buch[79] noted that using a value of $3\chi_r$ for an estimate for χ as suggested by Eq.(3) results in a large underestimation of the true average and overestimation of the true rms for the log-normal distribution of $\log(\chi)$. Using this approximation, average and rms values for the distribution

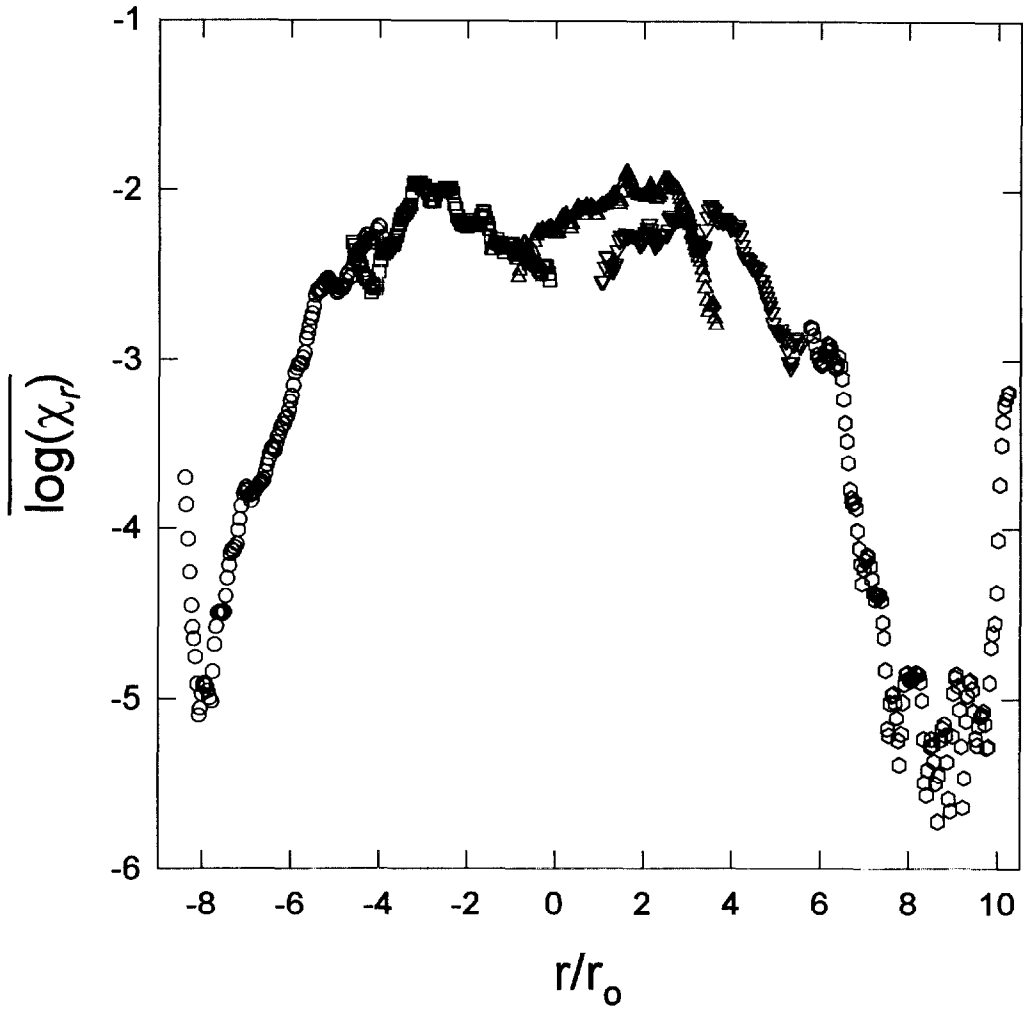

Figure 19. Average values of $\log(\chi_r)$ are plotted as a function of r/r_o for the five sets of data reproduced in Figs. 12 and 13.

would be estimated as -1.852 and 1.076, respectively. These values can be compared with those of -1.472 and 0.694 used to calculate the log-normal distribution shown in Fig. 18. The average value differs by a factor of nearly six and the rms value from the one-dimensionl approximation is 55 % larger.

Average and rms values of $\log(\chi_r)$ have been determined for each of the 127 pixel locations in the five images shown in Figs. 12 and 13. Averages are shown in Fig. 19 and rms values in Fig. 20. As observed previously for average and rms values of mass fraction, the overlap of individual sets of data is not complete. It is also clear that there are variations in average and rms values of $\log(\chi_r)$ within individual data sets. Nevertheless, general trends are evident in the results. Average values near the jet centerline are on the order of $\log(\chi_r) = -2.2$, and, as the sampling position moves

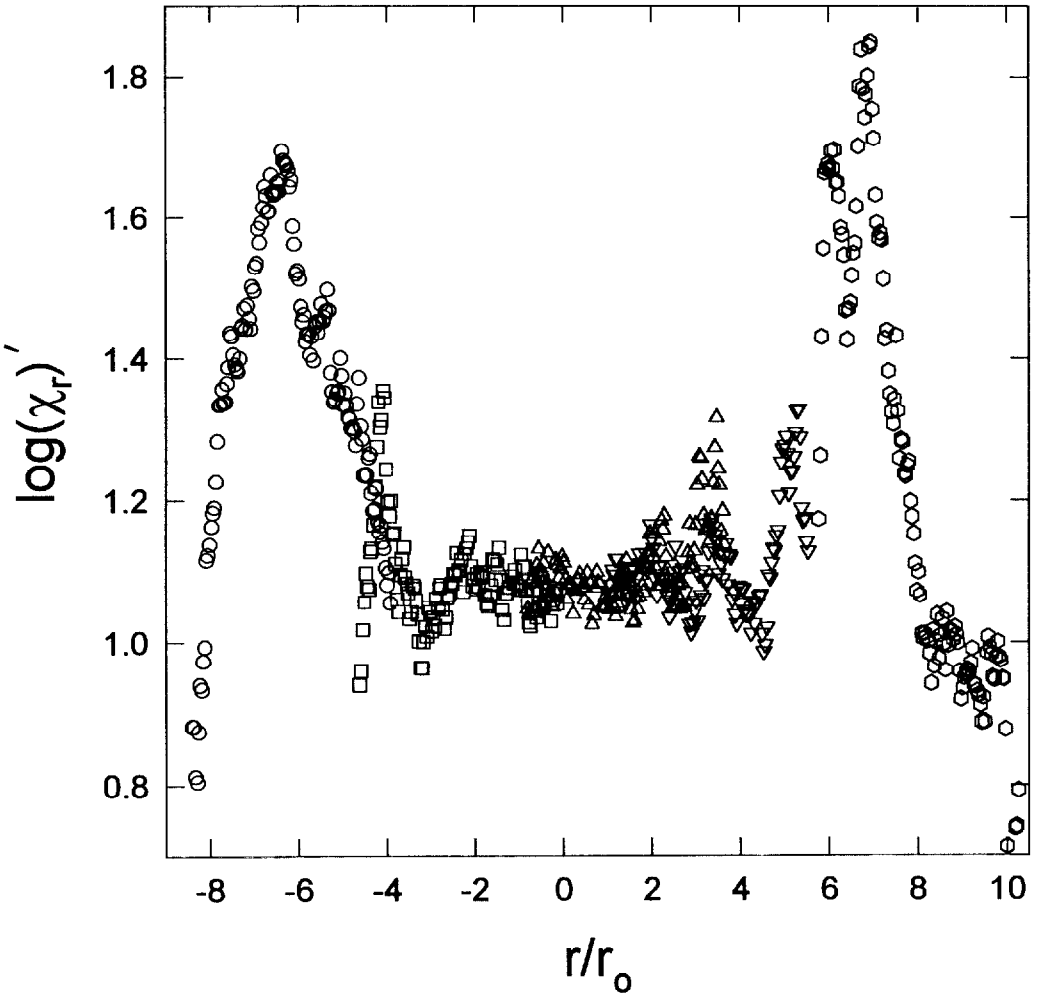

Figure 20. Root-mean-square values for $\log(\chi_r)$ are plotted as a function of r/r_o for the five sets of data reproduced in Figs. 12 and 13.

outward, the average first increases to a value of $\log(\chi_r) \approx -2.0$ for distances near $3r_o$ from the centerline, and then begins to fall rapidly for greater distances. Values for the rms for positions extending from $r/r_o = -4$ to $+4$ are nearly constant at $\log(\chi_r)' = 1.1$. At larger radial distances the rms values increase to a maximum which is roughly 70 % higher at $r/r_o \approx 7$ before falling rapidly at still larger radial distances.

Two points should be noted concerning measurements at the outer edges of the flow. First, for large distances from the centerline the average values fall to a minimum of $\log(\chi_r) \approx -5.2$. Since these measurements are actually recorded for positions where only air is expected to be present, this value reflects the inherent "noise" in the wavelet-treated data. Such values of $\log(\chi_r)$ correspond to a mass

fraction difference between adjacent pixels of 6×10^{-5}. Secondly, sharp increases in the averages are evident at the outer edges of the images. These result from the edge corrections applied during the wavelet calculations. Note, however, that these effects are not evident for positions closer to the jet centerline where the χ_r are the result of significant propane mass fraction fluctuations. This suggests that the end corrections do not result in significant errors in the average or rms values for measurement positions closer to the centerline.

The complexity of the structure evident in Figs. 12 and 13 makes generalizations concerning the nature of the mass fraction variations responsible for particular χ_r very difficult. However, it is informative to consider the nature of the concentration fluctuation behaviors responsible for the largest values of χ_r. Figure 21 shows three sequential radial profiles of propane mass fraction corresponding to times when the largest χ_r occur for each of the data sets shown in Figs. 12 and 13a-c. For each case the largest value of χ_r is the result of a very sharp drop (i.e., a "cliff") in mass fraction along the radial direction from relatively high values to very low values approaching ambient conditions. With the exception of one case, the cliffs are located near the instantaneous outer jet boundary. In each profile, the mass fraction is changing relatively slowly with time, and high values of χ_r exist immediately before and after the radial profile which generates the largest value of χ_r. In general, the radial locations of the cliffs are moving slowly away from the centerline with increasing time. Comparison of the profiles in Fig. 21 with the corresponding images in Figs. 12 and 13 suggests that the fishhook regions of high $\log(\chi_r)$ evident in the images are the result of this type of mass fraction radial distribution.

Figure 22 is a *r-t* image showing the behavior of $\log(\chi_z)$ for the mass fraction results displayed in Fig. 7. This image has a very different appearance from that for the corresponding radial component shown in Figs. 12. Values of $\log(\chi_z)$ have a distinct layered (or stratified) appearance with the layers aligned roughly in the radial direction. Regions of both high and low values of $\log(\chi_z)$ display this behavior. In many cases, layers of high $\log(\chi_z)$ continuously extend over much of the imaged region, including positions near the jet centerline. This behavior should be contrasted with that for $\log(\chi_r)$ where values were considerably more random and showed less evidence of organized large-scale structure near the jet center. Conversely, the extensive regions of high values of $\log(\chi_r)$ evident on the outer edge of Fig. 12 are not evident at all for the corresponding $\log(\chi_z)$ image.

Comparison of Figs. 12 and 22 shows that the temporally alternating periods of intense and relatively weak small-scale mixing are evident for both components of χ during the same periods. For the axial component there is a clear correlation of the magnitudes of $\log(\chi_z)$ and the two mixing behaviors, with high values of $\log(\chi_z)$ appearing to be much more likely during the intense periods and

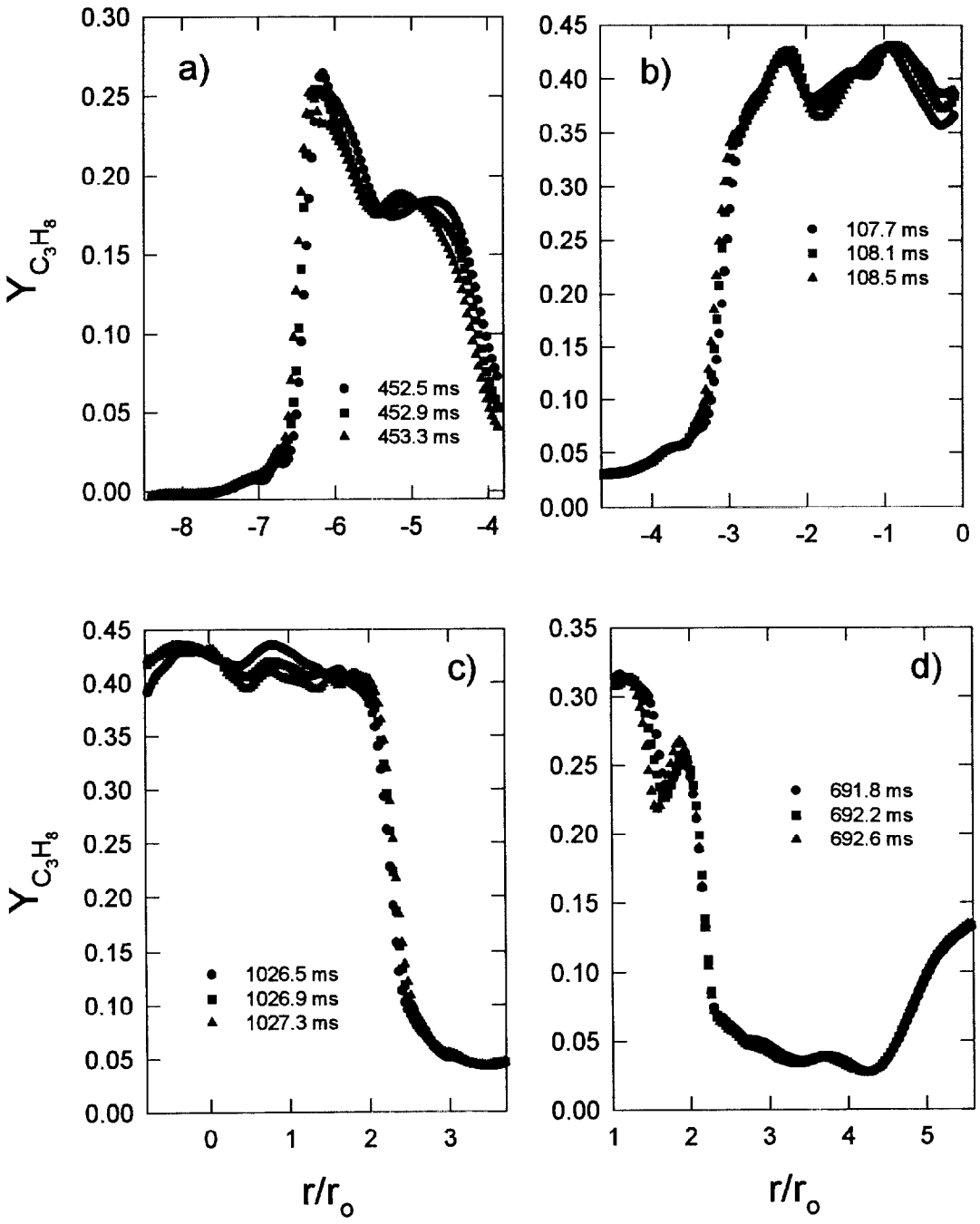

Figure 21. Three consecutive radial profiles of propane mass fraction are shown for times when the largest value of χ_r is observed for a given data set. The plots are for measurements shown as $\log(\chi_r)$ in a) Fig. 13a, b) Fig. 13b, c) Fig. 12, and d) Fig. 13c.

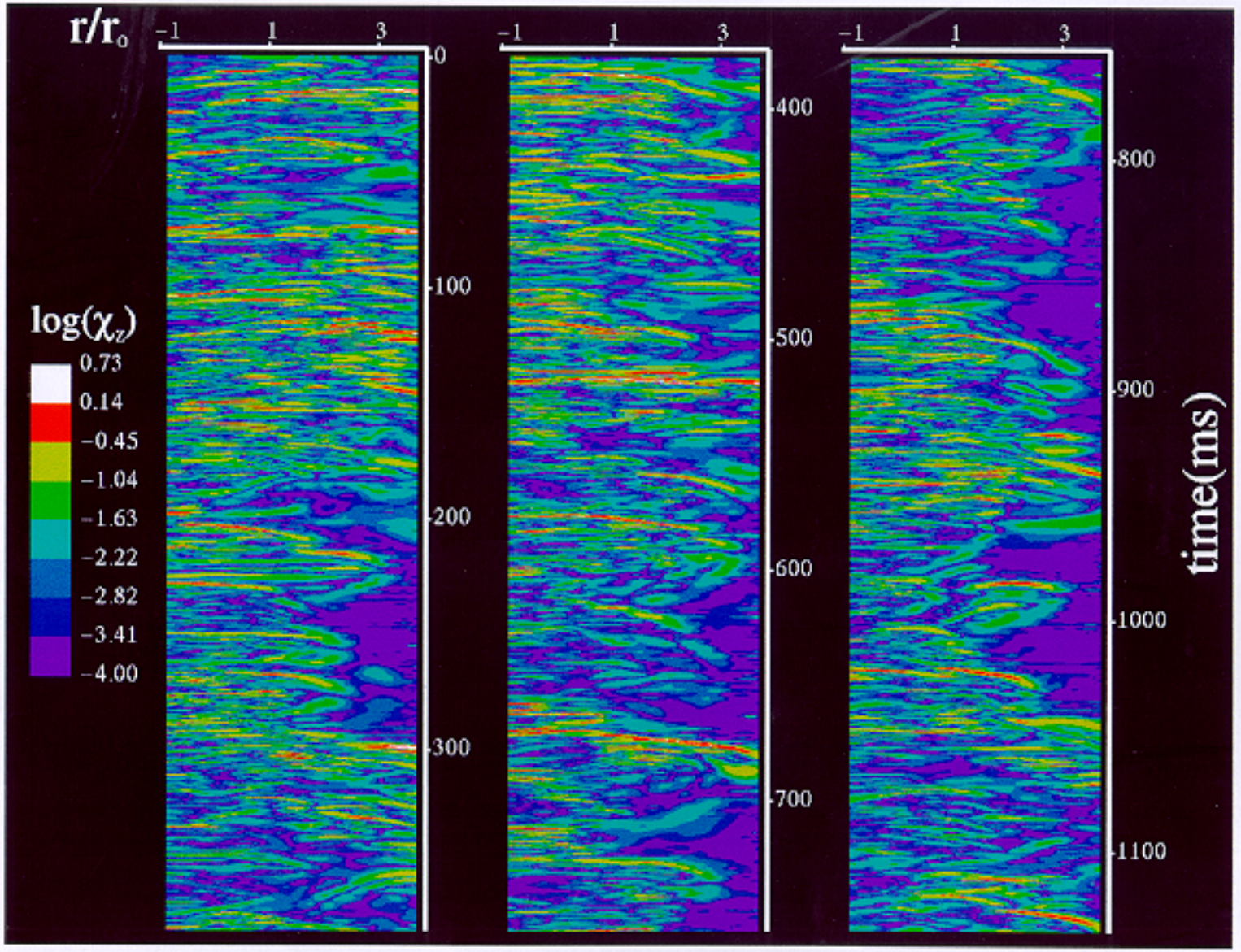

Figure 22. The time behavior of log(χ_z) (represented by an eight−level false−color scale) is shown for 128 adjacent points extending from $r/r_o = -0.89$ to 3.69. The axial location is $z/r_o = 40$.

smaller values during more quiescent times. Similarly, for the short periods when particularly large values of $\log(\chi_r)$ are observed over significant radial distances, high values of $\log(\chi_z)$ are also present. In most cases these narrow regions are more easily identified in the latter case due to the layering of the structures.

The stratified structure is evident in images of $\log(\chi_z)$ for the remaining four data sets shown in Fig. 23. Comparisons of the two images for positions nearest the centerline (Figs. 23b and c) with the corresponding images in Fig. 13 supports the above conclusions. At the jet's outer edge the regions of high scalar dissipation due to the formation of LSTSs lead to distinctly different appearances for $\log(\chi_z)$ (Figs. 23a and d) as compared to those for $\log(\chi_r)$ (Figs. 13a and d). High values of $\log(\chi_z)$ also appear at positions where the relatively straight portions of the fishhook-shaped regions of high $\log(\chi_r)$ are observed, but become very low in the regions where the fishhooks are sharply curved. The stirring motions within the LSTSs are less evident in Fig. 23 than they were for the corresponding radial-component images.

As was the case for images of the radial scalar dissipation component, relatively low noise levels are observed in the data for radial locations where only air should be present (see Fig. 23a and d). There is also noise evident in Fig. 23c for the mass fraction structure located on the right-hand edge of the image between roughly 160 ms to 200 ms where repeating bands can be seen. Similar bands are evident elsewhere in this image, as well as in the other images of $\log(\chi_z)$. It has been impossible to identify a particular frequency or spatial distribution for these bands. It is likely that they are due to a combination of systematic variations in the line camera output and artifacts resulting from the wavelet analysis.

Figure 24 shows the time behaviors over a 200 ms period for Y, χ_z, and $\log(\chi_z)$ along the centerline for the data shown in Figs. 7 and 22. The corresponding plot for χ_r is Fig. 15. While the time behaviors for both χ_z and χ_r consist of relatively low values punctuated by sharp increases, comparison of the two figures shows that the short periods of very large values are not highly correlated, and the two plots have very different appearances. The $\log(\chi_z)$ time behavior has very similar features to those observed for $\log(\chi_r)$, with high frequency variations and a most probable value centered between -2 and -3.

The pdf of $\log(\chi_z)$ based on time records for the eight radial locations nearest the jet centerline is shown in Fig. 25. Comparison with the corresponding pdf for $\log(\chi_r)$ in Fig. 17 shows that the two profiles are identical within the uncertainty of the measurements. Average and rms values for the data used to generate Fig. 25 are -2.363 and 1.085, respectively. These values are nearly identical to those, -2.329 and 1.076, calculated for the corresponding $\log(\chi_r)$ results. Within the uncertainty

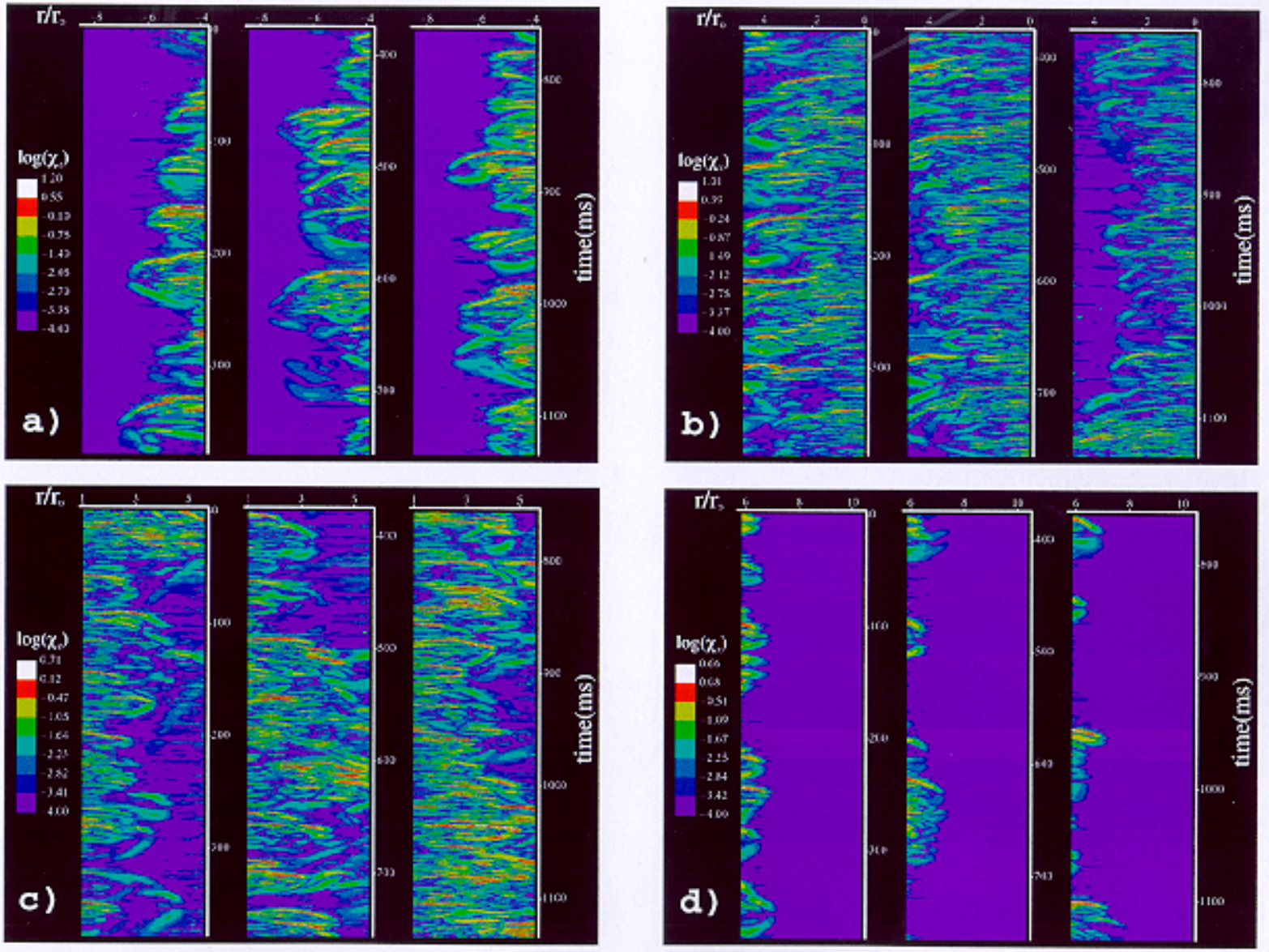

Figure 23. Time records of $\log(\chi_z)$ (represented by eight–level false–color scales) along lines positioned at four different radial locations across the jet flow are shown. The axial location is $z/r_o = 40$.

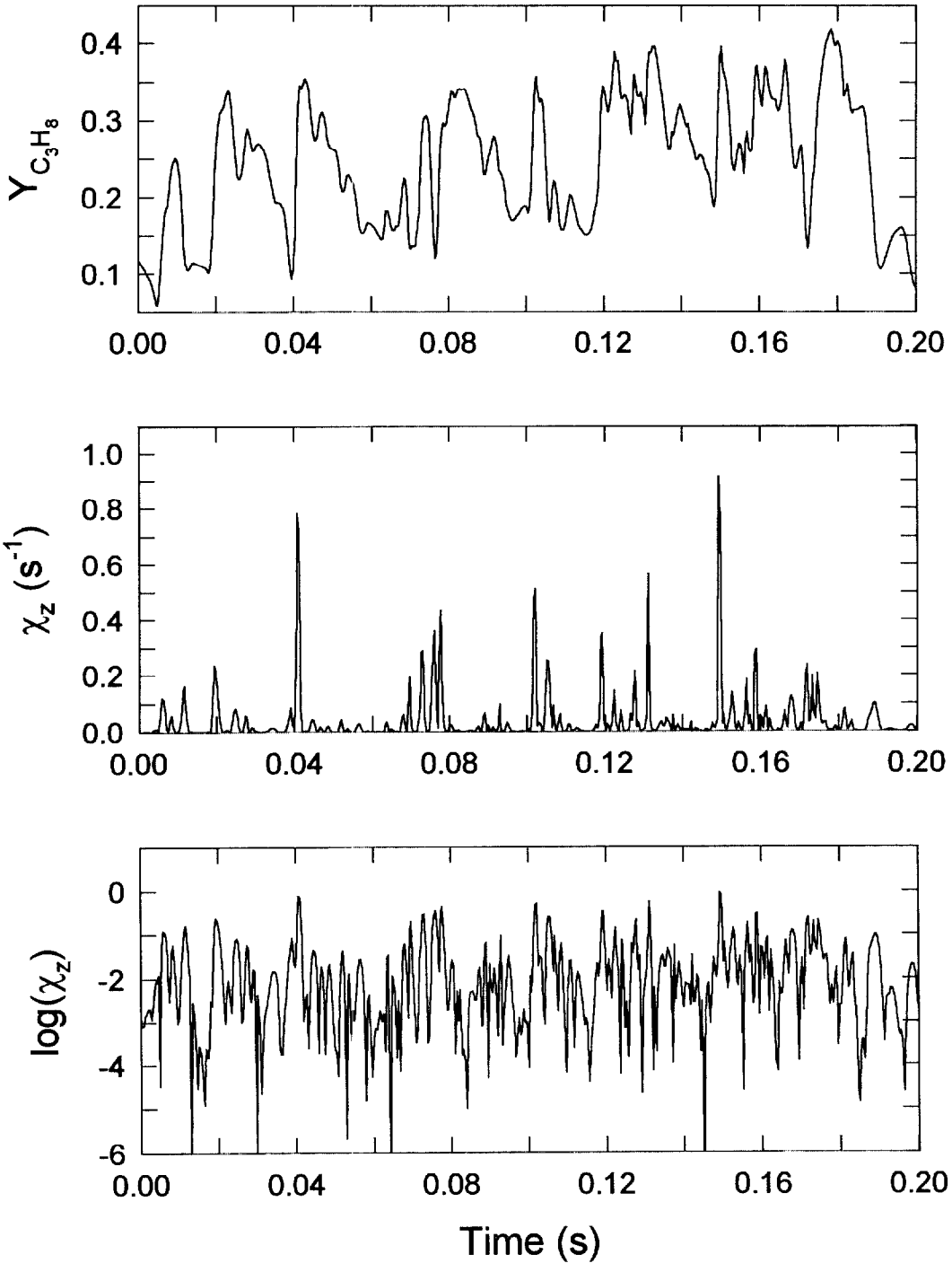

Figure 24. Centerline (r = 0) values of Y, χ_z, and log(χ_z) are plotted for the data shown in Figs. 7 and 22. Results for the first 200 ms of the time record are shown.

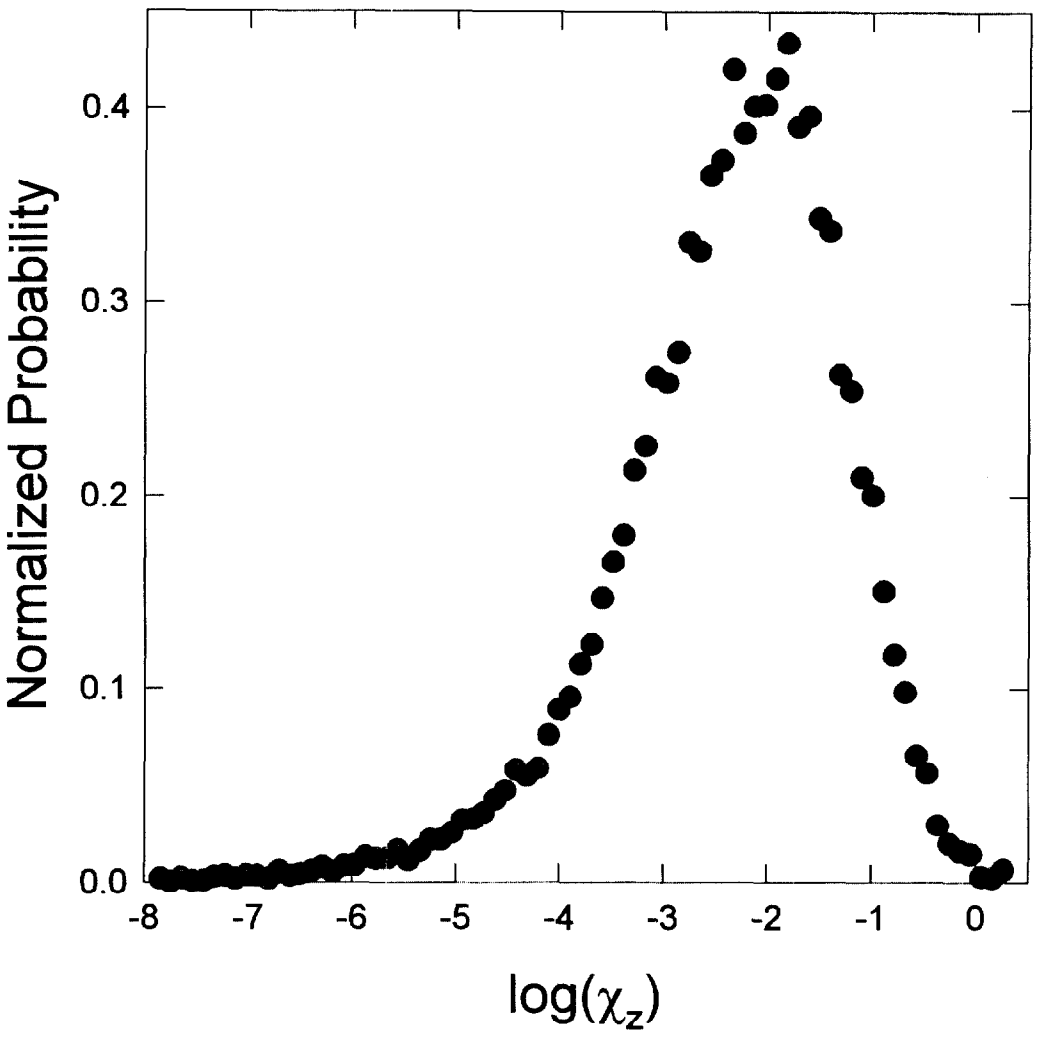

Figure 25. The pdf for $\log(\chi_z)$ is shown for 23,992 measurements recorded within $0.1r_o$ of the jet centerline in the propane jet.

introduced by the use of Taylor's hypothesis, it is evident that the scalar dissipation near the jet centerline is isotropic in the plane formed by the jet axis and radial direction. This conclusion is consistent with the success of the approach of Dahm and Buch[79] in predicting the form of $\log(\chi_{1D})$ based on χ_r measurements. Due to the similarity of the pdfs, the same log-normal χ distribution also reproduces the distribution of $\log(\chi_z)$ quite well.

Average and rms values for $\log(\chi_z)$ as a function of radial position are shown in Figs. 26 and 27, respectively. The three data sets closest to the centerline agree well and indicate that $\overline{\log(\chi_z)}$ values decrease as the measurement position moves away from the centerline. This should be contrasted with the results for $\overline{\log(\chi_r)}$ shown in Fig. 19 which increase for locations from $|r|/r_o = 0$ to ≈ 3, before

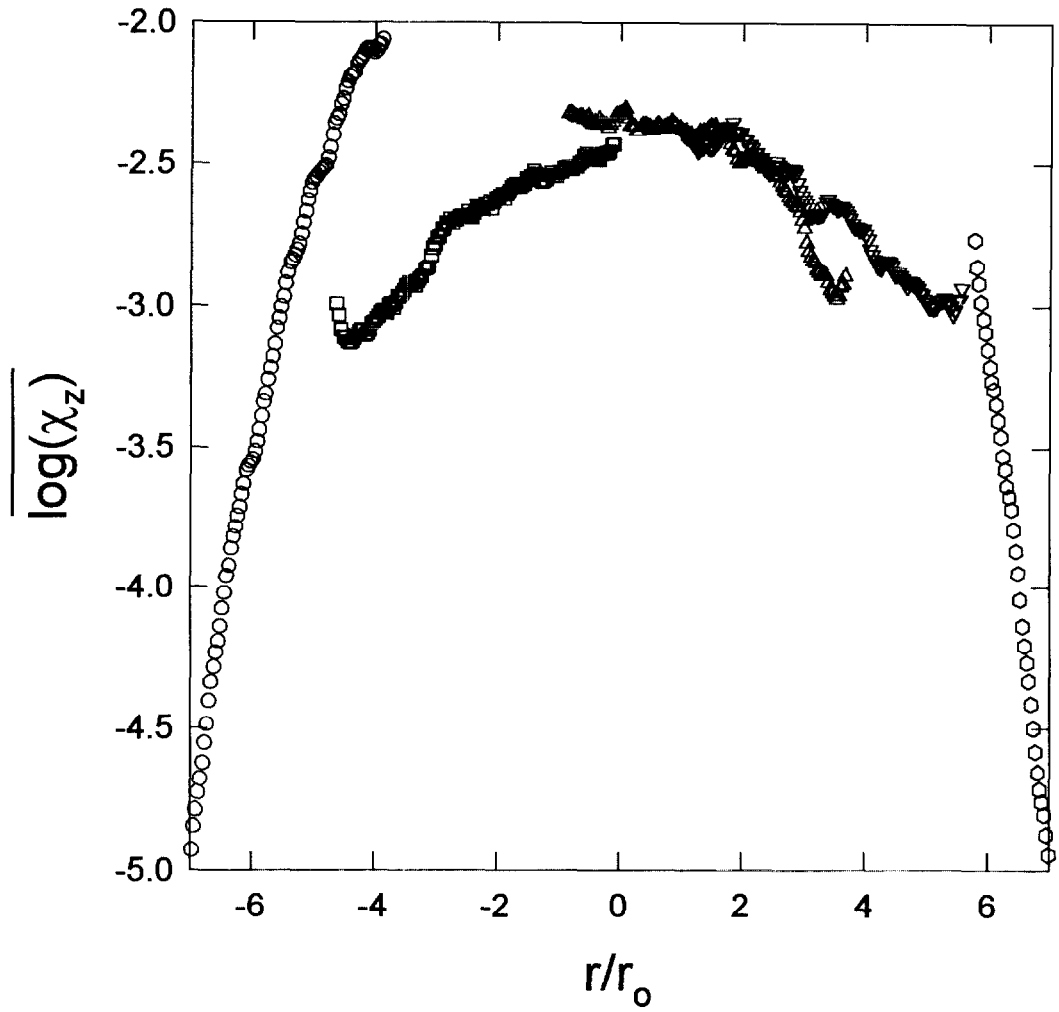

Figure 26. Average values of $\log(\chi_z)$ are plotted as a function of r/r_o for the five sets of data reproduced in Figs. 22 and 23.

beginning to fall off. The fall-off in $\overline{\log(\chi_z)}$ with r could be due to the use of Taylor's hypothesis since earlier studies have shown that values for χ_z are underestimated by amounts which increase with radial distance from the centerline.[123,124] Values of average $\overline{\log(\chi_z)}$ for the two remaining data sets do not agree as well. These data indicate very sharp drops in $\overline{\log(\chi_z)}$ for large radial distances. These decreases are not real, but are artifacts due to the combination of velocity radial profiles and the intermittency function used to calculate the time-averaged velocity profile necessary for the application of Taylor's hypothesis. It should be kept in mind that Taylor's hypothesis should be a very poor approximation near the jet edge in any case due to the presence of intermittent behavior and periods of reverse upstream flow.

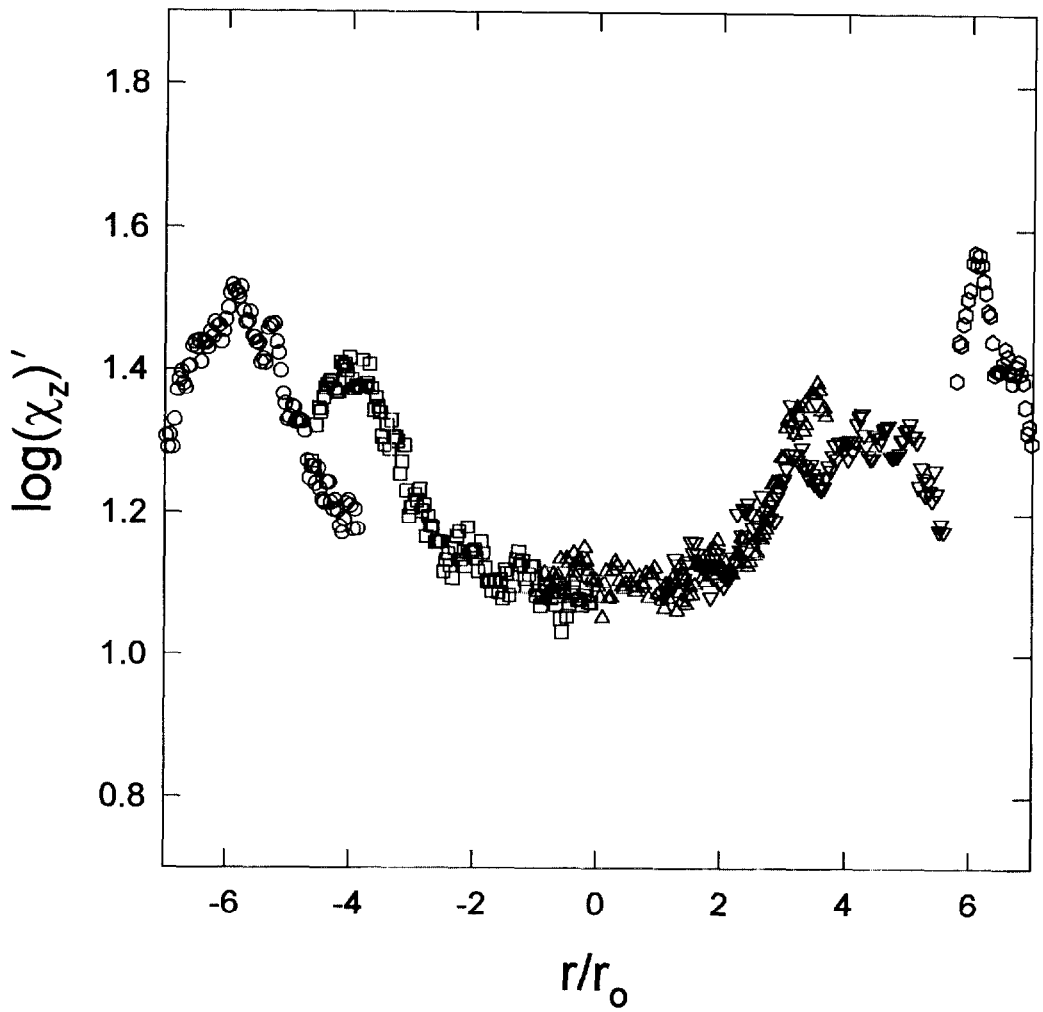

Figure 27. Root-mean-square values for $\log(\chi_z)$ are plotted as a function of r/r_o for the five sets of data reproduced in Figs. 22 and 23.

Interestingly, even though the results indicate that $\overline{\log(\chi_z)}$ and $\overline{\log(\chi_r)}$ have opposite dependencies on radial distance from the jet centerline for $|r|/r_o = 0$ to 3, values of the rms are roughly constant for the two components over the same locations. In the case of the χ_z results, the rms values begin to increase for $|r|/r_o > 3$, but it is impossible to conclude whether this behavior is real due to uncertainties due to the use of Taylor's hypothesis. The very large increases in the rms observed for $\log(\chi_r)$ near $r/r_o = \pm 6$ are not evident for the $\log(\chi_z)$ data.

As for the χ_r data, radial mass fraction profiles centered around the times when the maximum values of $\log(\chi_z)$ occur have been identified for the mass fraction data shown in Figs. 7 and 8a-c and are plotted in Fig. 28. The radial profiles corresponding to the times when the second highest values occur are shown in Fig. 29. As is to be expected, the largest values of $\log(\chi_z)$ are due to very rapid

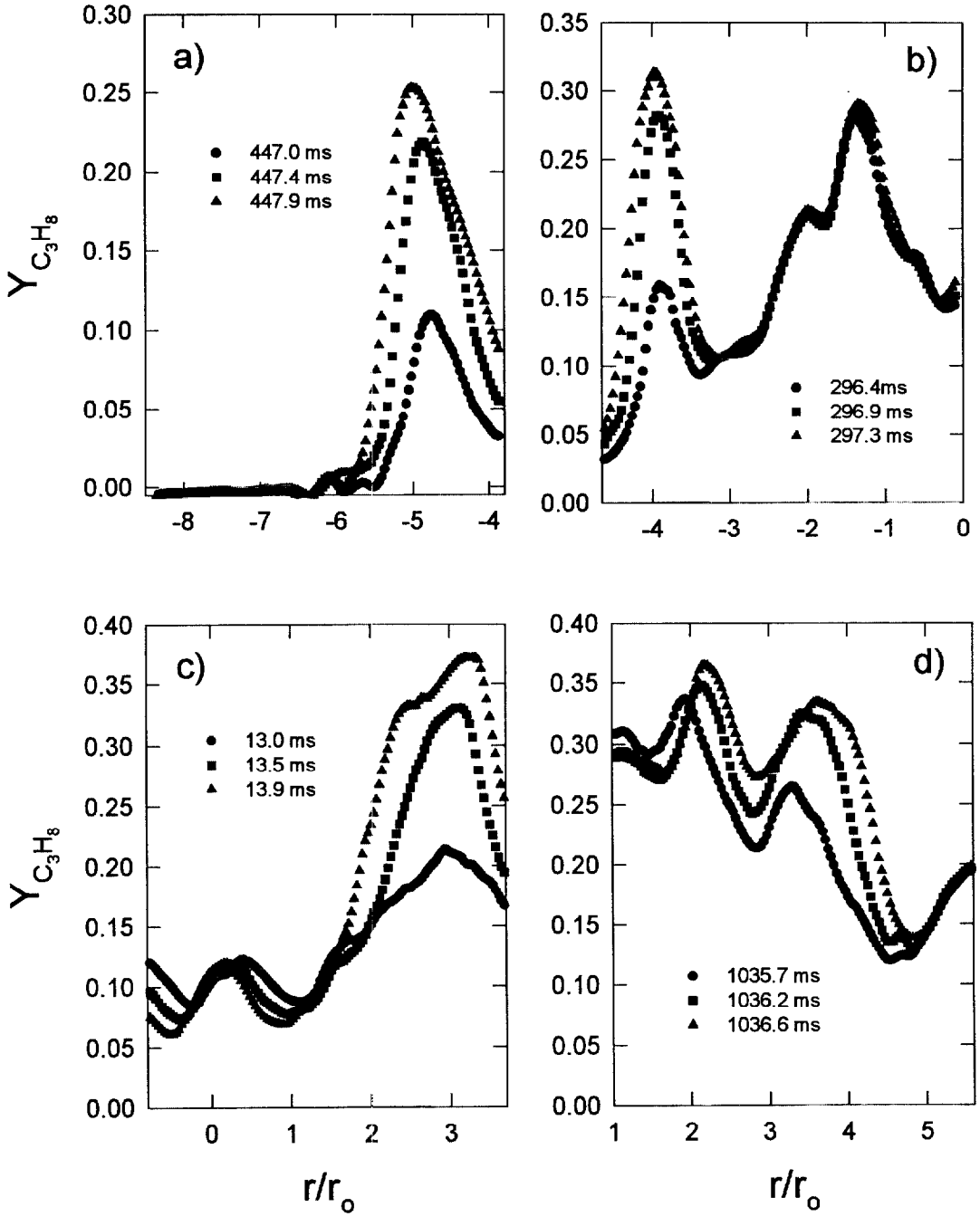

Figure 28. Three consecutive radial profiles of Y are shown for times when the largest values of χ_z are recorded for a given data set. The plots are for measurements shown as $\log(\chi_z)$ in a) Fig. 23a, b) Fig. 23b, c) Fig. 22, and d) Fig. 23c.

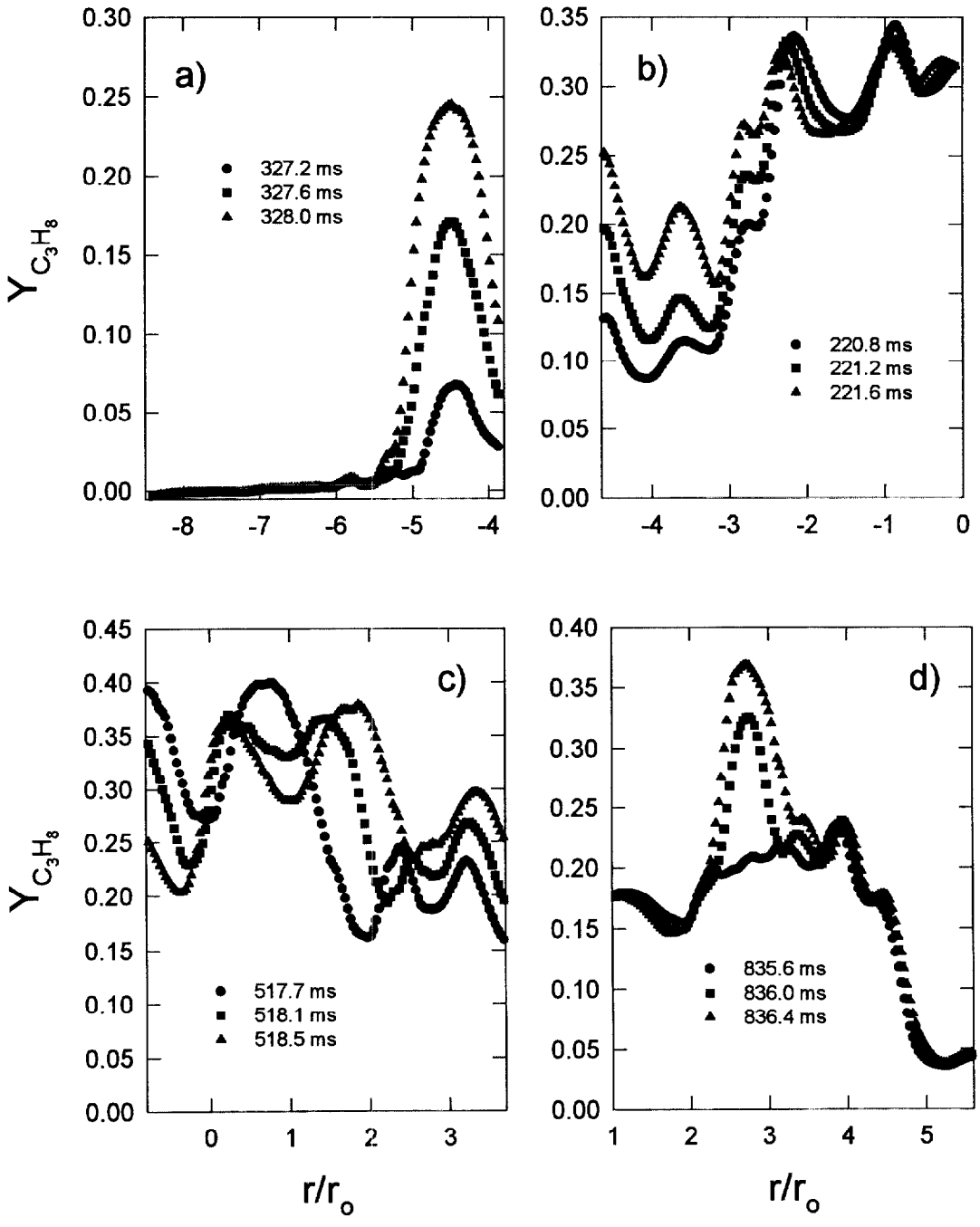

Figure 29. Three consecutive radial profiles of Y are shown for times when the second largest values of χ_z are recorded for a given data set. The plots are for measurements shown as $\log(\chi_z)$ in a) Fig. 23a, b) Fig. 23b, c) Fig. 22, and d) Fig. 23c.

increases in mass fraction with time. It is somewhat surprising, given the layered appearance of the images of $\log(\chi_z)$, that the sharp increases in concentration which result in the highest values of χ_z occur over fairly narrow radial widths of 1 to 2 r_o. This observation suggests that organized structures on the order of this size are responsible. In many of the radial profiles the mass fraction remains nearly constant with time for positions away from those where the sharp increases occur. This observation reinforces the conclusion that relatively small organized motions are responsible for the largest values of $\log(\chi_z)$ and also suggests that the localized events responsible for the high concentration time gradients have occurred recently. Otherwise, one would expect that the mass fraction gradients responsible would have been smoothed by turbulent mixing and molecular diffusion.

Values of χ_p have been calculated using Eq. (26). Space-time images of $\log(\chi_p)$ are shown in Figs. 30 and 31. These images have different appearances than those for $\log(\chi_r)$ and $\log(\chi_z)$ shown earlier, but many of the same characteristics present in the single-component images can be easily identified. The alternating regions of intense and relatively inactive periods of small-scale mixing noted previously are evident near the jet centerline. The correlation of the intense periods with the presence of higher values of $\log(\chi_p)$ is more evident than for the single-component images. A distinct elongation of relatively constant values of $\log(\chi_p)$ in the radial direction is present, but is not as prominent as in the $\log(\chi_z)$ images. The short periods of time during which regions of high scalar dissipation appear to extend across the entire displayed area for the images of $\log(\chi_r)$ and $\log(\chi_z)$ (Figs. 12 and 22) are more easily identified in Fig. 30. In the planar image these areas appear to be more continuous with fewer breaks than for the single-component results. This suggests that the breaks are not true discontinuities in high values of scalar dissipation, but are due to distortions of a continuous interface which lies between two relatively large volumes of jet fluid having significantly different concentrations.

There is a great deal of organization apparent in the $\log(\chi_p)$ plots for positions located well off the jet centerline. Narrow bands of roughly constant $\log(\chi_p)$ are apparent which extend over substantial fractions of the images. For positions nearer the jet center these layers tend to be aligned principally in the radial direction at similar angles, roughly 100° to 110° to the z axis, as observed for the $\log(\chi_r)$ plots (Figs. 12 and 13). Near the jet outer edge the layers develop the same fishhook shape described for the $\log(\chi_r)$ images (Figs. 12 and 13). For locations near the jet outer edge (Figs. 31a, d) the stirring behavior discussed earlier is even more evident than in the $\log(\chi_r)$ images. A clear example is at roughly 540 ms in Fig. 31a where regions of high $\log(\chi_p)$ can be seen curving upstream and downstream from the central region of a LSTS.

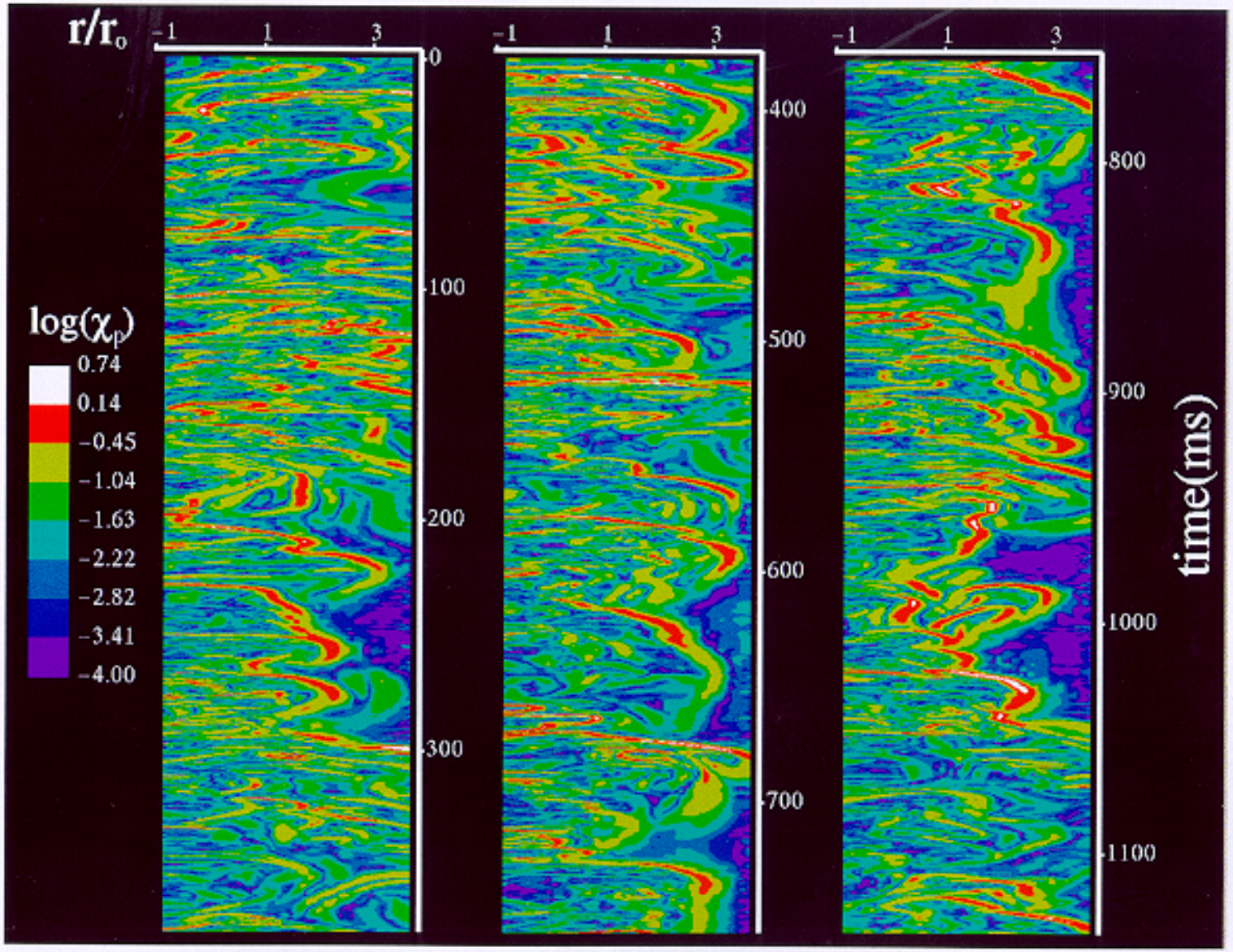

Figure 30. The time behavior of $\log(\chi_p)$ (represented by an eight–level false–color scale) is shown for 128 adjacent points extending from $r/r_o = -0.89$ to 3.69. The axial location is $z/r_o = 40$.

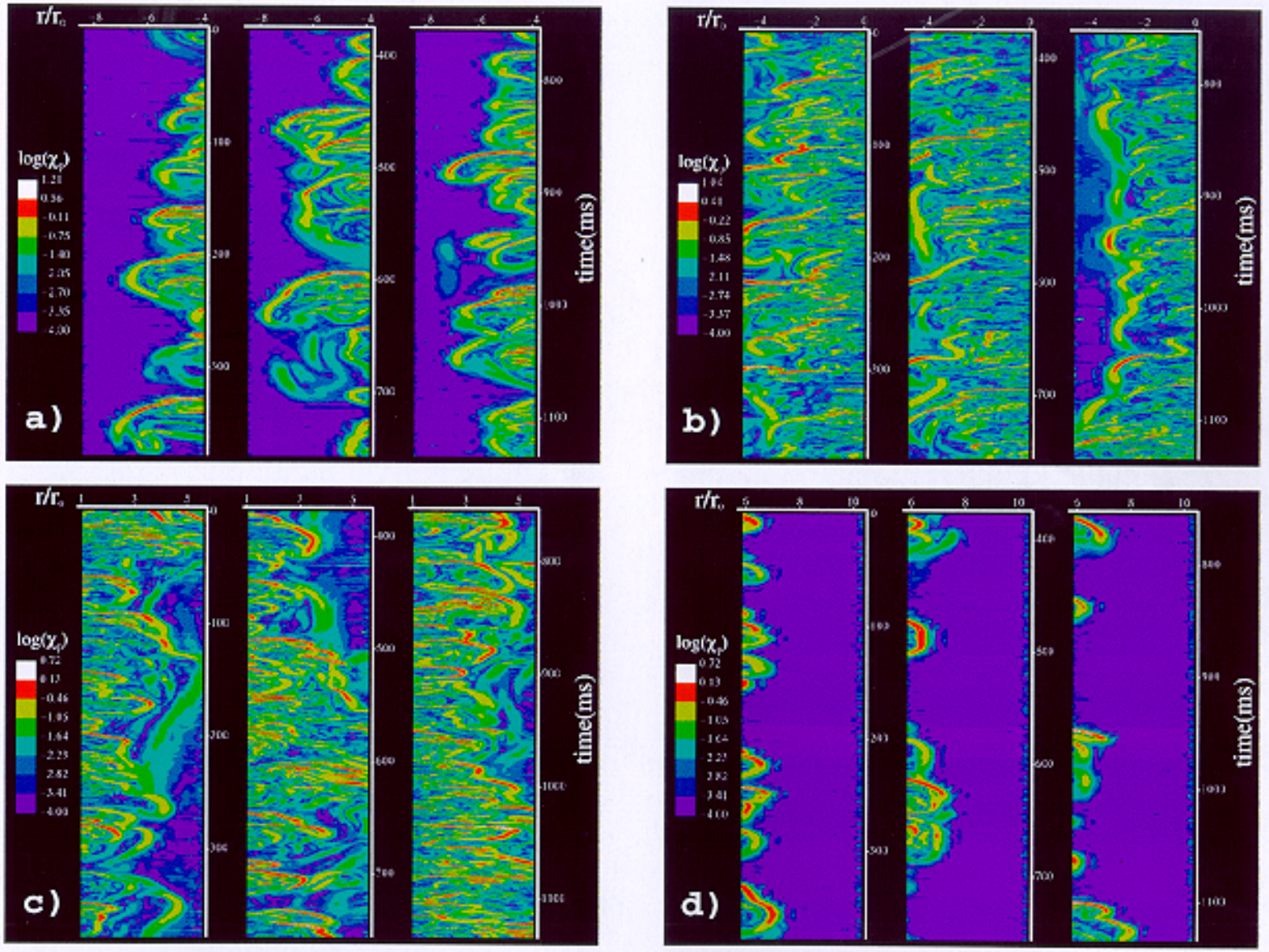

Figure 31. Time records of $\log(\chi_p)$ (represented by eight–level false–color scales) along lines positioned at four different radial locations across the jet flow are shown. The axial location is $z/r_o = 40$.

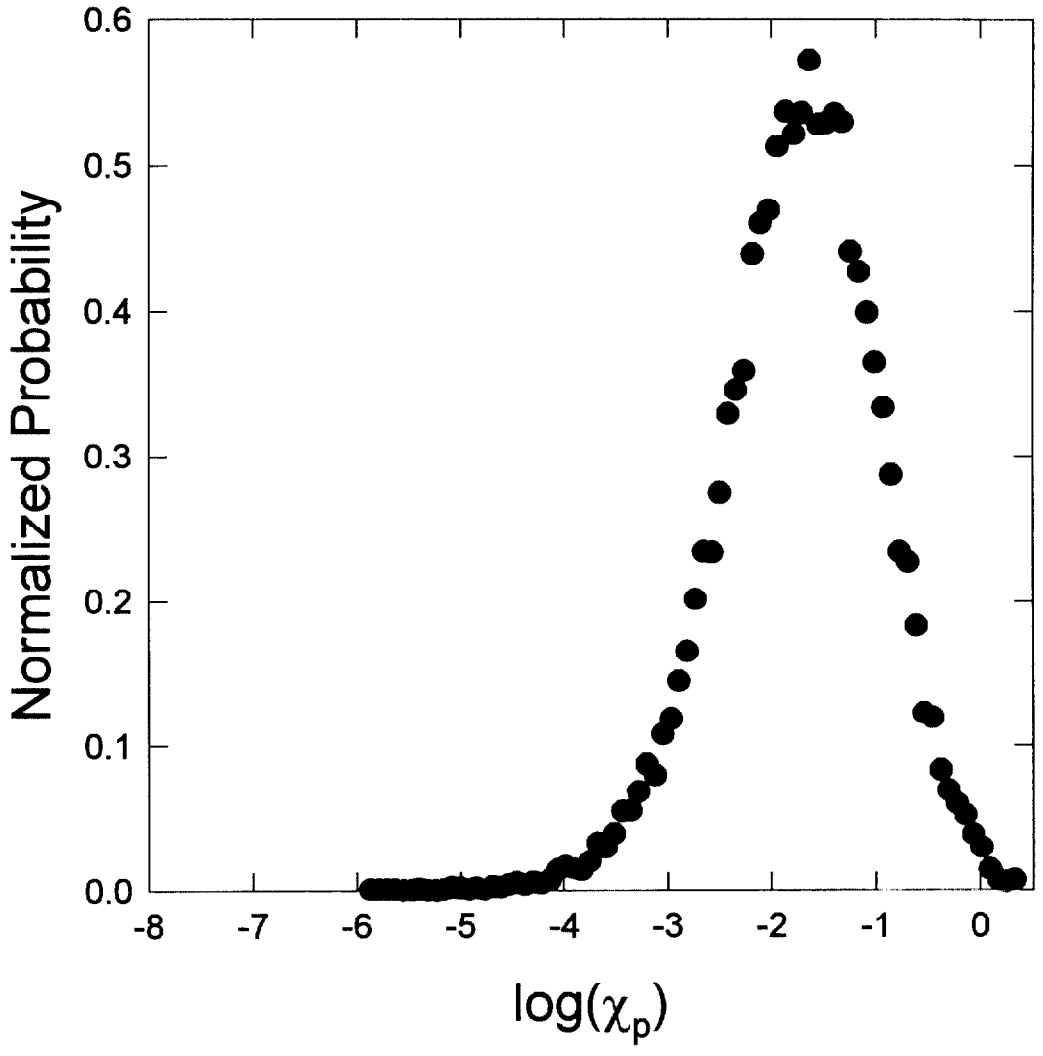

Figure 32. The pdf for $\log(\chi_p)$ is shown for 23,992 measurements recorded within $0.1r_o$ of the jet centerline in the propane jet.

The pdf of $\log(\chi_p)$ for the eight radial locations nearest the jet centerline in Figs. 30 and 31b is shown in Fig. 32. Comparison with the corresponding plots for the radial and axial components (Figs. 17 and 25) shows that the $\log(\chi_p)$ pdf is much more symmetric and that the long tail on the low-value side does not extend nearly as far as for the single-component pdfs. Average and rms $\log(\chi_p)$ values for the pdf are -1.738 and 0.750, respectively. Buch and Dahm have described a mathematical procedure, derived in a similar way to the approach used above to treat measurements of a single component of χ,[79] to calculate the pdf for χ from measurements of two components.[47] Assuming the pdf for χ is isotropic allows the following probability distribution for the projection of a given χ value into a plane, χ_{2D},

$$\beta(\chi_{2D},\chi) = 0.5\left| 1-\frac{\chi_{2D}}{\chi} \right| , \tag{33}$$

to be derived. Buch and Dahm provide an algorithm for generating the pdf for χ from the pdf for χ_{2D}.[47] As for the one-dimensional case previously discussed, it was decided to use the reverse transformation in which an assumed log-normal distribution for χ is used to deduce the expected pdf for χ_{2D}. For this purpose, the log-normal χ pdf determined previously from the pdf for $\log(\chi_r)$ was used as input for the calculation and Eq. (33) was integrated numerically to give the cumulative χ_{2D} pdf.

Figure 33 compares the calculated $\log(\chi_{2D})$ pdf with the experimental pdf for centerline values of $\log(\chi_p)$. Also shown is the assumed log-normal pdf for χ used as input for the calculation. The agreement between $\log(\chi_p)$ and $\log(\chi_{2D})$ is excellent as confirmed by comparing the average and rms values for $\log(\chi_p)$ (-1.738, 0.750) with those for the calculated $\log(\chi_{2D})$ pdf (-1.738, 0.785). Since the inputs for the calculation were taken from the assumed log-normal distribution of χ derived from measurements of the single-component χ_r, this close agreement provides strong support for the validity of the analysis suggested by Dahm and Buch[47,79] for projecting pdfs for χ into one and two dimensions. Furthermore, these results demonstrate that the experimental measurements agree quite well with the predicted behavior and provide strong evidence that the experimental data are accurately capturing the behavior for the two single components of χ. Note also that the success of the two calculational approaches also requires that the centerline distribution of χ values be very nearly log-normal and isotropic.

It was noted earlier that measurements of single- or two-dimensional components of χ are often used to estimate average values for χ. Two of the most common approximations can be written as

$$\overline{\chi} \approx 3\overline{\chi}_{1D} \tag{34}$$

and

$$\overline{\chi} \approx 1.5\overline{\chi}_{2D} . \tag{35}$$

Table 3 summarizes the average and rms log values determined from the experimental measurements of χ_r, χ_z, and χ_p along with the corresponding estimates for one and two-dimensional components of χ based on the assumed log-normal distribution and estimates for χ obtained using Eqs. (34) and (35). It is clear that estimates for χ based on experimental determinations of the distribution for a single component greatly underestimate the average and overestimate the rms for the true distribution of

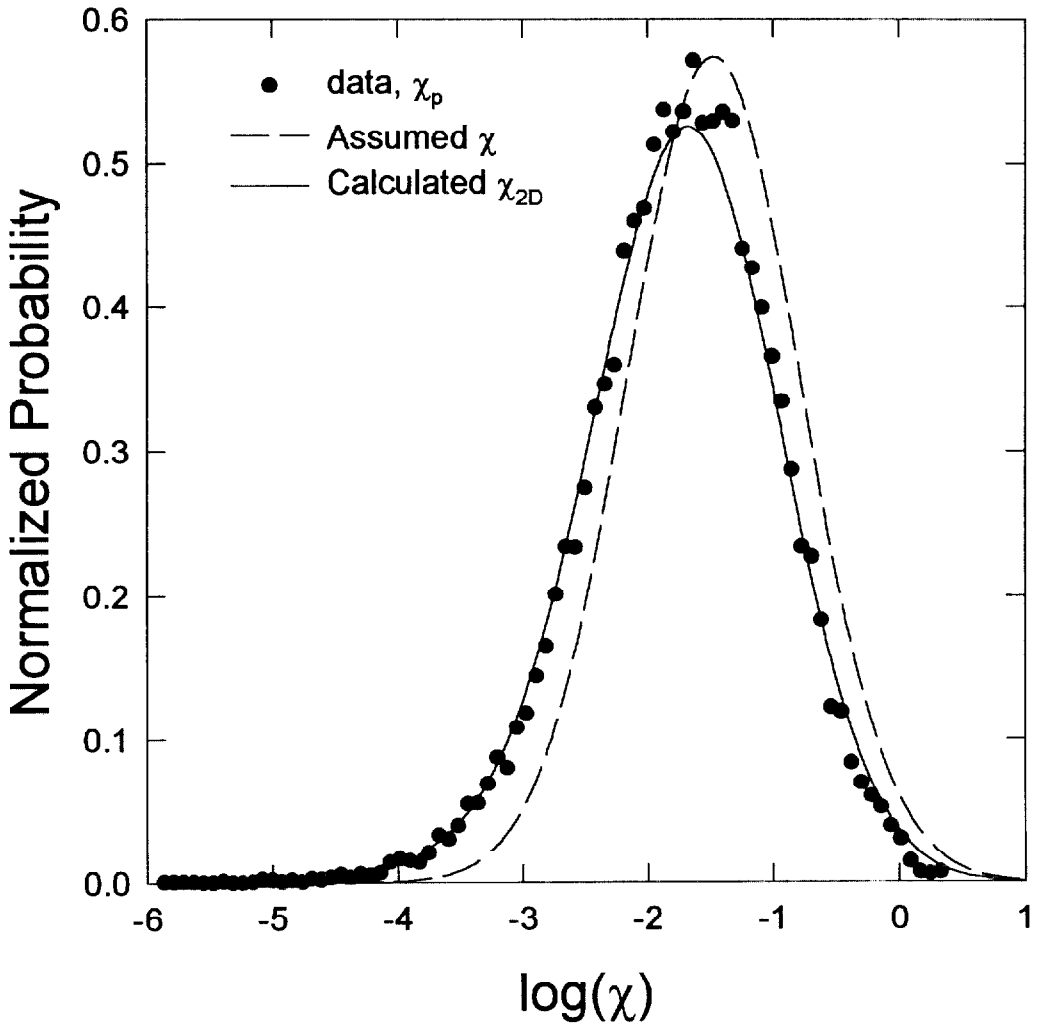

Figure 33. The experimental pdf (symbols) for $\log(\chi_p)$ is compared with the pdf for $\log(\chi_{2D})$ (solid line) calculated from an assumed log-normal distribution for χ (dashed line) having average and rms values of -1.472 and 0.694, respectively.

scalar dissipation. Estimates based on two-dimensional measurements also underestimate the average and overestimate the rms for the actual distribution, but the magnitudes of the errors are greatly reduced.

Average and rms values of $\log(\chi_p)$ as a function of radial position are shown in Figs. 34 and 35. Average values show some variation but appear to have a roughly constant value of $\log(\chi_p) \approx 1.75$ for $r/r_o = -4$ to 4. At larger distances from the centerline the average values begin to drop. The rms values seem to increase very slowly over the same radial positions (recall that the sharp increases at the

Table 3. Average and rms log values for various centerline scalar dissipation measures discussed in the text.

Property	Average	rms
$\log(\chi_r)$	-2.329	1.076
$\log(\chi_z)$	-2.363	1.085
$\log(\chi_p)$	-1.738	0.750
$\log(\chi_{1D})$	-2.329	1.076
$\log(\chi_{2D})$	-1.738	0.785
$\log(\chi)$	-1.472	0.694
$\log(3\chi_{1D})$	-1.852	1.076
$\log(1.5\chi_{2D})$	-1.562	0.785
χ_r	0.033	0.089
χ_z	0.031	0.091
χ_p	0.064	0.140
χ_{1D}	0.041	0.19
χ_{2D}	0.081	0.31
χ	0.121	0.42
$3\chi_r$	0.099	0.27
$3\chi_z$	0.093	0.27
$1.5\chi_p$	0.096	0.21
$3\chi_{1D}$	0.122	0.57
$1.5\chi_{2D}$	0.123	0.46

edges of the images are due to edge effects). As for the $\log(\chi_r)$ results, a sharp increase in rms is observed near $r/r_o = \pm 6$. The ten time records for data centered on $r/r_o = \pm 6.0$ in Figs. 31a and d have been used to generate the pdf for $\log(\chi_p)$ shown in Fig. 36. The pdf is clearly bimodal with one peak centered near $\log(\chi_p) = -4$ and a second at roughly -1.3. The images of $\log(\chi_p)$ suggest that the more negative peak is associated with noise in regions of the flow where only air is present. The high rms values observed at these radial locations are due to the bimodal nature of the pdf.

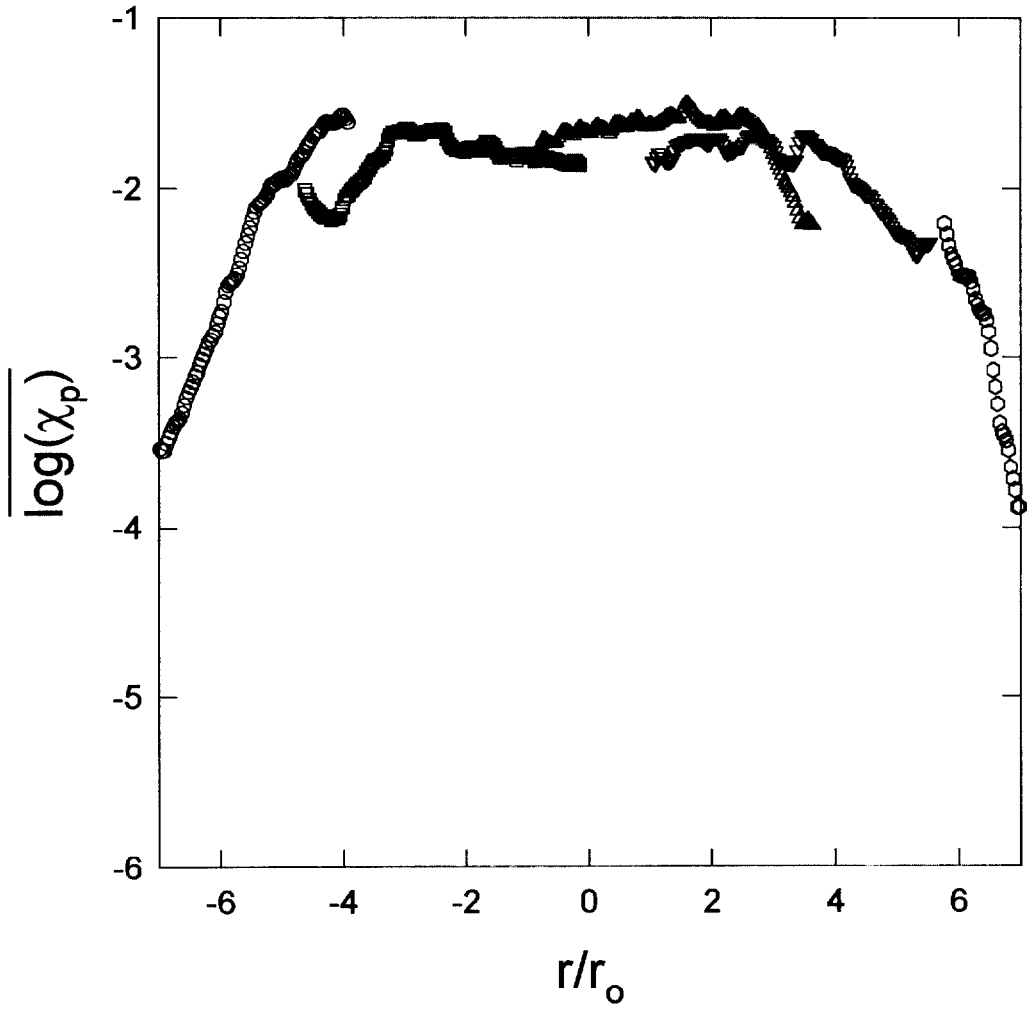

Figure 34. Average values of $\log(\chi_p)$ are plotted as a function of r/r_o for the five sets of data reproduced in Figs. 30 and 31.

Angles for the mass fraction concentration gradients, Θ, were calculated as described in Section II. The data are displayed as r-t images using an eight-level false-color scale to represent angle. A color-wheel legend on the images shows the correspondence between colors and orientation. The data were found to be very noisy in regions where the propane mass fraction approaches zero. For this reason, pixels corresponding to propane mass fractions below 0.01 are omitted from the images and appear as black regions.

Figure 37 shows the results of Θ measurements for the mass fraction data displayed in Fig. 7, which includes the jet centerline. Near the centerline Θ varies rapidly in time and space. These variations appear to be quite random even though relatively short periods of roughly constant Θ show a

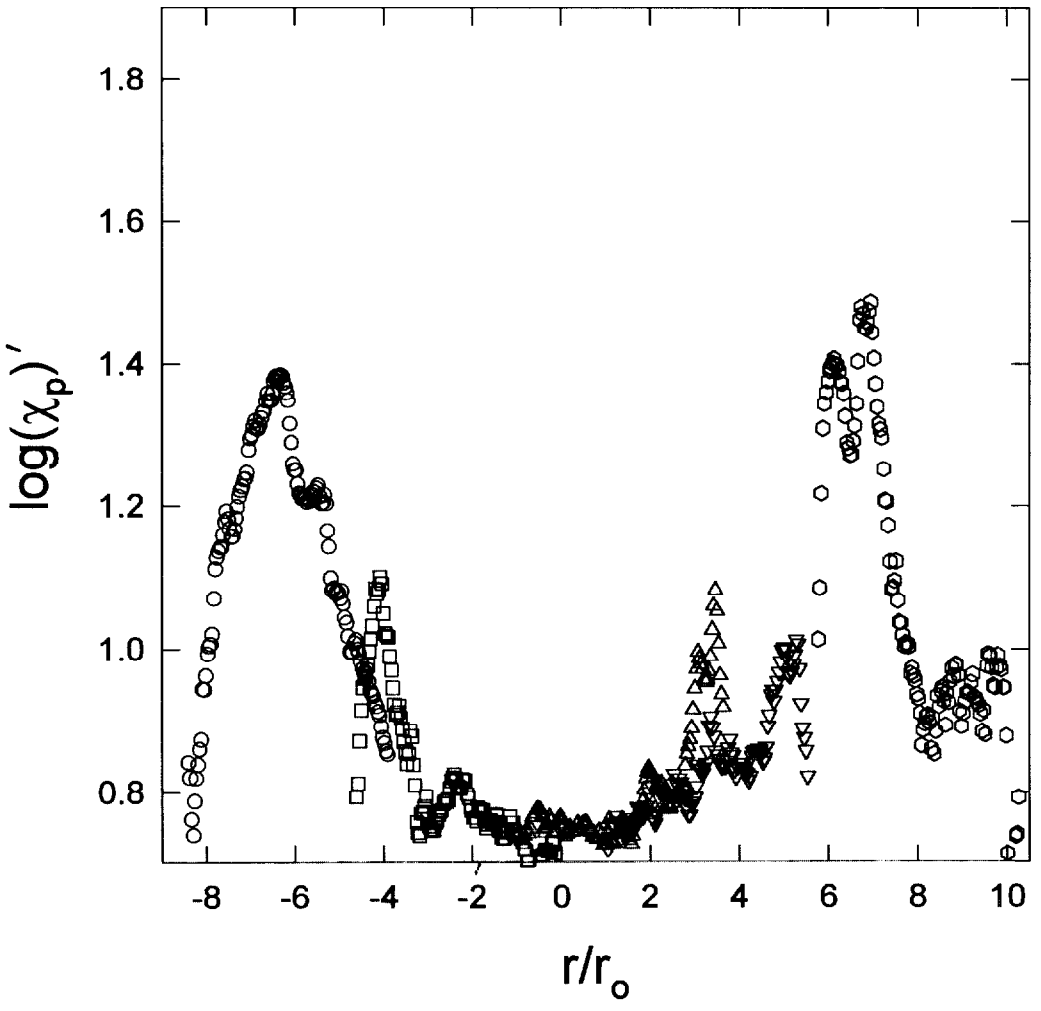

Figure 35. Root-mean-square values for $\log(\chi_p)$ are plotted as a function of r/r_o for the five sets of data reproduced in Figs. 30 and 31.

distinct elongation in the radial direction. As noted previously with regard to the behaviors of the one- and two-dimensional components of scalar dissipation, distinct periods are evident during which intense Θ fluctuations occur over short distances and times, while at other times the fluctuations are much less vigorous.

Greater organization of the flow field is evident in Fig. 37 along the right-hand edge of the image where extensive regions of red and yellow are observed for $|r|/r_o > 2$. These colors indicate mass-fraction gradients which are aligned primarily along the radial direction and point inward towards the jet centerline. The yellow regions generally extend to greater radial distances with increasing time and indicate gradients oriented slightly upstream, while the red regions tend to move towards the jet

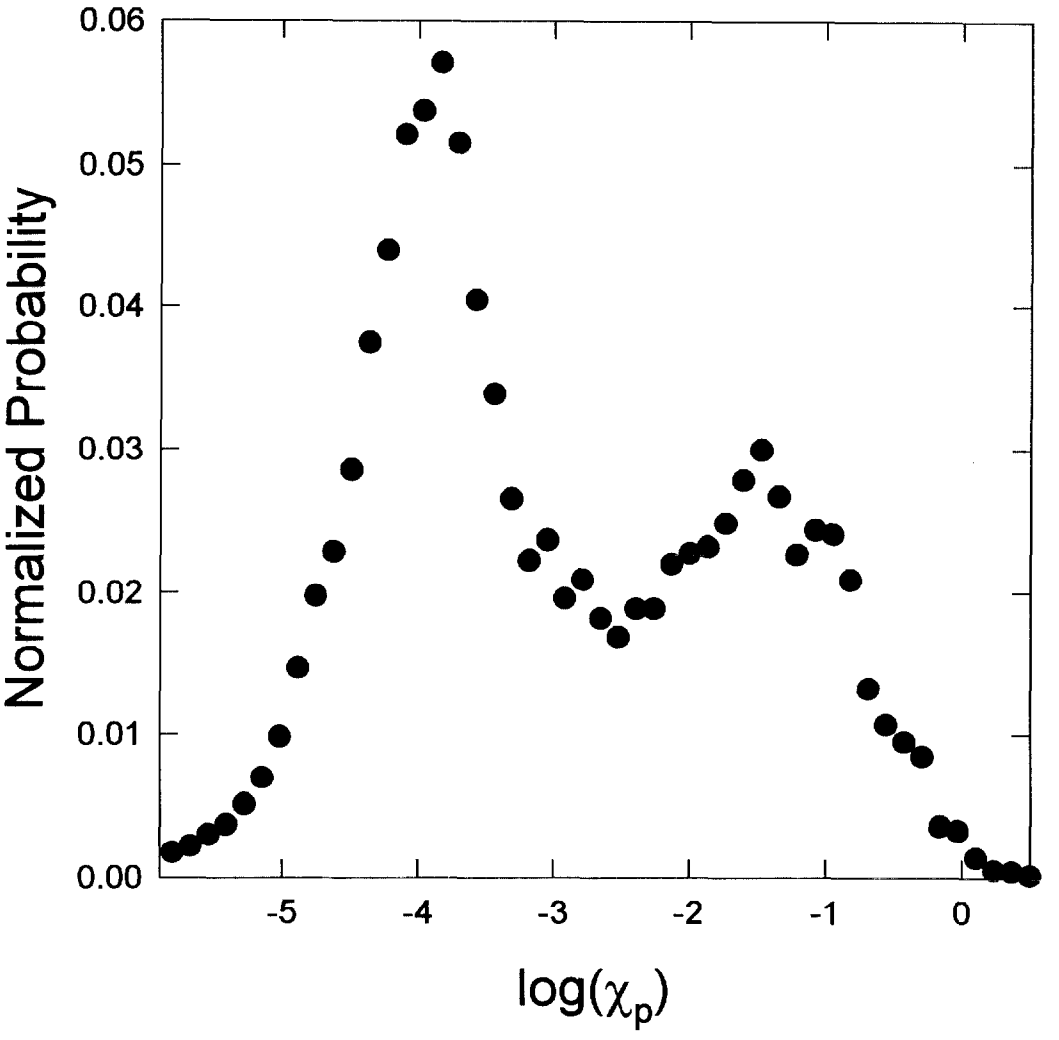

Figure 36. The pdf for $\log(\chi_p)$ is shown for 29,990 measurements recorded within $0.1r_o$ of $r/r_o = \pm 6$.

centerline with gradients pointing slightly downstream. These systematic variations in Θ show that these regions are associated with the LSTSs discussed earlier in which the concentration falls off rapidly in the radial direction and which have the fishhook shape identified earlier in the scalar dissipation measurements.

Figure 38 shows pdfs of Θ for three radial positions ($r/r_o = 0, \pm 0.12$) located near the jet centerline. At each location data for two adjacent pixels have been used. Note that a constant probability of $1/(2\pi) = 0.159$ corresponds to Θ oriented isotropically in the plane. The data are noisy, but several distinct trends are evident which suggest that the gradients of mass fractions are not isotropically oriented in the plane and that large-scale organization of the flow is responsible. Recall that Θ is defined such that 0 radians lies along the axial downstream direction, and the angle increases

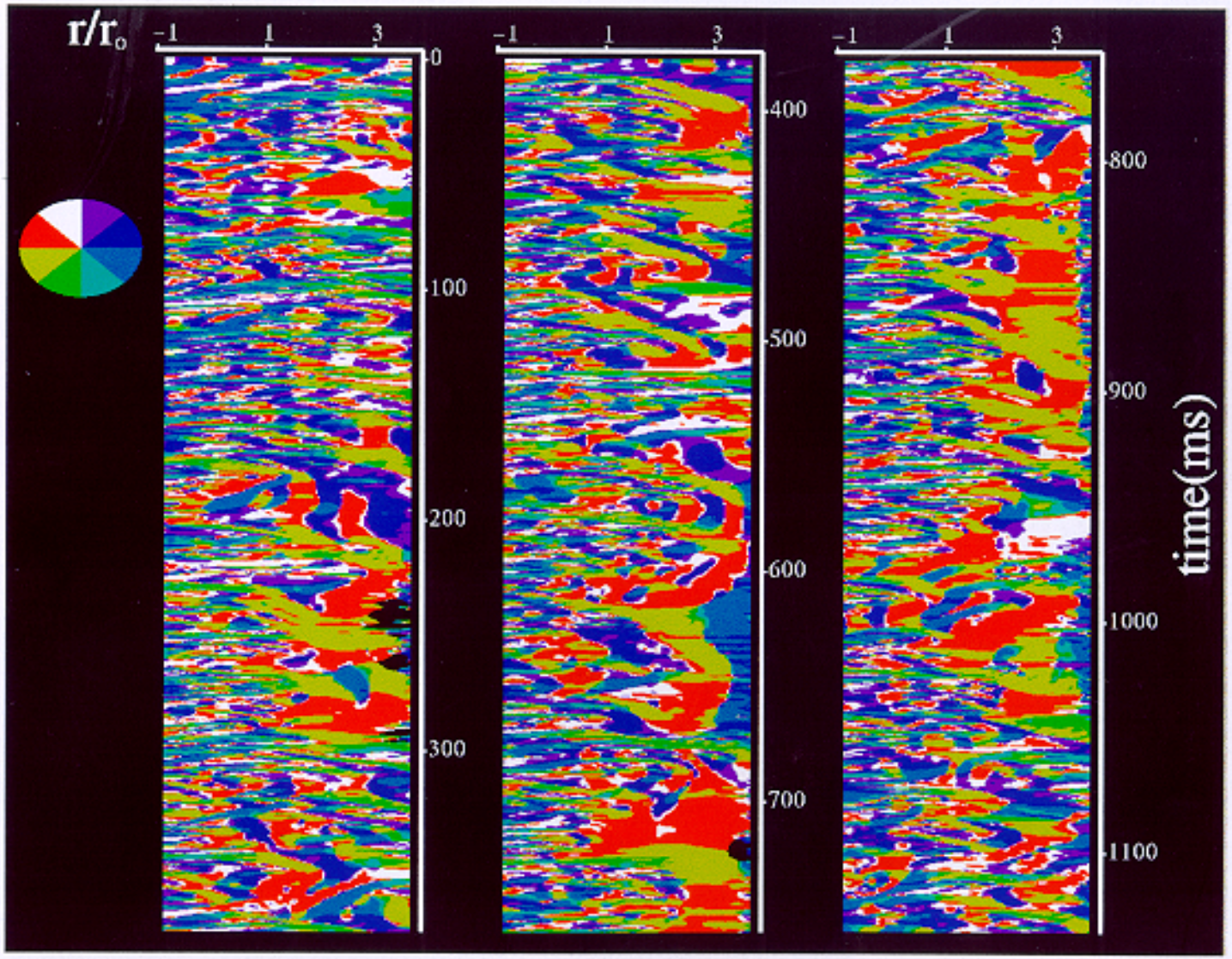

Figure 37. Values of Θ for 128 pixels in the $r-z$ plane of the propane jet are plotted as a function of time for the Y data shown in Fig. 7. The color wheel on the left–hand side shows the eight–level color coding used to represent angle. The upward direction on the wheel corresponds to the downstream direction of the flow (i.e., a concentration gradient aligned along the jet axis). Black regions designate locations where the mass fraction is less than 0.01.

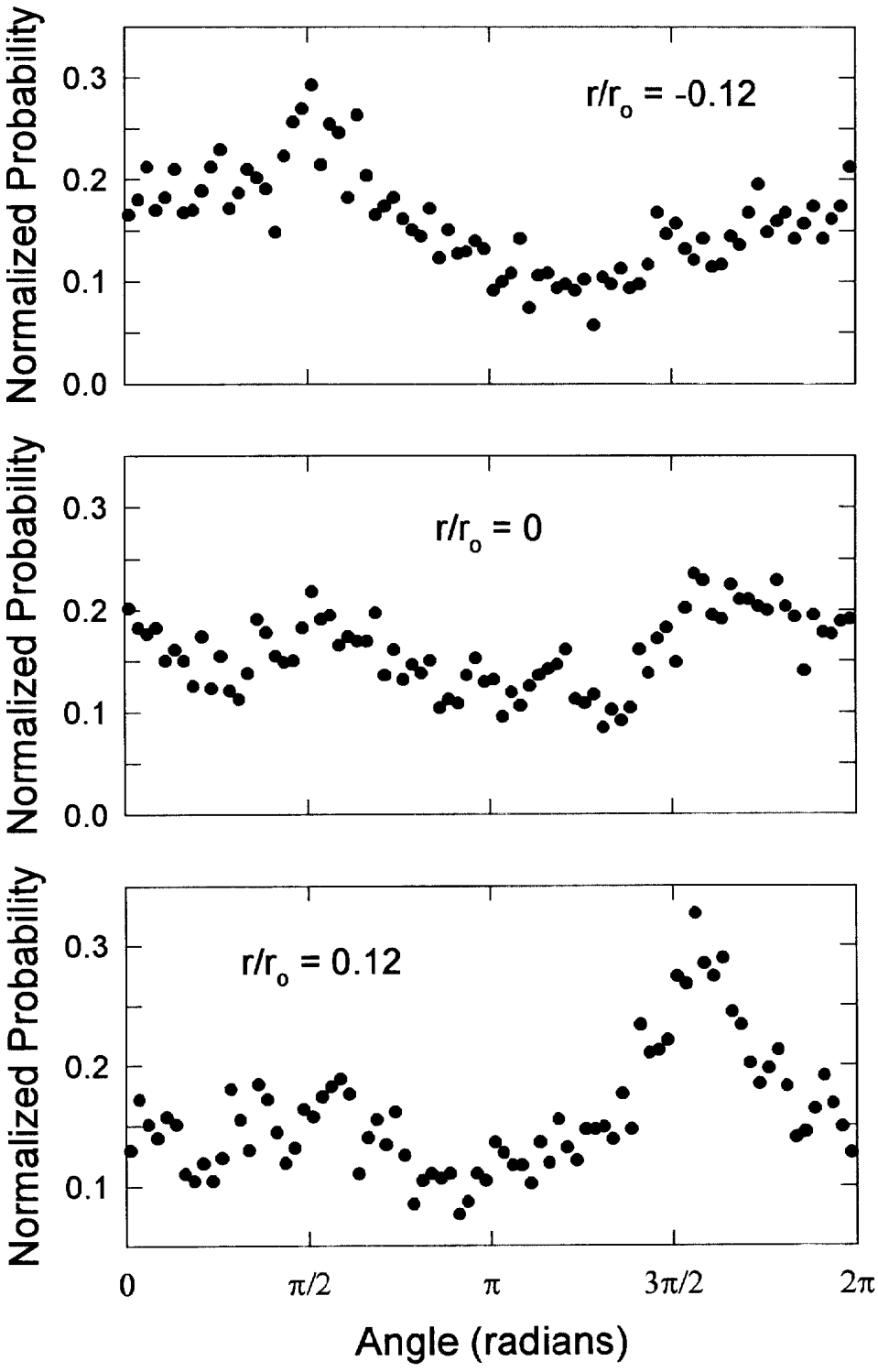

Figure 38. Three pdfs for Θ are shown for the indicated radial positions located $40r_o$ downstream of the jet exit. Each pdf is formed from 5,998 measurements recorded for two adjacent pixels.

from 0 to 2π in the clockwise direction. At the jet centerline small, but distinct and reproducible, variations in the probability with angle are found. The maximum values are observed for $\Theta = \pi/2$ and $3\pi/2$. These correspond to gradients lying along radial directions. Interestingly, the probability for gradients to lie primarily along the downstream direction ($\Theta = 0$ radians) is roughly two times greater than for the gradients to point upstream ($\Theta = \pi$ radians). Note that time-averaged mass fraction decreases with downstream distance, i.e., in the opposite direction of the more likely Θ. This requires that gradients oriented primarily in the upstream direction must, on average, have greater magnitudes than those oriented downstream, which is consistent with the presence of internal ramp-like structures on the jet centerline.

Comparison of the three pdfs in Fig. 38 shows that while the pdf on the jet centerline is symmetric with regard to radial direction, a distinct asymmetry develops as the measurement position is moved slightly off the centerline in either radial direction. This asymmetry results in a higher probability for angles near $\pi/2$ as compared to $3\pi/2$ for $r/r_o = -0.12$, while the opposite behavior is found for $r/r_o = 0.12$. These findings show that there is a higher probability for the concentration to fall off in the radial direction for these positions near the jet centerline. This higher probability is consistent with the decrease of $\bar{Y}$ with radial distance.

Figure 39 shows an image of Θ recorded at one of the outer edges of the propane jet corresponding to the mass fraction data shown in Fig. 8a. A systematic variation Θ is evident as one moves around the edges of individual structures. Generally, for these locations the gradients point toward the centerline, and with the passage of a structure the angles tend to decrease systematically from π (pointing predominantly upstream) to $\pi/2$ (pointing predominantly towards the centerline) to 0 radians (pointing predominantly downstream). For some of the structures the curvature of the outer edges extends over a large enough distance that the gradients nearer the centerline actually point away from the jet centerline, i.e., $\pi < \Theta < 5/4\ \pi$ (represented by green) and $7/4\pi < \Theta < 2\pi$ (represented by white).

For the locations along the outer edges of LSTSs there is little evidence of turbulent mixing. However, the variations of Θ within these structures is more random as easily seen in Fig. 39. There is evidence for areas having both intense small-scale mixing as well as the "stirring" types of larger scale motion described earlier for these inner regions. The LSTSs located at the outer edge of this jet consist of nearly lamarized outside edges surrounding regions in which scalar mixing takes place by two different mechanisms.

Figure 40 shows the pdf for Θ determined using the five radial positions centered about $r/r_o = -6$ in Fig. 39. Note that this pdf is formed only from pixels for which the mass fraction of propane is

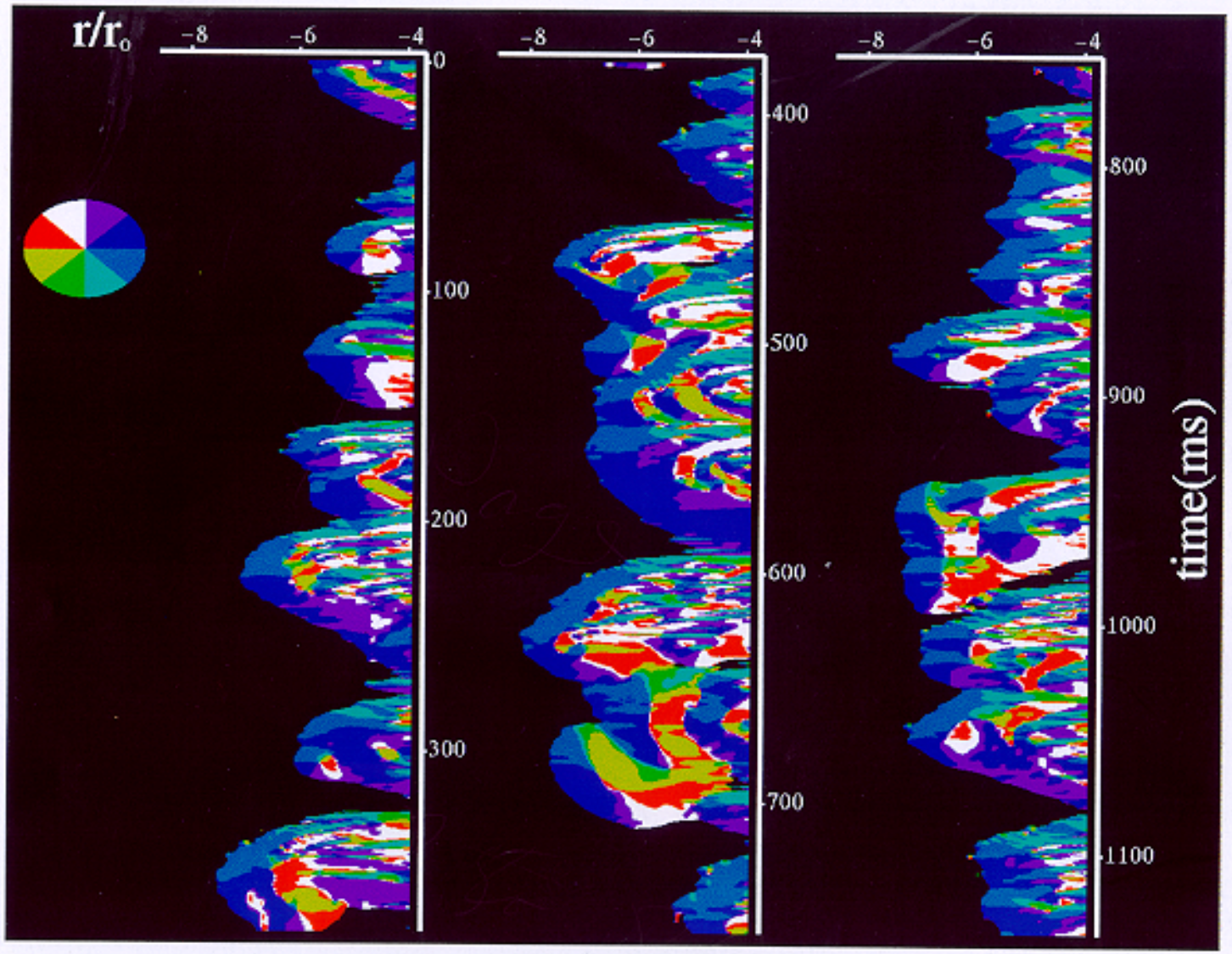

Figure 39. Values of Θ for 128 pixels in the r–z plane of the propane jet are plotted as a function of time for the Y data shown in Fig. 8a. The color wheel on the left–hand side shows the eight–level color coding used to represent angle. The upward direction on the wheel corresponds to the downstream direction of the flow (i.e., a concentration gradient aligned along the jet axis). Black regions designate locations where the mass fraction is less than 0.01.

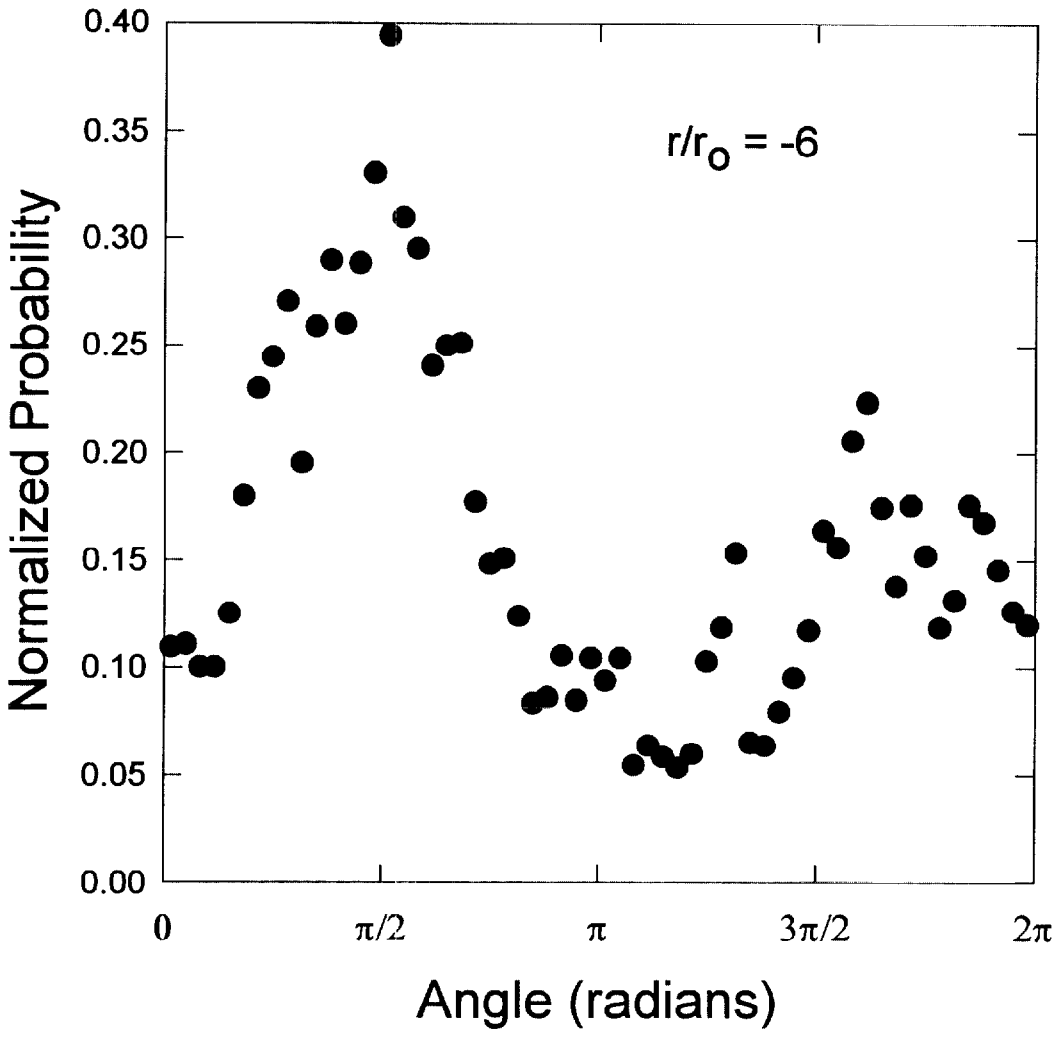

Figure 40. The pdf for Θ is shown for five pixels centered at r/r_o = -6 for a downstream position of 40 r_o. The pdf is formed from 7,344 out of 14,995 measurements for which the propane mass fraction exceeds 0.01.

greater than 0.01 (7,344 out of 14,995 measurements). The resulting pdf is highly asymmetric with gradient orientations aligned primarily along the radial direction having much higher frequencies of occurrence than those along the axial direction. Furthermore, gradients aligned predominantly along the radial direction are nearly twice as likely to point towards the jet centerline than outwards. These behaviors are consistent with those which would be expected based on the appearances of the mass fraction data in Fig. 8a and the gradient orientations plotted in Fig. 39.

IV. DISCUSSION

In this section the experimental findings discussed in the preceding section will be used as the foundation for discussion of three major points: 1) the nature and role of large-scale organized motion in mixing by axisymmetric turbulent jets, 2) the characterization of scalar dissipation behavior in this type of flow field, and 3) the evidence for the existence of coupling between LSTSs and the small scales responsible for molecular mixing.

A. ELSOSs, JCLSOSs, and FJLSOSs

As discussed in the Introduction, there have been numerous investigations which have attempted to educe the presence of organized large-scale velocity and concentration structures in downstream regions of axisymmetric jets. Three possible types of LSTSs were introduced: ejected large-scale organized structures (ELSOSs), jet-column large-scale organized structures (JCLSOSs), and full-jet large-scale organized structures (FJLSOSs). The vast majority of these studies have claimed to identify either ELSOSs or FJLSOSs. Apparently, the only previous discussion of JCLSOSs is the work of Tso and Hussain.[16]

Many of these investigations have focused on the possible existence of LSTSs involving the entire jet (i.e., FJLSOSs). The motivation (either implicit or explicit) for searching for these structures is the existence of comparable structures or "rollers" in two-dimensional mixing layers as originally reported by Brown and Roshko[7] and the possibility that such structures may be a general characteristic of a wide range of turbulent flows. In this model the large structures evident at the jet's outer edge are a manifestation of vortical structures covering the full-jet diameter. Some authors have claimed that such structures are formed near the jet exit and then grow continuously while being transported down the entire jet. On the other hand, studies identifying ELSOSs suggest the LSTSs at the jet's outer edge are due to more localized vortical structures which are considerably smaller than the jet width and are undergoing a continuous process of formation and destruction. The introduction of JCLSOSs can be viewed as a compromise allowing for the existence of both ELSOSs and vortical motions involving a significant fraction of the jet width which are more akin to those observed by Brown and Roshko.[7] JCLSOSs are expected to be considerably smaller than FJLSOSs since they should only exist in the central region of the jet.

It is important to recognize that many of the experimental results and conclusions of the studies summarized in the Introduction are contradictory and that no clear consensus concerning the existence or characteristics of LSTSs has emerged. In the authors' opinion, there has been very little effort to

compare and reconcile the findings of the wide range of studies dealing with LSTSs in fully developed axisymmetric jets. By utilizing the results of the current investigation along with a critical evaluation of previous research, the following discussion is an attempt to better understand the role of LSTSs. It will be the authors' conclusion that the evidence for the existence of ELSOSs is wide ranging and convincing, and, therefore, argues against the existence of FJLSOSs in axisymmetric jets. This conclusion will be justified before considering the possible existence of JCLSOSs in the flow.

Some of the strongest evidence for the existence of ELSOSs is found in early studies for which velocity measurements were made in order to identify the presence of LSTSs. In some cases, the velocity measurements were conditioned using simultaneous scalar results, while in other cases multiple velocity sensors were employed. Six of these earlier studies appear to have identified similar ELSOSs formed by relatively localized, abrupt ejections of jet fluid from core regions outwards into the ambient fluid.[9,10,11,12,14,15] The most detailed description of this type of LSTS is provided by Chevray (see his Fig. 14) who shows fluid being ejected with a "jet-like" motion from the central regions of the jet at an angle of roughly 60° to the z axis and generating a hairpin vortex which, in turn, forms the leading and tailing edges of the turbulent bulge.[11] Komori and Ueda show a similar cartoon (see their Fig. 11) based on their measurements.[14]

It is interesting that the size of the educed ELSOSs is consistent with the magnitude of the velocity integral scale measured for positions near the jet outer edge, which is reported to be $0.7(r_{\frac{1}{2}})_c$ by Wygnanski and Fiedler.[127] These authors found that the integral scale nearly doubled when the measurement location was moved from the centerline towards the outer edge of the jet. The variation in integral scale with r implies that the structure of the jet's outer edge is due to vortical motions which are larger or more organized than those closer to the centerline. The apparently localized motions suggested by the integral-scale magnitude is consistent with the formation of relatively localized LSTSs resulting from ejections of jet fluid from the core region of the jet. Considerably larger integral scales might be expected if FJLSOSs vortical motions were present. The studies of Komori and Ueda[14] and Tso et al.[15] include results for measurements which should have allowed the presence of FJSLOSs to be identified. Both groups found that educed structures at the outer edges of the jets were azimuthally localized and provided no evidence for the existence of FJLSOSs.

A significant number of measurements of scalar behavior at the outer edges of axisymmetric jets also provide evidence for the formation of ELSOSs. Several of the earlier investigations discussed above also included scalar measurements.[10,11,14] Conditional sampling based on the appearance of jet fluid allowed the structure of ELSOSs described by Chevray[11] and Komori and Ueda[14] to be identified.

One of the most dramatic manifestations of the formation of the LSTSs by ejection of jet fluid is the observation of ramp-like behaviors in single point time records of scalars recorded in the intermittent region of jet flow. As early as 1968 Gibson et al. had observed similar behaviors in the wake of a heated sphere.[128] Later work made it clear that such structures are characteristic of a wide range of shear flows, including axisymmetric jets.[18] Antonia et al.[9] noted the presence of ramp-like signals in the temperature signal for a heated axisymmetric jet, while Pitts and Kashiwagi[3] reported their occurrence for an axisymmetric jet of methane into air.

Based on early space-time images using the line camera, it was pointed out that the concentration behaviors near the outer edge of an axisymmetric jet are those expected for ejections of jet fluid such as described above.[24] The sharp concentration gradients evident in Figs. 7 and 8 for positions on the downstream edges of the structures near the jet outer edge are typical of those discussed in the earlier work. It was also noted that even though the concentration isopleths appear to be quite well aligned along the downstream edges of these structures, these positions are areas of rapid mixing as evidenced by a rapid fall off in the maximum concentration observed with increasing distance from the centerline.[24] The maintenance of sharp concentration gradients in the presence of strong mixing requires an active mechanism for sharpening the gradient.

A relatively short-lived ejection of fluid from a localized area of the jet core would be expected to result in mixing similar to that for vortex rings formed by short pulses of fluid through orifices into a large volume.[129,130,131] Such flows are known to generate "bubbles" of vorticity which grow and slow down as they move away from the starting position. Eventually, the bubble comes to a halt due to entrainment of ambient fluid into the bubble. The flow forms a wake in which small amounts of the ejected fluid as well as vorticity are left behind.

When similar structures are ejected at an angle to the downstream direction at the outer edge of an axisymmetric jet they will be strongly distorted by the strain rate and pressure fields associated with the jet. The portion of the ELSOS nearer the centerline will be accelerated while the flow further out will be slowed due to drag caused by the much slower moving ambient fluid. The regions of low pressure in the jet where strong entrainment of ambient fluid is occurring will tend to further slow the ejected fluid at the outer edge of the jet and even draw it back towards the jet centerline. As a result of these forces, the head, i.e., the downstream edge of an ELSOS is expected to be stretched along a direction parallel to the time-averaged principal strain rate. This explains the observation by Sreenivasan that the edges of LSTSs in the intermittent region tend to align at 135° to the downstream direction.[84]

The region separating jet and ambient fluids has been referred to as the "laminar superlayer" by Corrsin and Kistler, which will be shortened to "superlayer" for this discussion.[1] It should be remembered that these authors viewed the superlayer as being due to random motion of jet fluid, where today it would be argued that its most distinctive features are due to the formation of ELSOSs. The alignment of the concentration isopleths in Figs. 7 and 8, the sharpness and high levels of scalar dissipation in Figs. 30 and 31, and the distinctive variations of Θ seen in Fig. 39 along the outer edges of the LSTSs suggest that they are at least partially lamarized. It is also evident, however, from the data shown in Figs. 28 and 29 that smaller organized motions formed by ejected jet fluid can and do occur either within or near the superlayer. Presumably, these more localized LSTSs are the result of instabilities associated with the high strain rates expected at the edges of the larger ejected ELSOSs.

Corrsin and Kistler argued that the superlayer would be a region of high stretch rate which would result in a thinning of the superlayer. In fact, they speculated that it might be on the same order of size as the Kolmogorov scale. Chevray also points out that stretching of the interface along the downstream edges of the superlayer leads to increased surface area which keeps the interface sharp and results in increased mixing.[11] The observed behaviors in the current line camera measurements are certainly consistent with this view. Thus both the orientation of the downstream edges of the LSTSs and their concentration structure (i.e., high concentration gradients with high mixing rates) agree with the conclusion that these are ELSOSs. This explains the ubiquitous observation of ramp-like structures in the intermittency region of the jet. It is difficult to explain their existence by invoking FJSLOSs having much longer lifetimes.

One expected result of the formation of ELSOSs is that jet fluid will occasionally be ejected to the outer edge of the jet and, after losing its momentum, effectively become separated from the main jet flow and remain isolated for a brief period before being reentrained into the jet column. Evidence for the occurrence of this behavior has been reported and provides additional support that ejection of jet fluid is responsible for the formation of the type of LSTS most commonly observed at the outer edges of axisymmetric jets.[23,24,132,133]

The images of scalar dissipation and concentration gradient angles at the jet edge provide additional evidence that these LSTSs are ELSOSs and not FJLSOSs. Typical behaviors for χ_p near the outer edge of the flow are shown in Figs. 30 and 31 and for Θ in Fig 39. The "fishhook" shapes evident in the χ_p images are due to very high concentration gradients located on the downstream edges of the LSTSs which do not wrap around the entire structure. If the structures were formed by long lived coherent FJLSOSs one would expect the high concentration gradients to exist around the entire structure. It seems more plausible that the high values of χ_p are due to the highly strained bubble

formed by a localized ejection of jet fluid. The much lower concentrations of jet fluid observed behind the downstream edges of this type of LSTS are due to mixing within the bubble as well as jet fluid left behind in the "wake".

It was noted earlier that much of the mixing behavior within ELSOSs seems to be due to stirring motions as opposed to mixing on the much smaller scales observed closer to the centerline, which is to be expected for scalar dissipation as the result of a turbulent cascade. It is plausible that the stirring is the result of the passage of the "bubbles" formed by ELSOSs. If the LSTSs at the jet edges were due to FJLSOSs having roughly constant concentration, the small-scale structure would be expected to be relatively uniform over the entire jet radial profile.

The experimental evidence discussed thus far indicates that there are two distinct types of mixing processes in axisymmetric jets. In the outer, intermittent region of the flow mixing occurs by localized ejections of jet fluid and subsequent reentrainment due to ELSOSs which are similar to impulsively started jet flows. Regions nearer the jet centerline may contain JCLSOSs (see the discussion which follows), but behave more like classical diffusive turbulence. Additional evidence for two distinct types of turbulent behavior in these jets is available in an analysis by Drake et al.[134] These authors treated mixing in hydrogen turbulent jet flames and the isothermal mixing data of Pitts and Kashiwagi[3] for a methane jet using a procedure, originally suggested by Effelsberg and Peters,[135] based on the hypothesis that turbulent mixing can be broken into three distinct regimes--fully turbulent (Gaussian) zones, interface zones, and nonturbulent zones. The division into three zones was based on the behavior of the first four moments of the pdfs for scalar fluctuations at a point.[135] Drake et al. found that for regions near the centerline, where the intermittency factor is one, the methane jet behaved as if fully turbulent, but that as the sampling position was moved radially outward into the intermittent region the percentage of interface-type mixing rapidly increased to values exceeding 50 % of the turbulent fluid, indicating a profound change in mixing behavior. Such an observation strongly supports the presence of two distinct mixing behaviors and argues against the existence of FJLSOSs.

Effelsberg and Peters had previously observed a similar behavior for mixing in the wake of a sphere.[135] They attributed the interface mixing to the presence of superlayers analogous to those suggested by Corrsin and Kistler[2] in the intermittent region of the flow. Since the superlayer is expected to be spatially thin, it was necessary for the authors to hypothesize that the interface was highly convoluted with many passages of the superlayer taking place. This structure was referred to as consisting of "internal superlayers". Drake et al. argued against such a structure, pointing out that the interface regions were much broader than those expected for a superlayer (expected to have thicknesses roughly the size of η_B). They suggested instead that the interface regions were the result of the ramp-

like structures in the intermittent region of the flow. The current line camera measurements provide no indication of internal superlayers (see Figs. 7 and 8), but do indicate that the mixing of jet fluid at the outer edge of the flow is distinctly different than closer to the centerline. A plausible interpretation of the findings of Drake et al. is that the fully turbulent mixing regions at the jet outer edge occur in the bubble formed by the ejection of jet fluid while the "interface" regions correspond to mixing in the wakes of the rings which has been suggested to be the result of stirring motions induced by the passage of the bubble. Such an interpretation is consistent with the suggested structure of the flow shown in Fig. 18 of their paper.[134]

Another type of analysis which provides evidence for different mixing behaviors in regions near the outer edge of the jet and the centerline regions is that of Kerstein et al.[136] They introduced the concept of "conditional similarity" to analyze images of a flow field in an attempt to correlate the small-scale structure of the flow with the instantaneous large-scale structure. An approach was adopted in which the width of the jet along the radial direction was used as a selection criteria. Large widths were found to correspond to radial profiles which had average and rms profiles differing substantially from those for narrow profiles. In particular, the maximum in the rms for the wide profiles was found to be near the outer edges of the averaged data, while the narrow profiles had peaks in the rms much closer to the location where ambient air and jet fluid are expected to be strongly mixed. If the reasonable assumption is made that the wide profiles are due to periods during which ELSOSs are present, the high rms values at the outer edge result from the mixing behaviors discussed earlier. In the absence of ELSOSs, the strongest mixing should occur at locations where the core region of the jet interacts directly with the surroundings, as observed.

The high frequency with which this type of LSTS is observed at the jet outer edge indicates that the ejection of jet fluid is an integral part of the mixing process and that the shape of the instantaneous outer edge of the jet will be determined to a large degree by the formation of ELSOSs. Since the ejections are expected to be of relatively short duration, ELSOSs must be undergoing a continuous formation and destruction processes in which they are first ejected into the surrounding ambient fluid and then reentrained along with ambient fluid into the core region of the jet flow. Earlier work has shown that there are strong inward flows of ambient gas for positions immediately upstream of ELSOSs.[10,11,14] For this reason, it has been speculated the ejection of jet fluid along with the rapid inflow of ambient fluid is a fundamental process responsible for a significant fraction of the spreading of the jet and ambient fluid entrainment which occurs with increasing downstream distance. The importance of these structures in jet mixing has been noted by numerous authors (e.g., see references 17, 19, 21, 22, 24, and 28).

It is believed by the current authors that the evidence discussed above for the existence of ELSOSs and their dominant role in mixing at the outer edges of axisymmetric jets is overwhelming. However, as discussed in the Introduction, there is an extensive published literature suggesting that FJLSOSs exist and are central to the understanding of mixing behavior in axisymmetric jets. It is therefore important to consider the evidence for the existence of FJLSOSs and, where possible, demonstrate that it is also consistent with the formation of ELSOSs.

Behaviors which have been attributed to FJLSOSs have been observed in both liquid and gas jets based on a number of features observed in various types of two-dimensional (instantaneous z-r, z-t and r-t) images.[17,19,21,23,27,28] Both passively mixing and reacting flows have been studied. Characteristics which have been reported as indicating the presence of FJLSOSs include: 1) large volumes having relatively constant concentration which can extend across the full radial extent of the jet and which are transported downstream with nearly constant velocities, 2) the observation of radial profiles having two well defined concentration levels suggesting a possible nesting of axisymmetric FJLSOSs, 3) the observation of jet outer edges in planar images which are interpreted as being due to either axisymmetric or helical FJLSOSs, 4) narrow regions of very rapid concentration and velocity change between the large regions of relatively constant concentration, and 5) the reaction behavior observed at the downstream positions of reactive jets which indicate that the reactive scalar disappears nearly instantaneously over a large volume of the jet.

Consider first the observations concerning radial profiles. The picture of ELSOSs which has emerged consists of a turbulent jet core region from which LSTSs are periodically ejected. If a radial profile is recorded during periods when ELSOSs are not present the observed concentration field is expected to be that for the jet core which should have a relatively uniform scalar concentration over a relatively narrow radial width. On the other hand, when ELSOSs are present the radial profiles should be broader and have considerably lower concentrations at the outer edges due to the rapid mixing which takes place within ELSOSs. Such a radial profile could be interpreted as having two distinct concentration levels. It is significant that results from the analyses developed by Drake et al.[134] and Kerstein et al.[136] support this view of two distinct mixing behaviors.

Figure 11 shows an *r-t* image of *Y*, recorded for radial positions which include the jet centerline, using a three-level false-color scale chosen to highlight regions of relatively constant concentration separated by narrow bands of high mass-fraction gradient. This image was intended to capture similar details concerning mixing as an image shown by Papantoniou and List (see their Fig. 7a) for a dyed water jet.[23] Their image, which covered the entire radial extent of the jet, shows a clear, regular temporal alteration in scalar concentration near the centerline with narrow radial bands

of high concentration being followed by regions of lower concentration. As already noted, such organized structure is not evident for the propane jet results shown in Fig. 11.

The behavior of the scalar dissipation discussed in the Results section does provide a hint that a similar structure may be present for the propane jet. When a narrow region separating two more extensive regions having significantly different concentrations passes the observation point, a band of high scalar dissipation values should be observed across the jet. Evidence for the existence of such bands has already been discussed in the Experimental Results section. However, it has also been pointed out that the occurrence of these bands does not necessarily correlate with the ELSOSs observed at the jet outer edge.

Based on the planar images, FJLSOSs have been interpreted as being either axisymmetric, helical, or in transition between the two forms. Such structures have been justified in terms of a stability analysis for axisymmetric jets provided by Batchelor and Gill which predicts that axisymmetric and helical structures can be stabilized in fully developed jets.[137] Perhaps the strongest evidence against such an interpretation is provided by Yoda et al.[36] Using instantaneous three-dimensional scalar images, these researchers showed that orthogonal data planes did not provide consistent view of such structures. For instance, while one plane might suggest the presence of a helical FJLSOS, the second might suggest a circular FJLSOS. While the authors speculated that both positive and negative helical modes may be simultaneously present, it is believed by the current authors that this observation is due to the presence or absence of more localized ELSOSs.

As already noted, one of the major cornerstones supporting the existence of FJLSOSs has been the claim that planar images indicate that jet flows contain large regions of roughly constant concentration which extend out to the very edges of the flow field.[17,19,21,23,27,28] However, close inspection of Fig. 7a in Papantoniou and List indicates that obvious LSTSs at the outer edge of their water jet always have significantly lower concentrations than connected regions nearer the centerline.[23] It seems probable that these structures are actually due to ELSOSs. An explanation for these regions having lower scalar concentration has already been provided.

Shlien's investigation of the mixing of entrained ambient fluid into a water jet discussed in the Introduction supports the conclusion that initial jet entrainment and subsequent mixing are dominated by relatively localized ELSOSs (as opposed to FJLSOSs). The rapid entrainment at upstream edges of ELSOSs is evident in his images. The smooth spreading of the ambient fluid towards and across the jet centerline and the localization of the vast majority of entrained fluid along the edge of the jet where entrainment has occurred are consistent with a localized event instead of rapid dispersion by organized vortical structures involving the entire flow field.

The identification of reaction surfaces in turbulent flows provides another approach for characterizing mixing. Since chemical reaction requires intimate molecular mixing, the disappearance of a reactive scalar is a measure of molecular mixing which is not expected to be strongly dependent on the experimental spatial resolution. Dahm et al. were the first to point out that the periodic "flame" length fluctuations in a reacting turbulent jet must be associated with an organized LSTS in the jet flow.[138] Such behavior is evident in the later work of Dahm and Dimotakis where the "flame" tip for the acid/base reaction showed the characteristic oscillation described in the Introduction.[19] This behavior is strong experimental evidence for the existence of either FJLSOSs or JCLSOSs which are characterized by relatively constant concentration. The observation of a similar behavior in high Reynolds number combusting jets of acetylene and ethylene suggests that the fluctuations are a general characteristic of axisymmetric jets.[29,32]

Even though the appearance of a separated reaction zone at the downstream end of a turbulent reacting jets has been taken as an indication of the presence of FJLSOSs, inspection of the behavior of the separated reacting regions suggests that this is not the case. In their idealized view of these structures, Dahm and Dimotakis hypothesize that the concentration is nearly uniform across the entire radial extent of the jet.[19] However, their images show that the separated unreacted regions at the downstream end of a reacting jet have widths which are typically much less than $0.1z$, while the full jet width is expected to be on the order of $0.4z$. This requires the fluid at the edge of the jet be at concentrations less than stoichiometric over significant radial distances, and thus requires a substantial fall off of jet fluid concentration in the radial direction. Recall that the work Papantoniou and List shows just such a fall off.[23] Mungal and O'Neil have previously noted that the observed reaction zones are considerably narrower than the overall width of the flow.[30]

Pitts[26] has discussed why a narrowing of the reaction zone is to be expected in terms of time-averaged concentration profiles which lead to the observation of a cigar shape for jet diffusion flames. He noted that the region where combustion is occurring at the end of a turbulent flame is well inside of the radial position where the intermittency factor reaches one. In other words, there is no direct contact between the reacting fluid and ambient air. The results of Shlien suggest that mixing of ambient fluid in this region of the jet is more diffusional in nature than in the outer regions of the flow where LSTSs dominate.[22] The mixing responsible for the burnout of the separated high concentration fluid must result from entrained fluid being distributed within the core region of the flow. The observed behavior of the burnout (i.e., burnout occurs over a relatively large extent of the separated fluid nearly instantaneously) requires that the entrained fluid entering the core region (presumably by

"gulping" due to ELSOSs) is dispersed over the region at a rate roughly comparable to the rate at which it is being entrained. This conclusion does not require the existence of FJLSOSs.

Based on the discussion thus far, it is clear that, when considering the mixing behavior at the outer edge of axisymmetric jet, the experimental observations which have been used as justification for the presence of FJLSOSs can be interpreted equally well in terms of ELSOSs. In fact, in certain cases, e.g., the reaction behavior at downstream positions in reacting jets, the experimental evidence actually favors the existence of ELSOSs. Note that some of these observations can also be interpreted in terms of the presence of JCLSOS. This point is discussed further below.

Perhaps the hardest experiments to understand in terms of the characteristics of EJLSOSs are the experiments of Mungal and coworkers concerning LSTSs which the authors classify as FJLSOSs.[29,30,31,32,33] These authors provide evidence that the LSTSs which are primarily observed at the outer edges of turbulent jets form near the jet base and are transported over extremely long axial flow distances. This view is clearly inconsistent with the expected behavior of EJLSOSs which are viewed as relatively short-lived and spatially localized pulses of jet fluid from the core regions. One possible way that the two views could be reconciled would be for the formation of ELSOSs to be highly correlated in space and time. The experiments used to support the existence of localized ELSOSs have failed to identify such a high degree of correlation.

The findings of Mungal et al. are based on analysis using two-dimensional images of the flow field (either integrated projections or planar imaging). The observation of the structures over such long flow distances requires that they remain localized within a narrow azimuthal angle of the jet over the same flow distance. This is only possible if there is little or no azimuthal rotation of the proposed JCLSOSs around the centerline over the period required to cover the large axial distances. This does not seem reasonable. The authors discuss some possible explanations as to how random processes might lead to the observed behavior, but argue convincingly that the behaviors are real.[32] A possible explanation that does not seem to have been considered by the authors is that once a large projection of fluid has developed at some downstream location due to the presence of an ELSOS, naturally random processes could result in the bulge being maintained. While we believe it is very unlikely that individual LSTSs observed at the edge of these jets actually form close to the jet exit and are subsequently transported over long distances, we can offer no definitive counter explanations for the observations of Mungal and coworkers. This is a question which can only be settled by additional research.

The last point to be addressed in this subsection is whether or not LSTSs are present within the jet core, i.e., do JCLSOSs exist as originally suggested by Tso and Hussain[16] The conclusion that

relatively localized ELSOSs are responsible for the LSTSs routinely observed at the outer edges of axisymmetric jets must be kept in mind when attempting to identify JCLSOSs. As discussed in the Introduction, in their investigation of LSTSs using velocity measurements, Tso and Hussain educed the presence of an organized motion in the flow which was attributed to axisymmetric, helical, and double helical JCLSOSs isolated within the core region of the jet.[16] Significantly, these authors explicitly acknowledged the existence of both types of LSTSs and concluded that both are likely to be important for the entrainment and mixing of turbulent jets. Some additional evidence for the possible existence of JCLSOSs is available in power spectra and autocorrelations for scalar fluctuations which suggest the presence of a weak large-scale behavior for locations near the jet core.[12,23,139]

It is difficult to anticipate the signatures for the JCLSOSs identified by Tso and Hussain[16] which would be expected for the spatial-temporal images of mass fraction, scalar dissipation, and mass fraction gradient orientation recorded in the present work. Tso and Hussain did note that a single two-dimensional image of the concentration field of a water jet recorded by Dimotakis, Miake-Lye, and Papantoniou[17] showed a zigzag pattern which they interpreted as being indicative of the presence of a helical JCLSOS. A similar behavior is evident in Fig. 7(a) of Panpantonious and List.[23] However, as already discussed, the outer edge of a jet determined from two-dimensional measurements will be dominated by the behavior of ELSOSs and is unlikely to provide clear evidence for LSTSs within the jet core. It is our opinion that attempting to identify JCLSOSs based on two-dimensional concentration images is risky for the following reasons: 1) EJLSOSs, which have been shown to occur frequently, will obscure the presence of such structures, 2) the JCLSOSs are believed to be constantly changing between different modes (circular, two helical, two double helical) with random, and as, yet unspecified rates, and 3) the JCLSOSs are characterized as having a great deal of randomness in shape, size, and phase[16].

Clearly, more subtle jet characteristics than simple jet profiles need to be considered in order to identify the presence of JCLSOSs based on scalar measurements. While not conclusive, sufficient experimental evidence is available from past studies as well as the current work to suggest that the velocity and scalar fields in the jet core do have an underlying LSTS.

Even though it has been argued that FJLSOSs do not play a dominant role for mixing in axisymmetric jets, its is true that much of the earlier experimental evidence cited to support their existence, as well as other experimental results, does support the existence of organized motion involving interior regions of the jet. In particular, the internal ramp-like structures discussed by Sreenivasan et al.[12] and Gibson et al.,[18] the alternating patterns of localized regions of high and low concentration reported by Papantoniou and List,[23] and the distinct temporal variations of reactive

scalars at the downstream edges of reacting flow[19,21,30] suggest the presence of an underlying large-scale structure near the jet centerline. A strong argument can be made that each of these observations is related to the average scalar structure for a JCLSOS. Such a structure requires a roughly constant scalar concentration, a characteristic also attributed to FJLSOSs, which is separated from adjacent structures by narrow bands where the concentration increases rapidly in the upstream direction, and which has a small countergradient to the average centerline concentration fall off, such that the concentration across the structure would increase very slowly with downstream distance. The clearest evidence for the last point is found in reactive scalar investigations which show the reactive scalar disappearing from the upstream end of an extensive volume of the jet.

While the current experiments have failed to confirm the systematic variations of concentration near the jet centerline observed by Papantoniou and List[23] (consider Fig. 11), there are several aspects of the results which indicate that JCLSOSs exist and have a distinct internal ramp-like structure. The presence of localized regions of high scalar dissipation which extend across the central regions of the jet has already been discussed. Close qualitative comparisons of the times of these occurrences in the scalar dissipation images shown in Figs. 12, 22, and 30 with the corresponding times in the image for gradient angle (Fig. 37) shows that the strong gradients responsible point predominantly upstream as expected for internal ramp-like structures.

Most of the observation period at a given downstream distance is expected to be spent at locations within the jet corresponding to the interiors of JCLSOSs. Since these interiors are viewed as having roughly constant scalar concentrations with a mild superimposed countergradient, it would be expected that pdfs for the gradient angle would be skewed toward angles pointing in the downstream direction. As shown in Fig. 38, gradients pointing along the jet centerline are roughly twice as likely as those pointing upstream.

There is an additional aspect of the current findings that supports the existence of JCLSOSs in the flow. This is the systematic variation of the scalar dissipation behavior between intense and less robust mixing regions observed for the central region of the jet. Such variations have been noted in images for the individual radial and axial components of scalar dissipation, as well as those for the planar measurements obtained by combining the two components. The results shown in Fig. 30 for radial positions which cross the jet centerline provide the clearest examples of this behavior. Due to the limited acquisition times, it is not possible to perform a meaningful statistical analysis of this behavior, but a qualitative visual analysis indicates that roughly ten cycles occur during the 1.114 s shown in Fig. 30, suggesting a period of $\approx$ 0.110 s. This is roughly twice the value of τ_{jd} estimated

using the local full-jet diameter and $\bar{U}_m$. The most plausible explanation for these distinct, systematic variations in small-scale mixing behavior is that they are coupled to the passage of JCLSOSs.

Very little is known about the possible organization of turbulent flows into areas having high and low molecular mixing rates (i.e., high and low scalar dissipation). However, the existence of localized clumping of energy dissipation has long been recognized in turbulent flows. The first report of such a behavior was that of Batchelor and Townsend who reported results for decaying grid turbulence.[140] Later work by Kuo and Corrsin showed that a similar behavior occurs in axisymmetric jets.[141] The latter authors also showed that the regions of intense activity extended over distances which were significantly greater than the Kolmogorov scale, and for relatively low Reynolds numbers the scale ratio was on the order of 60 to 80. This ratio can be compared to that for the largest and Kolmogorov scales in the current experiments, $L_{jd}/\eta_K = 333$. There is roughly a factor of four difference. This does suggest that the regions of high energy dissipation are organized into structures of size comparable to the largest turbulent structures in the flow. Tso and Hussain reported systematic variations in a Reynolds-stress term across JCLSOSs which were attributed to differences in momentum redistribution by small-scale structures. The most intense regions were located at the downstream sides of the JCLSOSs.[16] Dahm et al. have described the "spottiness" of the scalar dissipation in dyed water jets.[37,38,47,59] These measurements were made over a relatively small fraction of the jet width and did not address a possible dependence on large-scale structure.

The only experimental evidence of which the authors are aware for a similar large-scale clumping of the scalar dissipation in axisymmetric jets is indirect. Magnussen et al. have observed an intermittent behavior for the distribution of soot in turbulent jet diffusion flames which they showed was associated with LSTSs having a size on the same order of magnitude as the integral scale.[142,143] If one assumes that the distinctive soot distribution is a result of soot formation in regions where scalar dissipation is high (i.e., where the combustion rate is expected to be high), their results indicate a large-scale variation for scalar dissipation similar to that observed in the current investigation. Mungal and O'Neil have speculated that the soot intermittency behavior is indicative of the presence of FJLSOSs,[30] while it is argued here that more localized JCLSOSs are responsible.

It should be pointed out that the localized formation of ELSOSs at the jet's outer edge could be correlated to some degree with the behavior of JCLSOSs in the central region of the flow. An analogous behavior has been observed in boundary-layer mixing where a dynamical relationship was observed between large-scale intermittent turbulent bulges and relatively small-scale bursting phenomena near the solid surface.[144] If such a connection is present in axisymmetric jets, the formation and destruction of ELSOSs could serve as potential markers for JCLSOS structure.

Techniques for identifying the location of ELSOSs at the jet outer edge in real time while simultaneously reliably detecting and characterizing JCLSOSs must be developed before the true nature of such potential interactions can be assessed. Obviously, such measurements present a formidable technical challenge.

Thus far, the possible effects of *Sc*, the relative molecular diffusion rates for momentum and composition, have not been considered. Results for water and gaseous jets have been considered together, and conclusions have been based on experimental observations in both types of jets, even though the Sc in gas jets are close to 1, while those for dyed water jets vary from roughly 600 to 2000. It should be cautioned, however, that there is abundant evidence that the mixing behavior and scalar topology in axisymmetric jets depends on *Sc*. In the Introduction it was noted that ambient fluid is observed on the jet centerline in high Sc jets, while $Sc \approx 1$ jets have intermittency values of 1 on and near the jet centerline. Measurements suggest that the fraction of ambient fluid at the centerline of water jets decreases with increasing Re.[21] Dahm and Dimotakis have noted that the typical ramp-like structures, which are so characteristic of mixing in the intermittency regions of gas jets, are not evident in water jets.[21] Furthermore, due to the high Sc in dyed liquid jets, the scalar dissipation is organized into distinct thin layers which extend over areas having much longer characteristic lengths than their thickness.[38,47,59] In gas jets, the characteristic length scales for the areas of the scalar dissipation sheets are the same order of size as the sheet thickness.[47,57] While all of these differences in properties complicate comparisons between the two types of flow, it seems likely that conclusions regarding LSTS behavior based on observations in either type of flow are valid since the experimental evidence suggests that gross features of turbulent jets, such as entrainment and spreading rates, are independent of whether the fluid is a liquid or a gas. Since these features are dominated by LSTS behavior, this is strong evidence that LSTS structure is similar in both cases and is nearly independent of molecular-scale processes such as viscosity and molecular diffusion.

From the above discussion, it is clear that the existence and characterization of LSTS has been a major focus of research in axisymmetric jets. While not discussed in detail here, the same is true for other types of turbulent shear flows as well. Much additional work is required before the nature and role of LSTSs in such flows is completely characterized and understood, however, the experimental evidence supports the following conclusions for axisymmetric jets:

1. Organized LSTSs are present and play a fundamental role in turbulent diffusion of momentum and jet fluid.
2. Organized LSTSs are particularly evident at the jet's outer edge. The strongly intermittent behavior observed in this region results from the formation of ELSOSs by relatively intense

ejections of jet fluid which occur over relatively limited times, axial distances, and jet circumference, followed by subsequent reentrainment of mixed ambient and jet fluid.

3. Evidence for the existence of JCLSOSs in jet core regions is not as conclusive as for ELSOSs, but strongly suggests that there is an underlying large-scale organized motion for locations near the centerline. The experiments of Tso and Hussain indicate the primary vortical structures responsible for these structures are helical.[16] JCLSOSs are most likely responsible for the appearance of internal ramp-like structures and the large-scale variations in small-scale mixing behavior observed in the current experiments.

Broadwell and Mungal reviewed many of the studies prior to 1991 which have been used to provide a justification for the existence of FJLSOSs in axisymmetric jets.[35] On the basis of these studies they have proposed a model for chemical reactions in these flows which divides the jet into two regions--outer locations where mixing primarily takes place in Taylor layers between mixed jet/ambient fluid and the ambient fluid and an inner region near the jet centerline where mixing is treated as homogeneous. The authors point out a similarity between their conclusions and the work of Effelsbergs and Peters[135] discussed above. The division of the jet into two distinct mixing regions is consistent with the current conclusions, but it should be kept in mind that the underlying physical models are very different. The Broadwell and Mungal approach is based on the hypothesis of the existence of FJLSOSs which are nearly uniformly mixed and involve the entire radial extent of the flow, while it is argued here that the experimental evidence suggests the outer region of the flow actually consists of considerably smaller ELSOSs which are ejected from the jet core region which has its own, more or less, independent large-scale organization (i.e., JCLSOSs).

B. Characterization of Scalar Dissipation

Before discussing the results of the scalar dissipation measurements in detail and comparing them with literature measurements, the points emphasized in the Introduction will be considered in light of the current measurements. It is clear from the images shown in Figs. 12, 13, 22, 23, 30, and 31 that there can be substantial variations in instantaneous scalar dissipation values over distances corresponding to the spatial resolution of the experiment. Values summarized in Table 2 indicate that the effective spatial resolution is roughly 2.1 to 2.6 times η_B. It is clear from this observation that the spatial resolution cannot be decreased without degrading the measurements and spatially averaging the results. Earlier studies suggesting that significantly relaxed resolution requirements are appropriate should not be used to specify resolution requirements for scalar dissipation measurements.

The close agreement between the experimental pdfs for $\log(\chi_r)$, $\log(\chi_z)$, and $\log(\chi_p)$ and values of $\log(\chi_{1D})$ and $\log(\chi_{2D})$ which is evident in Figs. 18, 25, and 33, respectively, indicates that the analyzes suggested by Dahm and Buch[79] and Buch and Dahm[47] provide valid approaches for estimating the pdf of $\log(\chi)$ from experimentally determined pdfs for the logarithms of components along a single axis or in a plane. Keep in mind that the measurements shown in the figures were made on the jet centerline where the approximation that χ is isotropic appears to be valid (see discussion below) and for which the use of Taylor's hypothesis has been shown to be the most accurate[123,124]. The projection methods would not be expected to provide reliable estimates for the average and rms of $\log(\chi)$ in regions of the flow where χ is nonisotropic, such as at the outer edge of the jet.

The pdfs for the scalar dissipation measurements were characterized in terms of log values because the pdf for χ was expected to be log-normal or nearly log-normal. The close agreement of the experimental pdfs for χ_r, χ_z, and χ_p with calculated pdfs for χ_{1D} and χ_{2D} based on an assumed log-normal distribution for χ confirms this expectation. However, it also of interest to consider the behavior of linear pdfs for χ_r, χ_z, and χ_p since average values of scalar dissipation, $\overline{\chi}$, are often used for modeling purposes, and previous experimental results for the average and rms, χ', have most frequently been reported in linear terms.

The transformation of a log distribution into a linear distribution is straightforward when it is noted that

$$P_\chi d\chi = P_{\ln\chi} d(\ln\chi) = \frac{P_{\ln\chi} d\chi}{\chi} , \tag{36}$$

which leads to

$$P_\chi = \frac{P_{\ln\chi}}{\chi} . \tag{37}$$

Here ln refers to the natural logarithm and P_χ and $P_{ln\chi}$ are the pdfs for χ and $\ln\chi$, respectively. When $P_{\ln\chi}$ is a log-normal distribution, values $\overline{\chi}$ and χ' are given by[145]

$$\overline{\chi} = e^{\overline{\ln\chi} - \frac{(\ln\chi)'^2}{2}} \tag{38}$$

and

$$\chi' = e^{2\overline{\ln\chi} + (\ln\chi)'^2}\left(e^{(\ln\chi)'^2} - 1\right) = \overline{\ln\chi}^2\left(e^{(\ln\chi)'^2} - 1\right) . \tag{39}$$

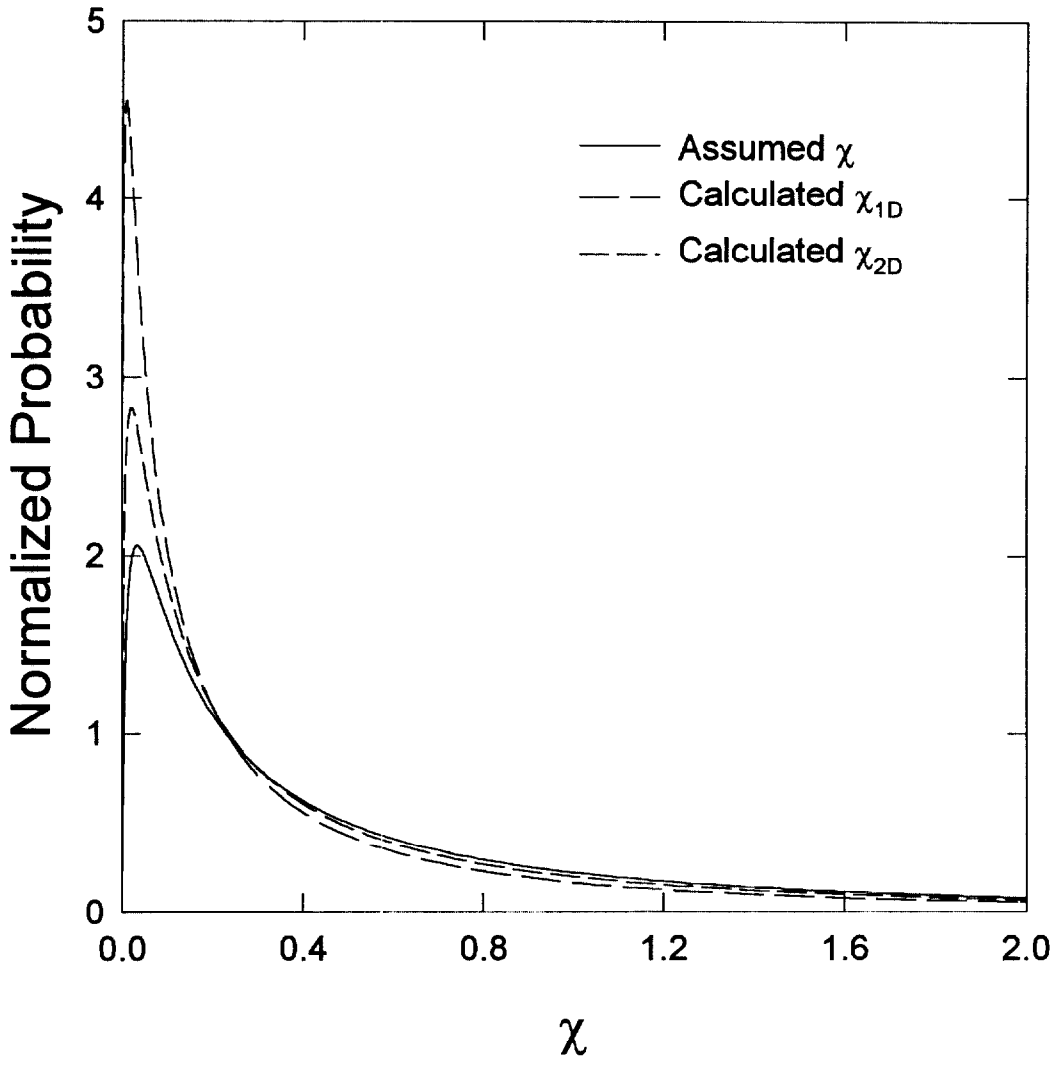

Figure 41. Normalized pdfs for χ_{1D}, χ_{2D}, and χ are shown. The pdfs are obtained by transforming pdfs for the log of the corresponding variable.

These equations are in terms of natural logarithms, but conversion to base 10 is straightforward.

The use of linear values for a log-normal pdf yields a pdf for χ in which small values of χ are much more probable, but which also has a long, low probability tail extending to large values of χ as has been reported previously.[46] This can be seen in Fig. 41 where the pdf for $\log(\chi)$ used to generate pdfs for $\log(\chi_{1D})$ and $\log(\chi_{2D})$ has been transformed to a linear pdf and normalized to have a total probability of one. Similar pdfs are included for χ_{1D} and χ_{2D}. The strong shift of the pdfs towards low values is evident for both χ_{1D} and χ_{2D}. Note that the maximum probability for the pdf of χ_{1D} extends to much larger values (maximum of 6133 at $\chi = 9 \times 10^{-8}$) than shown in the figure. The characteristics of the linear pdfs have important practical implications when experimental data are used to determine

statistical moments or pdfs. For instance, values of χ, or its projection onto an axis or into a plane, cover a range of several orders of magnitude, with smaller values strongly favored. If one attempts to use a typical "bin counting" approach to determine a pdf from such a strongly skewed linear distribution, it is quickly discovered that a very large number of bins, roughly comparable to the ratio of highest and lowest values of χ, is required to adequately define the pdf. If a much smaller, and more reasonable, number of bins is used, the full distribution is not reproduced and the first bin always contains the largest count. The resulting pdf is cut off on the low side and statistical values determined from the pdf are subject to large errors.

Another feature of the strongly skewed linear pdfs is that the moments of the distribution are extremely sensitive to the high value, low probability occurrences of the variable. As a result, moments for χ or its components determined from experimental distributions are subject to statistical noise due to the low probability of high values as well as experimental artifacts (e.g., temporal or spatial resolution limitations) which tend to smooth, i.e., lower, the highest and most infrequent values. For instance, a failure to accurately determine the high end of a distribution would lead to average and rms results which are significantly smaller than the true values. The high probability of observing very small values of χ or its components, i.e., orders of magnitude smaller than the highest values, also has implications for the accuracy of moments determined from the experimental measurements. When significant noise is present in individual concentration measurements, it is impossible to resolve the smallest values, and measured results for the smallest values will be, in general, considerably higher than the actual values. This effect of measurement noise is evident in the calibrations of Antonia and Mi[50] and Anselmet et al.[51] where increasing average values for single components of χ are recorded with decreasing cold-wire separation as the noise in the measurements becomes more significant. When experimental noise leads to measured values greater than the actual values, average values will be overestimated while the rms is underestimated. The effects of such measurement errors can be quite significant due to the high probability of occurrence for the lowest values of χ and its components.

Average and rms values for linear distributions calculated from the experimental measurements of χ_r, χ_z, and χ_p as well as the transformed log-normal distributions for χ_{1D}, χ_{2D}, and χ are included in Table 3. Comparison of the experimental one- and two-dimensional results with the corresponding model values shows that both average and rms values are higher for the model pdfs than observed experimentally, despite the close agreement of the corresponding parameters when calculated in terms of log values. These discrepancies are due to the experimental and model distributions having different probabilities for the highest values of χ and its projections onto an axis or into a plane

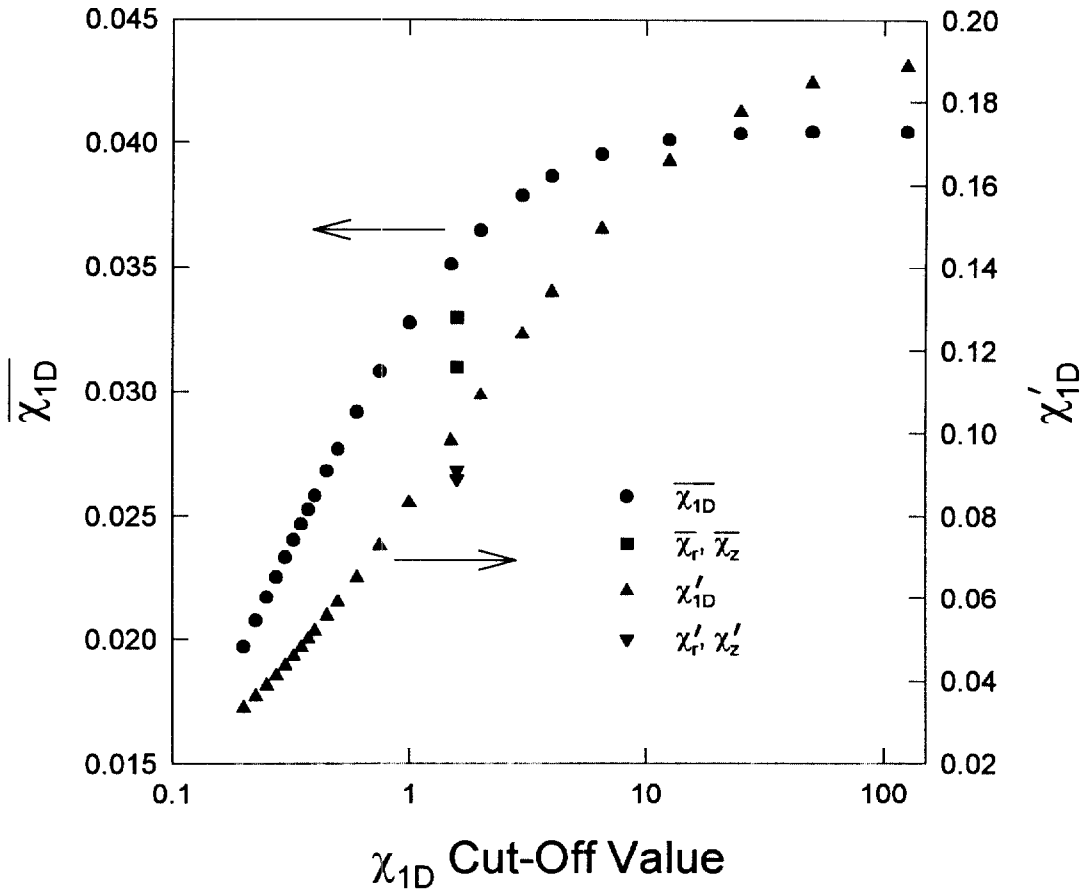

Figure 42. Average and rms values of χ_{1D} calculated from truncated pdfs are plotted as functions of the χ_{1D} value (log scale) above which the pdf is cut off. Corresponding experimental values for χ_r and χ_z are plotted assuming a cutoff value of 1.59 s^{-1}.

combined with the strong influence of these highest values on the statistical behavior. The differences between the experimental and model pdfs are barely discernible in Figs. 18 and 33 where it can be seen that the experimental values in log terms have probabilities which fall off more rapidly than the calculated values of χ_{1D} and χ_{2D} at the high ends of the distributions. For instance, the highest experimental value of χ_r observed in the data used to form the pdf shown in Fig. 18 is 1.59 s^{-1}, while values of χ_{1D} greater than 100 s^{-1} contribute to the average and rms values.

Figure 42 shows average and rms values of χ_{1D} obtained when the high end of the pdf has been truncated at the indicated values. Also included are the corresponding experimental values for the radial and axial directions plotted assuming a cutoff value of 1.59 s^{-1}. The experimental values fall very close to the corresponding calculated curves. This figure quantifies the statements above concerning the effects of the long tail towards high values on the statistics for scalar dissipation, while

at the same time demonstrating the care which must be used when transforming a log-normal to a linear pdf.

For the pdfs in log terms it was found that the strong asymmetry towards low values introduced by projecting values of χ onto a single component or into a plane resulted in average values which were significantly less than would be expected based on the use of approximations such as Eqs. (3) and (4). Corresponding estimates for the model linear pdfs, $3\overline{\chi}_{1D} = 0.122$ s^{-1} and $1.5\overline{\chi}_{2D} = 0.123$ s^{-1}, are included in Table 3. It is somewhat surprising to find that these approximations agree well with the actual value of $\overline{\chi}$. The reason is again due to the properties of a projection of a three-dimensional derivative onto a single axis or into a plane. The highest values in the projected pdfs can only occur when the mass fraction gradient lies along or very close to the direction of the component being measured in the χ_{1D} case or in the plane for the χ_{2D} case. As a result, values at the high end of these pdfs tend to approach those for χ and the probabilities for the projected components are actually overestimated at the extreme high ends of the pdfs. This overestimation is in the opposite direction from that for most of the pdf. Recalling that the largest values dominate the calculation of an average value, the observation of $\overline{\chi}_{1D}$ and $\overline{\chi}_{2D}$ values consistent with an isotropic distribution indicates that the two types of distortions roughly cancel each other.

Even though the opposite distortions of the pdfs cancel for linear averages, it would be expected that rms values would be considerably overestimated using χ_{1D} and χ_{2D} since the pdfs are distorted in opposite directions at the high and low ends. This expectation is confirmed by the results summarized in Table 3. Since the pdf for χ_{1D} is more distorted by geometrical effects than that for χ_{2D}, the χ rms estimated from this pdf is overestimated to a much greater degree.

The model results suggest that Eqs. (3) and (4) should provide good estimates for $\overline{\chi}$ from $\overline{\chi}_r$, $\overline{\chi}_z$, and $\overline{\chi}_p$ despite the truncation at higher values. These estimates are included in Table 3. The three experimental values cluster around $\overline{\chi} = 0.096$ s^{-1}.

To the authors' knowledge, the estimates for averages and rms values for $\log(\chi)$ and χ included in Table 3 are the first measurements which have been reported for scalar dissipation in gas flows where the data are sufficiently spatially and temporally resolved to determine the full pdf and for which the effects of projecting the measurements onto a single axis or into a plane have been included in the data analysis. There have been numerous values of time-averaged one- and two-dimensional scalar dissipation components reported in the literature. It is of interest to compare the results of the current work with corresponding literature estimates in order to check for consistency and provide a means for estimating scalar dissipation levels in cases where measurements are not available.

Centerline values have been chosen for comparison since the measurements reported here are expected to be most accurate at this location, and the most extensive literature results are also for this case. Measurements have been made in axisymmetric jets formed by a variety of different gases as well as heated air jets and for a range of initial conditions and downstream distances. In order to compare the different results it is appropriate to try and nondimensionalize the data in a manner expected to collapse the results. There have been limited efforts in the literature to theoretically predict the expected behavior of $\overline{\chi}$ as a function of jet parameters and measurement location which can be used for this purpose.

Peters and Williams[42] used an analogy with the predicted and experimentally observed behavior for the time-averaged turbulence kinetic energy in axisymmetric jets[76] and nondimensional analysis to conclude that centerline $\overline{\chi}$ values should be inversely proportional to the downstream distance to the fourth power. By assuming that

$$\overline{\chi} = \left(\frac{2\nu_t}{Sc_t}\right)\left(\frac{\partial \overline{Y}}{\partial r}\right)^2 \tag{40}$$

where ν_t and Sc_t are the turbulent kinematic viscosity and Schmidt number, respectively, and the following form for the radial distribution of $\overline{Y}$,

$$\overline{Y} = \overline{Y}_m\left[1+\left(\frac{\gamma_t r}{4z}\right)^2\right], \tag{41}$$

where γ_t is a parameter chosen to fit the data, they deduced an expression for the axial and radial dependence of $\overline{\chi}$. In order to quantify their expression, Peters and Williams assumed $Sc_t = 1$, $\gamma_t = 10$, constant density flow, and self-similar mixing behavior. Everest et al.[109] and Feikema et al.[56] used the same approach, but incorporated the effects of an initial density difference to give

$$\overline{\chi} \propto U_o \frac{r_\epsilon^3}{z^4}\left(\frac{r}{z}\right)^2\left[1+25\left(\frac{r}{z}\right)^2\right]^{-6}. \tag{42}$$

r_ϵ is the effective radius given by Eq. (18). Eq.(18) has been shown to allow the mixing behavior of variable density jets to be correlated using the same relations as for self-similar constant-density flows.[4] Note that Eq. (42) requires that $\overline{\chi}$ be zero on the centerline (i.e., $r = 0$). Obviously, this can not be correct since it would require the centerline mass fraction to be constant, when it is known to fluctuate substantially. This discrepancy has been noted by Feikema et al.[56]

Dowling derived the centerline dependence of $\bar{\chi}$ using a slightly difference approach.[49] He started with an expression for $\bar{\chi}$ provided by Townsend,[146]

$$\bar{\chi} = \frac{(Y')^2(q^2)^{1/2}}{L_{jd}} , \tag{43}$$

where L_{jd} is full width of the jet defined earlier and q^2 is the kinetic energy of the turbulent fluctuations. By introducing the appropriate similarity relations for the jet, Dowling was able to show that

$$\bar{\chi}_m \propto \frac{U_o Y_o^2 r_o^3}{(z-z_o)^4} , \tag{44}$$

where Y_o is the mass fraction at the jet exit (normally one). Introducing the similarity expressions for variable density flows into Eq. (43) leads to Eq. (44) being rewritten as

$$\bar{\chi}_m \propto \frac{U_o Y_o^2 r_\epsilon^3}{(z-z_{oY})^2(z-z_{oJ})^2} , \tag{45}$$

where two different virtual origins are introduced to incorporate the experimental observation that the mass (z_{oY}) and momentum (z_{oJ}) distributions in axisymmetric jets can have different origins.[4] Note that if one assumes that $Y_o = 1$ and $z_{oY} = z_{oJ} = 0$, Eqs. (42) and (45) have the same dependencies on U_o, r_ϵ, and z. However, the latter equation predicts a nonzero value for $r/z = 0$.

In an attempt to test the applicability of Eq. (45), the following expression has been defined,

$$\beta_i = \frac{(\bar{\chi}_i)_m (z-z_o)^4}{8 U_o C_o^2 r_\epsilon^3} , \tag{46}$$

where i represents z and r for single component scalar dissipation measurements along the axial and radial directions, respectively, and p for measurements in the z-r plane. The subscript m indicates a centerline value. Eq. (46) is similar to the scaling developed by Friehe et al. for the mean centerline energy dissipation in axisymmetric jets.[78]

Table 4 lists values of $\bar{\chi}_i$ and β_i observed in the current work along with findings from other investigators. In many cases the literature values included in Table 4 have been obtained from results provided in different forms using appropriate transformations. For instance, for the heated jets it has been assumed that heated air behaves as a passive scalar, and results provided as derivatives of temperature have been transformed to conserved scalar form.

Table 4. Experimental $\bar{\chi}_i$ and β_i from literature measurements and the current work are summarized.

Authors	Year	Jet/Ambient	R_p	Re	z/r_o	i	$\chi_{i(s^{-1})}$	β_i
Lockwood and Moneib[43]	1980	heated air/air	0.53	52,300	40	z	0.00052	0.031
					50	z	0.00051	0.073
					60	z	0.00049	0.15
					70	z	0.00042	0.23
					80	z	0.00041	0.38
					90	z	0.00044	0.66
					100	z	0.00044	1.01
Dibble et al.[44]	1984	propane/air	1.52	134,000	100	r	0.067	10.6
Effelsberg and Peters[45]	1988	propane/air	1.52	7,500	40	r	0.28	6.5
					60	r	0.21	25
					80	r	0.14	55
					100	r	0.14	127
Namazian et al.[46]	1988	methane/air	0.55	7,000	34	z	0.26	13
						r	0.26	13
Dowling[49]	1991	ethylene/N_2	1.0	5,000	40	z	0.011	16.2
					80	z	0.0011	18.1
					120	z	0.00024	18.6
					160	z	.000085	19.7
		propylene/air	1.05	16,000	60	z	0.069	13.0
					180	z	0.00098	16.3
		propylene/air	1.05	40,000	120	z	0.013	18.9
Feikema and Driscoll[48]	1992	propane/air	1.52	10,000	28	p	1.4	6.5
Antonia and Mi[50]	1993	heated air/air	0.90	19,000	60	z	0.0019	4.2
						r	0.0019	4.2
Feikema et al.[56]	1996	propane/air	1.52	10,000	28	p	4.9	15.1
Current Work	-	propane/air	1.52	3,960	40	z	0.031	5.9
						r	0.033	6.3
						p	0.064	12.1

Examination of Table 4 shows that, with the exception of two sets of data, the use of Eq. (46) leads to a narrow range of values for β_z, β_r, and β_p. The two exceptions are measurements reported by Lockwood and Moneib[43] and Effelsberg and Peters[45] which yield values of β_z and β_r varying over wide ranges and have magnitudes which differ significantly from the remaining results. These two studies have the common characteristic that the separation of the locations used for the scalar derivative single-component measurements are much greater than the expected Batchelor scales for the corresponding flows. A lack of spatial resolution is the likely reason why the values of these two studies are so out of line with the remaining results.

Simple averaging of the remaining values yields $\beta_z = 14.4 \pm 5.2$ (10), $\beta_r = 8.5 \pm 3.5$ (4), and $\beta_p = 11.2 \pm 5.4$ (3) where the error limits are rms values and the values in parenthesis are the number of measurements. Given the wide range of values for $\bar{\chi}_i$ and experimental conditions represented in Table 4, it is clear that Eq. (46) effectively collapses the experimental findings. However, it is also clear that there is some uncertainty in the numerical values which should be assigned to the various β_i. For instance, values of β_z and β_r for centerline measurements should be very similar (see ahead) and the value of β_p should be larger by roughly a factor of two than either of the single-component results. The observed variations in values of β_i are most likely associated with the measurement difficulties discussed above as well as the neglect of virtual origins. Dowling has provided an excellent discussion of possible reasons for such variations.[49] Until additional measurements of scalar dissipation become available, it is probably most appropriate to assume that values of β_z and β_r are on the order of 8 and β_p is roughly a factor of two larger, but to recognize that there is an uncertainty of at least a factor of two associated with each of these recommendations. Based on these estimates, the corresponding value for $\bar{\chi}$, β, is on the order of 24.

Everest et al.[109] have provided a similar analysis of earlier experimental data based on the use of Eq. (42) by comparing the maximum values of estimated $\bar{\chi}$ along the radial direction at given downstream distances for a limited number of experimental measurements as well as the modeling results reported by Peters and Williams[42]. They also found a reasonable collapse of experimental data to a single value (8900 to 10,300) for values of maximum $\bar{\chi}$ covering a range of roughly fifty. Some caution should be exercised since the number of measurements considered was limited and included a result from Effelsburg and Peters[45] which has been identified as being in error due to insufficient spatial resolution. The statistical difficulties associated with measurements of large-value $\bar{\chi}$ have also been discussed.

Most previous measurements of scalar dissipation have been characterized in terms of averages of linear values. As has been shown, a log-normal representation seems to be more appropriate. In

Table 5. Experimental values of average and rms values for centerline log-normal pdfs of χ and γ from literature measurements and the current work are summarized.

Authors	Jet/Ambient	R_ρ	Re	z/r_o	$\overline{\log(\chi)}$	$\log(\chi)'$	γ
Namazian et al.[46]	methane/air	0.55	7,000	34	-0.74	0.35	9.6
Dowling[49]	ethylene/N_2	1.0	5,000	160	-4.35	0.88	10.3
Current Work	propane/air	1.52	3,960	40	-1.472	0.69	6.4

addition to the measurements reported here, the only other results reported in log terms which have been identified are due to Namazian et al.[46] and Dahm and Buch[79]. The latter used their mathematical analysis to estimate the log-normal distribution from one-dimensional data reported by Dowling and Dimotakis.[125,126] Table 5 summarizes averages and standard deviations determined from $\log(\chi)$ pdfs. In order to compare average results for different jet conditions, an equation analogous to Eq. (46),

$$\gamma = \frac{10^{\overline{\log(\chi)}}(z-z_o)^4}{8U_oC_o^2r_\epsilon^3}, \tag{47}$$

is used. Values of γ are sumarized in Table 5.

It is clear from Table 5 that Eq. (47) does a good job of collapsing the measurements of $\overline{\log(\chi)}$ as the three values result in an average of 8.8 ± 1.7, while the values of $10^{\overline{\log(\chi)}}$ vary from 4.5×10^{-5} to 0.18. Despite the strong dependence on downstream distance evident in Eq. (47), measurements by both Namazian et al.[46] and Dowling and Dimotakis[125,126] indicate that the rms values are roughly independent of downstream distance. While the rms values for the $\log(\chi)$ distributions included in Table 5 are of the same order of magnitude, the differences between the various investigations are too large to conclude with certainty that they represent a constant value. Additional work is necessary to determine whether the width of the log-normal distributions for $\log(\chi)$ depends on flow parameters such as the Reynolds number.

Average values for the axial and radial components of the centerline scalar dissipation determined in the current investigation are equal within experimental uncertainty in both linear (Table 4) and log (Table 3) terms. Namazian et al. also found that centerline axial and radial components in a methane jet at $z/r_o = 34$ were nearly equal.[46] Antonia and Mi measured all three components of the average centerline temperature gradient in a heated jet and found that they were identical within experimental uncertainty.[50] These authors discussed the question of centerline isotropy for scalar dissipation in detail and concluded that the behavior is indeed isotropic. Additional analysis led to the

same conclusion.[52,58] It should be noted that while the findings of these three studies are in agreement, the earlier measurements of Lockwood and Moneib indicated that the radial component was roughly twice as large as the axial component.[43] It seems likely that this disagreement is due to the limited spatial resolution of these early measurements as discussed above.

While average values for the single components indicate that the scalar dissipation is isotropically distributed, the measured pdf for the angle of the centerline concentration gradient shown in Fig. 38 indicates that this is not the case. Orientations with the gradients pointing in the radial direction are found to be most probable, while gradients lying along the jet centerline are twice as likely to point downstream as upstream.

The scalar dissipation measurements suggest that the anisotropy increases as the measurement position is moved away from the jet centerline. At first, values of $\overline{\log(\chi_r)}$ increase with radial distance before dropping further from the centerline. On the other hand, values of $\overline{\log(\chi_z)}$ drop continuously as the measurement position moves outward. Values of the rms for both components are relatively constant near the jet centerline before increasing substantially near the edge of the jet. The effects of the different radial behaviors for the axial and radial components seem to cancel as the radial average and rms values for $\log(\chi_p)$ are roughly constant for $-4 \le r/r_o \le 4$ (see Figs. 34 and 35). At larger radial distances the average begins to fall off rapidly, while the rms first increases to a sharp peak before decreasing rapidly at still larger r.

Detailed quantitative comparisons with previous findings are not justified due to the use of Taylor's hypothesis to determine the axial component of χ_p, but qualitative comparisons of the radial dependence should be valid. All of the studies in Table 4 include some measurements of χ or one or more of its components as a function of radial position.

Lockwood and Moneib found that values of $\overline{\chi}_r$ first increased with radial position and then fell off rapidly for $|r|/(r_{1/2})_c$ greater than ≈ 1.4.[43] Strangely, even though the centerline values were roughly constant for both $z/r_o = 40$ and 60, the increase in $\overline{\chi}_r$ with radial distance was much greater for the position nearer the nozzle. Dibble et al. found that estimated values of $\overline{\chi}$ first increased and then fell very rapidly (i.e., much faster than $\overline{Y}$) towards zero with increasing $|r|$.[44] Effelsberg and Peters reported that $\overline{\log(\chi)}$ values increased with $|r|$ and were roughly equal for $z/r_o = 60$ and 100, while values for the rms remained roughly constant.[45] Note that each of these early studies reported different radial dependencies.

Namazian et al. reported measurements of $\overline{\log(\chi)}$ as a function of downstream distance for both the jet centerline and along the contour $(r_{1/2})_c$ from near the jet exit to $z/r_o = 34$.[46] For the current jet $(r_{1/2})_c$ is expected to be at $|r| = 14.4$ mm $= 4.5r_o$ assuming $z_o = 0$ mm and $(r_{1/2})_c = 0.113z$.[4]

Namazian et al.'s results indicate that $\overline{\log(\chi)}$ values at both positions have a similar dependence on z, but that values at $(r_{1/2})_c$ are somewhat less than for $r = 0$. The rms values were roughly constant at 0.35 for both positions. Radial profiles at $z/r_o = 26$ showed that $\overline{\log(\chi)}$ decreased at an increasing rate with $|r|$, while the rms remained nearly constant until $|r|/(r_{1/2})_c \approx 1$ and then decreased rapidly toward the jet edge.

Dowling reported that values for his estimated $\bar{\chi}$ were nearly independent of r for $|r|/z$ values out to 0.2.[49] The radial extent over which constant values of $\bar{\chi}$ were observed is somewhat greater than indicated by the current measurements, but it must be kept in mind that Dowling employed Taylor's hypothesis and used the centerline velocity to normalize all of his measurements. Fiekema and Driscol found that their two-dimensional measurements of $\bar{\chi}_p$ increased slightly as the measurement position moved off the centerline and then decreased steadily for $|r|/(r_{1/2})_c > 0.7$.[48] The same behavior was observed for the later measurements reported by this group.[56]

Antonia and Mi found that values of $\bar{\chi}_z$ were slightly smaller than for $\bar{\chi}_r$ for positions away from the jet centerline.[50] The radial component first remained nearly constant as the measurement position was moved away from the centerline, and then began to drop at larger radial distances. Averages for both components fell more rapidly for $|r|/(r_{1/2})_c > 0.7$. They emphasized that both components had nearly equal values for a given radial location, indicating that scalar dissipation is nearly isotropic across much of the jet. However, analysis presented in a later paper showed that the ratio of averages for the radial and axial components increases with radial distance, thus indicating an increase in the degree of anisotropy.[52] Note that their measurements did not extend far enough radially to capture the strong isotropy evident between the axial and radial components when comparing the jet's outer edges in images in Figs. 12 and 13 with those in Figs. 22 and 23.

The more recently published results agree with the current measurements that the degree of anistropy in χ increases with radial distance. At the same time, $\bar{\chi}$ and $\overline{\log(\chi)}$ values change slowly near the jet centerline and then fall off rapidly with radial distance as the jet becomes intermittent. The rms behavior in all of the more recent studies shows a relatively constant region for locations in the central core of the jet. The current investigation seems to be the only one which has recognized the increase in rms values and anisotropy at the jet's outer edge.

As was true for measurements on the jet centerline, pdfs of Θ for $r \neq 0$ suggest that the orientation of the scalar dissipation is far from isotropic. Particularly noteworthy is the strong anisotrophy in Θ which develops as soon as the measurement position is moved away from the centerline (see Fig. 38). The pdfs become highly asymmetric for radial distance as small as $|r|/r_o = 0.12$, which corresponds to $|r|/z = 0.003$. Gradients lying along the radial direction and pointing

towards the centerline are strongly favored. These results indicate that even though axial and radial components of χ have very similar average and rms values in the core region of the jet, their spatial orientations are anisotropic. At the jet's outer edge the anisotrophy is enhanced (see Figs. 37 and 39) due to the unique structure associated with ELSOSs.

C. Evidence for Interactions Between Large-Scale and Small-Scale Structures

The availability of real-time line measurements allows details concerning interactions between small scales where scalar dissipation is strong and larger scales in the flow field to be identified which apparently have not been discussed previously for axisymmetric jets. While the experimental findings are insufficient to definitely determine the underlying physical mechanisms responsible for these observations, recent experimental and modeling work allows plausible explanations to be suggested. Throughout the previous discussion a clear distinction has been drawn between the scalar behavior at the edge of the jet and positions closer to the centerline (i.e., the jet core region) where the flow is not intermittent. This distinction will be maintained for the discussion which follows.

Consider first the behavior of the scalar dissipation at the outer edges of the ELSOSs. Images of the mass fraction (Figs. 7 and 8), scalar dissipation (Figs. 12, 13, 22, 23, 30, and 31), and Θ (Fig. 39) in this region of the flow indicate that there is a great deal of large-scale organization of the scalar structure. It has already been pointed out that the strong ramp-like structures on the downstream edges and the smaller magnitudes for the mass fraction gradients on the upstream sides of these structures are consistent with the hypothesis that this distinctive behavior results from the ejection of LSTSs (i.e., ELSOSs) at an angle of roughly 45° to the downstream direction. Note that the DNS studies described in the Introduction would not be expected to identify the ELSOSs where the mixing is largely determined by strong stretching over large distances (the downstream edges) or in the interiors where there is evidence for mixing by stirring processes since these calculations are not currently capable of handling the wide range of turbulent scales required. For interior locations of ELSOSs which have sufficient velocity (i.e, a sufficiently high local Reynolds number) for a well defined turbulent cascade to develop, small-scale mixing is likely to occur. The earlier discussion indicates that such regions do exist within ELSOSs. These findings alone are sufficient to reach the conclusion that small-scale mixing behavior in certain regions of axisymmetric jets is intimately coupled with much larger scale processes. However, due to difficulties associated with identifying such regions, as well as uncertainties concerning the nature of the larger vortical structures which are present, further discussion will be limited to results for the core region of the jet.

The evidence indicating a break down of Kolmogorov's hypothesis of a universality for the small-scale structure in the core region of the current axisymmetric jet is overwhelming. This evidence includes 1) the distinct directionality evident in χ_z (see Figs. 22 and 23), 2) the presence of small-scale intermittency as reflected by the alternating regions of intense and relatively inactive small-scale mixing, 3) the tentative identification of internal ramp-like structures in the core region, and 4) the strong dependence of Θ on direction in the *r*-*z* plane, including its strong dependence on symmetry as indicated by the asymmetries which quickly develop as the sampling position is moved from the jet centerline (Fig. 38). Taken together, these findings indicate that the small-scale turbulent structure is not universal and that there is significant coupling between the small turbulent structures and LSTSs in this flow.

Perhaps the clearest evidence is the distinct layer structure which is evident in images for χ_z, particularly Figs. 22 and Figs. 23b and 23c. Organization is apparent which results in roughly constant values of $\log(\chi_z)$ extending over substantial distances, primarily in the radial direction. At this point it is relevant to consider whether these structures might be the result of some type of artifact associated with the experimental system or data analysis. For instance, the individual pixels in the images are not square, but have relative sizes in the axial and radial directions of 1:4.1, assuming Taylor's Hypothesis for the axial direction. The resulting distortion of the images certainly enhances the impression of elongation in the radial direction, but it is clear that ratios for the lengths to the thicknesses of the majority of the layers evident in the figures are much greater than four and that the layering must be, in fact, a characteristic of the flow field. Furthermore, the effective spatial resolution for both directions is roughly comparable (see Table 2) and should not be responsible for the observations.

The layered regions are most evident for higher values of χ_z and become nearly indistinguishable for the smallest values. A remarkable characteristic of these structures is that they are much more difficult to identify in the corresponding images of χ_r (see Fig. 12 and Figs. 13b and 13c). Close inspection of images for the mass fraction and the two components of scalar dissipation, e.g., Figs. 7, 12, and 22, provides an explanation for this observation and a strong clue as to the physical structure of the organization within the mass fraction field which is responsible. The mass fraction image clearly shows variations which are layered, with the layers extending principally in the radial direction. Detailed comparisons show that while the layers clearly extend in the radial direction, they are not entirely "smooth". In fact, there are distinct temporal and spatial small-scale variations along the edges, which, when differentiated, lead to large fluctuations in χ_r, but to only minor time offsets in the corresponding values of χ_z. It is significant that similar differences in the components for

χ can be observed in the results of direct numerical simulations of turbulent flows in the presence of a scalar gradient (e.g., see Fig. 10 in reference 90).

The above discussion suggests that the distinctive differences in the appearances of the radial and axial components of scalar dissipation images result from the presence of numerous sheet-like structures in the concentration field which have their faces aligned predominantly along the axial direction. Instead of being perfectly flat, the sheets are mildly crumbled.

As discussed in the Introduction, two possible mechanisms for the formation of scalar sheets in turbulent flows have been proposed in the literature. The first results from the direct interaction of organized LSTSs. In the notation of this work these are expected to be JCLSOSs. Previous experimental[147] and direct numerical simulations[89,90] have suggested that widely spaced sheet-like scalar structures should be observed at the edges (cliffs) of the large-scale internal ramp-like structures which develop in turbulent flows. The large concentration changes across the sheets result from the localized concentration of a much smaller time-averaged scalar gradient by stretching at the stagnation point formed by the intersection of the two large-scale organized vortical structures. The type of flow at the stagnation point is referred to as hyperbolic, and the sheet-like scalar structure forms very near the diverging separatrix in the vicinity of the stagnation point. In this view, most of the regions of the velocity field are elliptic (i.e., have closed streamlines) which tend to expel the time-averaged gradient to the edges of the structure where it is concentrated. It is the combined effect of the elliptic and hyperbolic flow regions which is believed to generate internal ramp-like structures.

The discussion above provides an explanation for the formation of strong concentration gradients corresponding to scalar concentration changes on the order of the rms for the scalar fluctuations. However, these regions are expected to be spaced at distances roughly corresponding to the size of the large-scale structures. As discussed above, there is compelling, but inconclusive, evidence for the presence of such structures in the current study.

On the other hand, Buch and Dahm have shown that the entire scalar field is organized into sheet-like structures, but have argued that for high enough Reynolds number these sheets should be randomly oriented in space.[38,47,57,59] In the current study the sheets seem to be strongly oriented in the radial direction with their faces aligned toward the downstream direction. The layers are closely packed together and occur at a much higher frequency than would be expected if they were due to the formation of cliffs resulting from internal ramp-like structures forming between individual JCLSOSs. The most likely mechanism for the development of the layered structure, based on current understanding, is the concentration of scalar gradients associated with the presence of vortex tubes in the flow field as discussed in the Introduction.[99,100,101]

If the above conclusion is correct, it has important implications for the organization of the velocity field within the core region of an axisymmetric jet. Based on DNS findings summarized in the Introduction, the vortex tubes responsible for the layering of the scalar must lie predominantly in the radial direction. The resulting picture is that of roughly parallel vortex "rollers" aligned in the radial direction. Furthermore, if the hypothesis of Rogers and Moin[100] is correct, it is likely that the vortex tubes are formed at an angle of roughly 45° to the z axis, and are then rotated to orientations lying primarily in the radial direction by the mean shear field of the jet. Rogers and Moin indicated that the degree of alignment of the vortex tubes increased with the strength of the vorticity concentrations. This conclusion is consistent with the experimental observation that regions of larger scalar dissipation values are more clearly organized than those having smaller scalar dissipation and provides additional support that the observed scalar-field organization is the result of the concentration of vorticity into tube-like structures aligned primarily in the radial direction with lengths which are considerably longer than the local Kolmogorov scale. Such a conclusion is clear evidence for a break-down of Kolmogorov's hypothesis and suggests that there is a direct coupling of large-scale vortical structures in the flow with the smallest scales which are responsible for dissipation of turbulent energy and scalar gradients.

The above hypothesis concerning the structure of the flow field provides an explanation for the strong dependence of the scalar gradient angle on spatial orientation which is evident in Fig. 38. On average, the mean shear rate in the radial direction at the jet centerline should be zero, and vortex tubes passing through this area should not be rotated by the mean flow. This explains the symmetry evident for Θ at the jet centerline. As soon as the measurement position is moved from the centerline, the vortex tubes are subjected to a mean velocity field which tends to rotate them towards the radial direction. Since the scalar sheets associated with the tubes will also be rotated, it is to be expected that the gradient angles will become asymmetric with directions pointing toward the centerline being favored. This behavior is evident in the pdfs for Θ recorded at $r/r_o = \pm 0.12$ in Fig. 38.

Two expected effects of direct interactions between large- and small-scale turbulent structures, small-scale anisotropy based on average values for the components of scalar dissipation and extended wings for pdfs of scalar dissipation, are not evident in the current results. On the jet centerline values of $\overline{\chi}_r$ and $\overline{\chi}_z$ are found to be identical within the experimental uncertainty. This finding agrees with others reports in the literature for axisymmetric jets.[46,50] Equal values for averaged components of scalar dissipation have often been used as a test for small-scale isotropy. Since the evidence for small-scale anisotropy now appears overwhelming for axisymmetric jets, it must be concluded that time-averaged measurements alone are not an adequate test. It should be mentioned that measurements in

another type of shear flow, namely a planar jet, yielded average values for scalar dissipation components which were different and were taken as an indication for the breakdown of isotropy.[148] It seems likely that anisotropic small-scale scalar structures are a general characteristic of turbulent shear flows.

Some of the numerous experimental and modeling investigations suggesting that the tails of χ pdfs fall off more slowly than would be expected for a lognormal distribution of scalar dissipation have been discussed in the Introduction. However, earlier investigations in axisymmetric jets have provided no evidence for such a behavior. Holzer and Siggia[89] explicitly addressed this point by noting that they did not "feel that the published experimental fits[79] to lognormal behavior are definite nor preclude a stretched-exponential form." The current results for single and planar components are fit very well by assuming that the pdf for χ is lognormal. The only indication of a poor fit is for high values of χ_r and χ_z where the fall off is faster than expected. While it is possible that the current data are insufficiently resolved to identify a non Gaussian behavior, we are forced to conclude for the moment that the pdfs are indeed lognormal for these low Re axisymmetric jets and that further theoretical work is required in order to develop a full understanding of the shapes of χ pdfs in turbulent shear flows.

The final point to be addressed is the small-scale intermittency evident for the scalar dissipation in the core regions of the jet. The implications of the above discussion is that this intermittency results from large-scale (on the order of size of the largest scales in the flow) variations in the strengths of the vortex tubes generated by the flow. Whatever the mechanism responsible, it is clear that the net result is that the local structure of the smallest scales is intimately coupled with the behavior of the largest scale structures present in the flow field.

Taken together, the experimental evidence strongly supports the conclusion that there are significant interactions between large- and small-scale turbulent structures in the core region of axisymmetric jets. Furthermore, the behavior of the scalar mixing at the smallest scales reveals the presence of JCLSOSs in this region of the flow. The current findings agree with the conclusions of Sreenivasan as discussed in his 1991 review (see the list in the Introduction).[84] These interactions provide a mechanism for the failure of Kolmogorov's hypothesis.[80]

V. SUMMARY AND FINAL COMMENTS

The work reported here has covered a number of topics dealing with mixing in axisymmetric jets. The experimental findings and critical analysis of related literature have allowed a number of conclusions concerning mixing behavior in these flows. In this section the major findings and conclusions are grouped and listed under four headings: A) Experiment and Analysis, B) Large-Scale

Turbulent Structures, C) Scalar Dissipation Characteristics, and D) Interactions Between Small- and Large-Scale Turbulent Structures.

A. Experiment and Analysis

1. An intensified, real-time line camera has been developed which has sufficient spatial and temporal resolution and sensitivity for accurate measurements of concentration in a relatively low Reynolds number axisymmetric jet of propane flowing into air. The dynamic range is on the order of 500:1.
2. Two-dimensional wavelet analysis provides an excellent means for smoothing the high frequency variations in the time-space concentration data which results from a limited number of possible values during the experimental digitization process. The success of this approach is demonstrated by the excellent quality of the pdfs determined for the various components of scalar dissipation.
3. The experimental spatial resolution required to fully resolve scalar dissipation variations in turbulent flows is on the order of the Batchelor scale, η_B. The coefficient does not exceed a value of 2. Literature recommendations[37,38,47,67,68,71] suggesting spatial resolution requirements can be relaxed substantially should not be adopted for quantitative measurements.
4. Eq. (19) provides an accurate estimate for η_B using values of $(r_{1/2})_u$, U_m', ν, and Sc. Estimates can also be obtained using Eqs. (7) and (8) along with the centerline estimate for $\bar{\epsilon}$ (see Eq. (12)) given by Friehe et al.[78]
5. Measurements of scalar dissipation components along a single spatial direction or in a plane are subject to geometric effects which distort the pdfs for log values and preclude simple addition of components to obtain average and rms values for χ. Approaches based on the assumption of an isotropic distribution for χ developed by Buch and Dahm allow accurate pdfs for χ to be obtained from lower dimensional results.[47,79]

B. Large-Scale Turbulent Structures

1. Three distinct types of possible organized large-scale turbulent structures for axisymmetric jets are described: 1) ejected large-scale organized structures (ELSOSs), 2) full jet large-scale organized structures (FJLSOSs), and 3) jet column large-scale organized structures (JCLSOSs).

2. It is demonstrated, based on the current results and previous experimental findings, that LSTSs observed at the outer edge of an axisymmetric jet are the result of relatively localized, short-lived ejections of fluid from the jet core. These structures are those referred to as ELSOSs.
3. ELSOSs can be usefully viewed as impulsively started flows which move outward from the jet center and are distorted by the strain rates associated with the overall shear flow. This simple model provides an explanation for the ramp-like structures observed in time records of mixture fraction in the intermittency regions of these flows, as well as the presence of two distinct types of mixing--stirring and small-scale turbulence.
4. Smaller, more localized ejections of jet fluid are observed along the downstream edges of ELSOSs.
5. EJLSOSs do occasionally expend their turbulent energy and leave nonturbulent mixtures of jet fluid at the outer edge of the jet. These pockets are subsequently retrained into the jet as the result of the passage of later LSTSs.
6. The conclusion that the intermittency region of an axisymmetric jet is dominated by ELSOSs argues against the existence of FJLSOSs of the type shown as idealized drawings by Dahm and Dimotakis[19] and Mungal and O'Neil[30].
7. The arguments against the existence of FJLSOSs do not rule out the coexistence of a large-scale organized structure within the core region of the jet where the intermittency factor is one for gas jets. Tso and Hussain have described explicitly the existence of two types of LSTSs in axisymmetric jets.[16] These authors found that the structures educed in the core region, here referred to as JCLSOSs, had either axisymmetric, helical, or double helical configuration, with the helical configuration strongly favored.
8. Much of the experimental evidence provided in the literature to justify the existence of FJLSOSs can be interpreted equally well, and in some cases more consistently, as being due to JCLSOSs which coexist with ELSOSs. This is particularly true with regard to the fluctuations in "flame" length" observed for a variety of reacting turbulent jets.[19,29,30,32] A major exception is the series of experiments which suggests that LSTSs form near the base of the jet and can be subsequently tracked over large distances.[29,30,32,33,34] We have been unable to provide a plausible explanation for these observations in terms of the coexistence of localized EJLSOSs and JCLSOSs.
9. The current experimental findings provide additional evidence for some degree of large-scale organization in the core region of axisymmetric jets. Distinct alternating regions of intense and more modest fluctuations observed in scalar dissipation time-space images are likely

associated with such an underlying structure. Pdfs for the angle of the mass fraction gradient relative to the jet centerline indicate the presence of an internal ramp-like structure which has previously been attributed to LSTSs.

10. The experimental results suggest that there are widely spaced regions where discontinuous narrow bands of particularly high values of χ extend across significant radial distances in the core region. These regions are much less distinctive than in an axisymmetric water jet where they have been associated with the occurrence of organized FJSLOSs.[23]

C. Scalar Dissipation Characteristics

1. Pdfs for $\log(\chi)$ on the jet centerline can be approximated quite well as having Gaussian shapes.
2. Average centerline axial and radial components of χ are equal within experimental uncertainty. This agrees with previous experimental findings and has led to the conclusion that scalar dissipation is isotropic on the jet centerline.
3. Values of $\overline{\chi}_r$ and $\overline{\chi}_z$ begin to differ by increasing amounts as the measurement position is moved away from the centerline. At the outer edge of the jet, these differences are clearly associated with the characteristic shape of the LSTSs observed in the intermittency region.
4. Centerline values for the averages of $\log(\chi_r)$, $\log(\chi_z)$, and $\log(\chi_p)$ from a large number of experiments having a wide range of conditions are effectively collapsed by the use of Eq. (46). The best estimates for the constants to use in Eq. (46) are $\beta_r = \beta_z = 8$ and $\beta_p = 16$. The corresponding value for χ is $\beta = 24$.
5. Average and rms values for χ and its components are very sensitive to the highest values in the distribution. This requires recording a large number of fully resolved measurements in order to determine these values accurately. For the current measurements, it was shown that the high-value tails of the pdfs for χ_r, χ_z, and χ_p are cut off as compared to the expected distributions obtained by transforming the corresponding pdfs for the log values. It is unclear if this is the result of experimental resolution limitations, or if the high-end tail of the roughly log-normal distribution for χ is actually truncated.
6. Despite uncertainties associated with the measurement of high values of χ, Eq. (47) effectively correlates a number of experimental measurements from different groups of $\overline{\chi}$ along the jet centerline, yielding a value of 8.8 for γ.

D. Interactions Between Small- and Large-Scale Turbulent Structures

1. Scalar dissipation behavior at the outer edge of an axisymmetric jet is clearly tied to the presence of ELSOSs in this region of the flow. Narrow laminar-like region of high χ extend across the downstream edges of these structures. Even though these are regions of intense molecular mixing, strong concentration gradients are maintained for significant periods of time.
2. There is strong evidence for two different types of mixing within the LSTSs found in the intermittency region of the jet. This evidence includes the appearance of images for mass fraction and scalar dissipation presented here, as well earlier analyses [134,136] available in the literature. One type is turbulent mixing resulting from a classical turbulent cascade from large to small scales. The second is characterized as "stirring" and results from the passage of organized LSTSs.
3. A dominant feature of the core region of the jet is the presence of regions of relatively constant χ which have an anisotropic shape, being elongated primarily in the radial direction.
4. There is a distinct clumping of regions of intense and moderate molecular mixing, as reflected by local variations of χ, which is evident in space-time images for χ_r, χ_z, and χ_p. This behavior is in addition to the small-scale intermittency which is well known for these flows.
5. Pdfs for the angle of mass fraction gradient in the radial-axial plane indicate that the local mixing structure throughout the jet is anisotropic. On the centerline, the most probable direction for gradients lying along the centerline is downstream, which is the opposite of the direction for the time-averaged gradient. This indicates the presence of an underlying ramp-like structure in the core region.
6. As the measurement position is moved away from the jet centerline, pdfs for the gradient angle rapidly become anisotropic, with gradients pointing toward the jet centerline becoming more probable.
7. Organization of the mixing field in axisymmetric jets can be understood by observations from idealized DNS studies. The narrow bands of high χ which extend across the radial direction of the jet core are attributed to the formation of a cliff-like concentration structure which forms in the vicinity of a stagnation point lying at the interface of two adjacent large-scale vortical structures. The more numerous radially elongated regions of χ are associated with the presence of vortex tubes which tend to concentrate concentration gradients. The preferred

orientation for the tubes is due to the presence of the time-averaged strain associated with the shear flow.

8. The evidence for a direct coupling of the small- and large-scale structures in this type of flow indicates a breakdown in Kolmogorov's hypotheses.
9. The current measurements of χ have pdfs which are fit very well by assuming they have a log-normal distribution. There is no evidence of the long exponential tails found in some other types of flows and in DNS studies.

E. Final Comments

The study of turbulent flow and mixing has been an intense area of study for many years. Such interest is justified due to the central importance of turbulence in a wide range of practical applications. This work has addressed a number of questions of current interest to researchers in the field. It is our hope that this work will serve as a catalyst for the development of the improved understanding of turbulent structure and mixing which are required for the development of models for predicting these complicated behaviors in practical systems.

VI. REFERENCES

1. S. Corrsin, "Investigation of flow in an axially symmetrical heated jet of air," *N.A.C.A. Wartime Report W-94*, 1943.
2. S. Corrsin and A. L. Kistler, "Free-stream boundaries of turbulent flows," *N.A.C.A. Report 1244*, 1955.
3. W. M. Pitts and T. Kashiwagi, "The application of laser-induced Rayleigh light scattering to the study of turbulent mixing," *J. Fluid Mech.* **141**, 391 (1984).
4. C. D. Richards and W. M. Pitts, "Global density effects on the self-preservation behavior of turbulent free jets," *J. Fluid Mech.* **254**, 417 (1993).
5. C. J. Chen and W. Rodi, *Vertical Turbulent Buoyant Jets--A Review of Experimental Data* (Pergamon, New York, 1980).
6. S.C. Crow and F. H. Champagne, "Orderly structure in jet turbulence," *J. Fluid Mech.* **48**, 547 (1971).
7. G. L. Brown and A. Roshko, "On density effects and large structure in turbulent mixing layers," *J. Fluid Mech.* **64**, 775 (1974).
8. L. S. G. Kovasznay, V. Ribens, and R. F. Blackwelder, "Large-scale motion in the intermittent region of a turbulent boundary layer," *J. Fluid Mech.* **41**, 283 (1971).
9. R. A. Antonia, A. Prabhu, and S. E. Stephenson, "Conditionally sampled measurements in a heated turbulent jet," *J. Fluid Mech.* **72**, 455 (1975).
10. R. Chevray and N. K. Tutu, "Intermittency and preferential transport of heat in a round jet," *J. Fluid Mech.* **88**, 133 (1978).
11. R. Chevray, "Entrainment interface in free turbulent shear flows," *Prog. Energy Combust. Sci.* **8**, 303 (1982).

12. K. R. Sreenivasan, R. A. Antonia, and D. Britz, "Local isotropy and large structures in a heated turbulent jet," *J. Fluid Mech.* **94**, 745 (1979).
13. K. R. Sreenivasan and R. A. Antonia, "Joint probability densities and quadrant contributions in a heated turbulent round jet," *AIAA J.* **16**, 867 (1978).
14. S. Komori and H. Ueda, "The large-scale coherent structure in the intermittent region of the self-preserving round free jet," *J. Fluid Mech.* **152**, 337 (1985).
15. J. Tso, L. S. G. Kovasznay, and A. K. M. F. Hussain, "Search for large-scale coherent structures in the nearly self-preserving region of a turbulent axisymmetric jet," *J. Fluid Eng.* **103**, 503 (1981).
16. J. Tso and F. Hussain, "Organized motions in a fully developed turbulent axisymmetric jet," *J. Fluid Mech.* **203**, 425 (1989).
17. P. E. Dimotakis, R. C. Miake-Lye, and D. A. Papantoniou, "Structure and dynamics of round turbulent jets," *Phys. Fluids* **26**, 3185 (1983).
18. C. H. Gibson, C. A. Friehe, and S. O. McConnel, "Structure of sheared turbulent fields," Phys. Fluids, **20**, S156 (1977).
19. W. J. A. Dahm and P. E. Dimotakis, "Measurements of entrainment and mixing in turbulent jets," *AIAA J.* **25**, 1216 (1987).
20. H. C. Hottel, "Burning in laminar and turbulent fuel jets," in *Fourth Symposium (International) on Combustion* (William and Wilkins, Baltimore, 1953), p. 97.
21. W. J. A. Dahm and P. E. Dimotakis, "Mixing at large Schmidt number in the self-similar far field of turbulent jets," *J. Fluid Mech.* **217**, 299 (1990).
22. D. J. Shlien, "Observation of dispersion of entrained fluid in the self-preserving region of a turbulent jet," *J. Fluid Mech.* **183**, 163 (1987).
23. D. Papantoniou and E. J. List, "Large-scale structure in the far field of buoyant jets," *J. Fluid Mech.* **209**, 151 (1989).
24. W. M. Pitts, "Large-scale turbulent structures and the stabilization of lifted turbulent jet diffusion flames," in *Twenty-Third International Symposium on Combustion* (The Combustion Institute, Pittsburgh, 1990), p. 661.
25. W. M. Pitts, "Assessment of theories for the behavior and blowout of lifted turbulent jet diffusion flames," in *Twenty-Second Symposium (International) on Combustion* (The Combustion Institute, Pittsburgh, 1988), p. 809.
26. W. M. Pitts, "Importance of isothermal mixing processes to the understanding of lift-off of turbulent jet diffusion flames," *Combust. Flame* **76**, 197 (1989).
27. I. van Cruyningen, A. Lozano, and R. K. Hanson, "Quantitative imaging of concentration by planar laser-induced fluorescence," *Expts. Fluids* **10**, 41 (1990).
28. R. W. Schefer, A. R. Kerstein, M. Namazian, and J. Kelly, "Role of large-scale structure in a nonreacting turbulent CH_4 jet," *Phys. Fluids* **6**, 652 (1994).
29. M. G. Mungal and D. K. Hollingsworth, "Organized motion in a very high Reynolds number jet," *Phys. Fluids A* **1**, 1615 (1989).
30. M. G. Mungal and J. M. O'Neil, "Visual observations of a turbulent diffusion flame," *Combust. Flame* **78**, 377 (1989).
31. I. van Cruyningen, A. Lozano, M. G. Mungal, and R. K. Hanson, "Three-dimensional visualization of temporal flow sequences," *AIAA J.* **29**, 479 (1991).
32. M. G. Mungal, P. S. Karasso, and A. Lozano, "The visible structure of turbulent jet diffusion flames: large-scale organization and flame tip oscillation," *Combust. Sci. Tech.* **76**, 165 (1991).
33. M. G. Mungal, A. Lozano, and I. van Cruyningen, "Large-scale dynamics in high Reynolds number jets and jet flames," *Expts. Fluids* **12**, 141 (1992).

34. M. Yoda, L. Hesselink, and M. G. Mungal, "The evolution and nature of large-scale structures in the turbulent jet," *Phys. Fluids A* **4**, 803 (1992).
35. J. E. Broadwell and M. G. Mungal, "Large-scale structures and molecular mixing," *Phys. Fluids A* **5**, 1193 (1991).
36. M. Yoda, L. Hesselink, and M. G. Mungal, "Instantaneous three-dimensional concentration measurements in the self-similar region of a round high-Schmidt-number jet," *J. Fluid Mech.* **279**, 313 (1994).
37. W. J. A. Dahm, K. B. Southerland, and K. A. Buch, "Direct, high resolution, four-dimensional measurements of the fine scale structure of Sc » 1 molecular mixing in turbulent flows," *Phys. Fluids A* **3**, 1115 (1991).
38. K. A. Buch, Jr. and W. J. A. Dahm, "Experimental study of the fine-scale structure of conserved scalar mixing in turbulent shear flows. Part I. Sc » 1," *J. Fluid Mech.* **317**, 21 (1996).
39. N. Peters, "Laminar flamelet concepts in turbulent combustion," in *Twenty-First Symposium (International) on Combustion* (The Combustion Institute, Pittsburgh, 1986), p. 1231.
40. R. W. Bilger, "The structure of turbulent nonpremixed flames," in *Twenty-Second Symposium (International) on Combustion* (The Combustion Institute, Pittsburgh, 1988), p. 475.
41. K. A. Buch, W. J. A. Dahm, R. W. Dibble, and R. S. Barlow, "Structure of equilibrium reaction rate fields in turbulent jet diffusion flames," in *Twenty-Fourth Symposium (International) on Combustion* (The Combustion Institute, Pittsburgh, 1992), p. 295.
42. N. Peters and F. A. Williams, "Liftoff characteristics of turbulent jet diffusion flames," *AIAA J.* **21**, 423 (1983).
43. F. C. Lockwood and H. A. Moneib, "Fluctuating temperature measurements in a heated round free jet," *Comb. Sci. Technol.* **22**, 63 (1980).
44. R. W. Dibble, W. Kolmann, and R. W. Schefer, "Measurements and predictions of scalar dissipation in turbulent jet flames," in *Twentieth Symposium (International) on Combustion* (The Combustion Institute, Pittsburgh, 1984), p. 345.
45. E. Effelsberg and N. Peters, "Scalar dissipation rates in turbulent jets and jet diffusion flames," in *Twenty-Second Symposium (International) on Combustion* (The Combustion Institute, Pittsburgh, 1988), p. 693.
46. M. Namazian, R. W. Schefer, and J. Kelly, "Scalar dissipation measurements in the developing region of a jet," *Combust. Flame* **74**, 147 (1988).
47. K. A. Buch and W. J. A. Dahm, *Fine Scale Structure of Conserved Scalar Mixing in Turbulent Shear Flows: Sc > > 1, Sc ≈ 1 and Implications for Reacting Flows*, The University of Michigan Report No. 026779-5 (1991).
48. D. A. Feikema and J. F. Driscoll, "Scalar dissipation rate measurements in initially non-premixed turbulent shear layers using Rayleigh imaging," *6th International Symposium on Applications of Laser Techniques to Fluid Mechanics*, Lisbon, Portugal, July 20-23, 1992.
49. D. R. Dowling, "The estimated scalar dissipation rate in gas-phase turbulent jets," *Phys. Fluids A* **3**, 2229 (1991). see also D. R. Dowling, "Erratum: the estimated scalar dissipation rate in gas-phase turbulent jets," *Phys. Fluids A* **4**, 453 (1992).
50. R. A. Antonia and J. Mi, "Temperature dissipation in a turbulent round jet," *J. Fluid Mech.* **250**, 531 (1993).
51. F. Anselmet, H. Djeridi, and L. Fulachier, "Joint statistics of a passive scalar and its dissipation in turbulent flows," *J. Fluid Mech.* **280**, 173 (1994).
52. J. Mi, R. A. Antonia, and F. Anselmet, "Joint statistics between temperature and its dissipation rate components in a round jet," *Phys. Fluids* **7**, 1665 (1995).
53. C. Tong and Z. Warhaft, "Passive scalar dispersion and mixing in a turbulent jet," *J. Fluid Mech.* **292**, 1 (1995).

54. J. A. Muss, R. W. Dibble, and L. Talbot, "A helium-hydrogen mixture for the measurement of mixture fraction and scalar gradient in non-premixed reacting flows," *AIAA 94-0612*, Thirty-Second Aerospace Sciences Meeting, Reno, NV, Jan. 10-13, 1994.
55. A. Brockhinke, P. Andresen, and K. Kohse-Höinghaus, "Contribution to the analysis of temporal and spatial structures near the lift-off region of a turbulent hydrogen diffusion flame," in *Twenty-Sixth Symposium (International) on Combustion* (The Combustion Institute, Pittsburgh, 1996), p. 153.
56. D. A. Feikema, D. Everest, and J. F. Driscol, "Images of dissipation layers to quantify mixing within a turbulent jet," *AIAA J.* **34**, 2531 (1996).
57. K. A. Buch and W. J. A. Dahm, "Experimental study of the fine-scale structure of conserved scalar mixing in turbulent shear flows. Part 2. Sc ≈ 1," *J. Fluid Mech.* **364**, 1 (1998).
58. J. Mi, R. A. Antonia, G. J. Nathan, and R. E. Luxton, "Non-Gaussian statistics of a passive scalar in turbulent flows," to appear in *Twenty-Seventh Symposium (International) on Combustion* (The Combustion Institute, 1998).
59. K. B. Southerland and W. J. A. Dahm, *A Four Dimensional Experimental Study of Conserved Scalar Mixing in Turbulent Flows*, The University of Michigan Report No. 026779-12 (1994).
60. R. R. Prasad and K. R. Sreenivasan, "Quantitative three-dimensional imaging and the structure of passive scalar fields in fully turbulent flows," *J. Fluid Mech.* **216**, 1 (1990).
61. P. Kailasnath, K. R. Sreenivasan, and J. R. Saylor, "Conditional scalar dissipation rates in turbulent wakes, jets, and boundary layers," *Phy. Fluids. A* **5**, 3207 (1993).
62. B. Yip and M. B. Long, "Instantaneous planar measurement of the complete three-dimensional scalar gradient in a turbulent jet," *Optics Letters* **11**, 64 (1986).
63. M. B. Long and B. Yip, "Measurement of three-dimensional concentration in turbulent jets and flames," in *Twenty-Second Symposium (International) on Combustion* (The Combustion Institute, Pittsburgh, 1988), p. 701.
64. M. S. Mansour, "Two-plane two-dimensional Rayleigh thermometry technique for turbulent combustion," *Optics Lett.* **18**, 537 (1993).
65. S. Corrsin and M. S. Uberoi, "Spectrums and diffusion in a round turbulent jet," *NACA Tech. Note 2124*, 1950.
66. G. K. Batchelor, "Small-scale variation of convected quantities like temperature in a turbulent fluid. Part 1. General discussion and the case of small conductivity," *J. Fluid Mech.* **5**, 113 (1959).
67. D. R. Dowling and P. E. Dimotakis, "Similarity of the concentration field of gas-phase turbulent jets," *J. Fluid Mech.* **218**, 109 (1990).
68. P. L. Miller and P. E. Dimotakis, "Stochastic geometric properties of scalar interfaces in turbulent jets," *Phys. Fluids A* **3**, 168 (1991).
69. A. Brockhinke, P. Andresen, and K. Kohse-Höinghaus, "Quantitative one-dimensional single-pulse multi-species concentration and temperature measurement in the lift-off region of a turbulent H_2/air diffusion flame," *Appl. Phys. B* **61**, 533 (1995).
70. L. L. Smith, R. W. Dibble, L. Talbot, R. S. Barlow, and C. D. Carter, "Laser Raman scattering measurements of differential molecular diffusion in nonreacting turbulent jets of H_2/CO_2 mixing with air," *Phys. Fluids* **7**, 1455 (1995).
71. S. H. Smith and M. G. Mungal, "Mixing, structure and scaling of the jet in a crossflow," *J. Fluid Mech.* **357**, 83 (1999)
72. L. Su and N. T. Clemens, "Measurements of the three-dimensional scalar dissipation rate field in gas-phase planar turbulent jets," *AIAA 97-0074*, Thirty-Fifth Aerospace Sciences Meeting, Reno, NV, Jan. 6-10, 1997.
73. A. Lozano, I. Van Cruyningen, P. Danehy, and R. K. Hanson, "Planar laser-induced fluorescence measurements in a turbulent jet," in *Application of Laser Techniques to Fluid*

Mechanics (Springer-Verlag, Berlin, 1991), p. 19.
74. A. A. Townsend, "On the fine-scale structure of turbulence," *Proc. Royal Soc. (London)* **208A**, 534 (1951).
75. J. C. Wyngaard, "Measurement of small-scale turbulence structure with hot wires," *J. Phys. E: Sci. Instrum.* **1**, 1105 (1968).
76. R. A. Antonia, B. R. Satyaprakash, and A. K. M. F. Hussain, "Measurements of dissipation rate and some other characteristics of turbulent plane and circular jets," *Phys. Fluids* **23**, 695 (1980).
77. A. Noullez, G. Wallace, W. Lempert, R. B. Miles, and U. Frisch, "Transverse velocity increments in turbulent flow using the RELIEF technique," *J. Fluid Mech.* **339**, 287 (1997).
78. C. A. Friehe, C. W. Van Atta, and C. H. Gibson, "Jet turbulence: dissipation rate measurements and correlations," in *Turbulent Shear Flows*, AGARD Conference Proceedings No. 93 (1972), p. 18-1.
79. W. J. A. Dahm and K. A. Buch, "Lognormality of the scalar pdf in turbulent flows," *Phys. Fluids A* **1**, 1290 (1989).
80. A. N. Kolmogorov, "Local structure of turbulence in an incompressible fluid for very large Reynolds numbers," *Dolk. Akad. Nauk. SSSR* **30**, 299 (1941).
81. A. M. Obukhov, "Structure of the temperature field in turbulent flows," *Izr. Akad. SSSR Serv. Georgr. Geofiz.* **13**, 48 (1949).
82. S. Corrsin, "On the spectrum of isotropic temperature fluctuations in isotropic turbulence," *J. Appl. Phys.* **22**, 469 (1949).
83. K. R. Sreenivasan and R. A. Antonia, "The phenomenology of small-scale turbulence," *Annu. Rev. Fluid Mech.* **29**, 435 (1997).
84. K. R. Sreenivasan, "On local isotropy of passive scalars in turbulent shear flows," *Proc. R. Soc. London* **434**, 165 (1991).
85. B. Castaing, G. Gunaratne, F. Heslot, L. Kadanoff, A. Libchaber, S. Thomas, X. Wu, S. Zaleski, and G. Zanetti, "Scaling of hard thermal turbulence in Rayleigh-Bernard convection," *J. Fluid Mech.* **204**, 1 (1989).
86. J. P. Gollub, J. Clarke, M. Grarib, B. Lane, and O. N. Mesquita, "Fluctuations and transport in a stirred fluid with a mean gradient," *Phys. Rev. Lett.* **67**, 3507 (1991).
87. Jayesh and Z. Warhaft, "Probability distribution in grid-generated turbulence," *Phys. Rev. Letters* **67**, 3503 (1991).
88. Jayesh and Z. Warhaft, "Probability distribution, conditional dissipation and transport of passive temperature fluctuations in grid-generated turbulence," *Phys. Fluids A* **4**, 2292 (1992).
89. M. Holzer and E. D. Siggia, "Turbulent mixing of a passive scalar," *Phys. Fluids* **6**, 1820 (1994).
90. A. Pumir, "A numerical study of the mixing of a passive scalar in three dimensions in the presence of a mean gradient," *Phys. Fluids* **6**, 2118 (1994).
91. R. M. McLaughlin and A. J. Majda, "An explicit example with non-Gaussian probability distribution for nontrivial scalar mean and fluctuations," *Phys. Fluids* **8**, 536 (1996).
92. F. A. Jaberi, R. S. Miller, C. K. M. Madina, and P. Givi, "Non-Gaussian scalar statistics in homogeneous turbulence," *J. Fluid Mech.* **313**, 241 (1996).
93. M. R. Overholt and S. B. Pope, "Direct numerical simulation of a passive scalar with imposed mean gradient in isotropic turbulence," *Phys. Fluids* **8**, 3128 (1996).
94. A. M. Obukhov, "Some specific features of atmospheric turbulence," *J. Fluid Mech.* **13**, 77 (1962).
95. J. M. Burgers, "A mathematical model illustrating the theory of turbulence," *Adv. Appl. Mech.* **1**, 171 (1948).

96. J. M. Burgers, "The formation of vortex sheets in a simplified type of turbulent motion," *Proc. Acad. Sci. Amst.* **53**, 122 (1950).
97. A. A. Townsend, "On the fine-scale structure of turbulence," *Proc. R. Soc. London A.* **208**, 534 (1951).
98. A. Y. Kuo and S. Corrsin, "Experiments on internal intermittency and fine-structure distribution functions in fully turbulent flows," *J. Fluid Mech.* **50**, 285 (1971).
99. R. M. Kerr, "Higher-order derivative correlations and alignment of small-scale structures in isotropic turbulence," *J. Fluid Mech.* **153**, 31 (1985).
100. M. M. Rogers and P. Moin, "The structure of the vorticity field in homogeneous turbulent flows," *J. Fluid Mech.* **176**, 33 (1987).
101. W. T. Ashurst, A. R. Kerstein, R. M. Kerr, and C. H. Gibson, "Alignment of vorticity and scalar gradient with strain rate in simulated Navier-Stokes turbulence," *Phys. Fluids* **30**, 2343 (1987).
102. G. R. Ruetsch and M. R. Maxey, "Small-scale features of vorticity and passive scalar fields in homogeneous isotropic turbulence," *Phys. Fluids.* **A3**, 1587 (1991).
103. S. C. Graham, A. J. Grant, and J. M. Jones, "Transient molecular concentration measurements in turbulent flows using Rayleigh light scattering," *AIAA J.* **12**, 1140 (1974).
104. T. M. Dyer, "Rayleigh light scattering measurements of time-resolved concentration in a turbulent propane jet," *AIAA J.* **17**, 912 (1979).
105. H. G. Green, "Developments in signal analysis for laser Rayleigh scattering," *J. Phys. E: Sci. Instrum.* **20**, 670 (1987).
106. W. M. Pitts, "Effects of global density ratio on the centerline mixing behavior of axisymmetric turbulent jets," *Exp. Fluids* **11**, 125 (1991).
107. W. M. Pitts, "Reynolds number effects on the mixing behavior of axisymmetric turbulent jets," *Exp. Fluids* **11**, 135 (1991).
108. M. C. Escoda and M. B. Long, "Rayleigh scattering measurements of the gas concentration field in turbulent jets," *AIAA J.* **21**, 81 (1983).
109. D. A. Everest, J. F. Driscoll, W. J. A. Dahm, and D. A. Feikema, "Images of the temperature field and temperature gradients to quantify mixing rates within a non-premixed turbulent jet flame," *Combust. Flame* **101**, 58 (1995).
110. M. Winter, J. K. Lam, and M. B. Long, "Techniques for high-speed digital imaging of gas concentrations in turbulent flows," *Expts. Fluids* **5**, 177 (1987).
111. W. M. Pitts, "Development of a line camera system for real-time measurements of concentration in turbulent flow fields," in *Proceedings of the Flow and Particles Diagnostics, LIA Volume 58* (The Laser Institute of America, Toledo, 1987), p. 7.
112. K. C. Muck, J. M. Wallace, and W. M. Pitts, "Simultaneous real-time line measurements of concentration and velocity in turbulent flows," in *Application of Laser Techniques to Fluid Mechanics* (Springer-Verlag, Berlin, 1991), p. 80.
113. N. Bryner, C. D. Richards, and W. M. Pitts, "A Rayleigh light scattering facility for the investigation of free jets and plumes," *Rev. Sci. Instrum.* **63**, 3629 (1992).
114. Y. S. Touloukian, S. C. Saxena, and P. Hestermans, *The Thermophysical Properties of Matter Vol. 11, Viscosity* (IFE/Plenum, New York, 1975).
115. N. R. Panchapakesan and J. L. Lumley, "Turbulence measurements in axisymmetric jets of air and helium," *J. Fluid Mech.* **246**, 197 (1993).
116. C. R. Wilke, "A Viscosity equation for gas mixtures," *J. Chem. Phys.* **18**, 517 (1950).
117. R. F. Barr and H. Watts, "Diffusion of some organic and inorganic compounds in air," *J. Chem. Eng. Data* **17**, 45 (1972).
118. G. Strang, "Wavelet transforms versus Fourier transforms," *Bull. Am. Math. Soc.* **28**, 288 (1993).

119. I. Daubechies, *Ten Lectures on Wavelets* (SIAM, Philadelphia, PA, 1992).
120. M. S. Levenson, "Removing quantization noise in images using wavelets," *ASA Proc. Sect. Phys. Eng. Sci.* (American Statistical Assoc., Alexandria, VA, 1996), p. 193.
121. D. L. Donoho and I. M. Johnstone, "Ideal spatial adaptation by wavelet shrinkage," *Biometrika* **81**, 425 (1994).
122. A. Bruce and H. Gao, *S+ Wavelets User's Manual* (MathSoft, Inc., Seattle, WA, 1994).
123. J. Mi and R. A. Antonia, "Corrections to Taylor's hypothesis in a turbulent circular jet," *Phys. Fluids* **6**, 1548 (1994).
124. W. J. A. Dahm and K. B. Southerland, "Experimental assessment of Taylor's hypothesis and its applicability to dissipation estimates in turbulent flows," *Phys. Fluids* **9**, 2101 (1997).
125. D. R. Dowling, *Mixing in Gas Phase Turbulent Jets*, Doctor of Philosophy Thesis, California Institute of Technology, 1988.
126. D. R. Dowling and P. E. Dimotakis, "On mixing and structure of the concentration field of turbulent jets," *Proceedings of the First National Fluid Dynamics Congress* (AIAA, New York, 1988), p. 982.
127. I. Wygnanski and H. Fiedler, "Some measurements in the self-preserving jet," *J. Fluid Mech.* **38**, 577 (1969).
128. C. H. Gibson, C. C. Chen, and S. C. Lin, "Measurements of turbulent velocity and temperature fluctuations in the wake of a sphere," *AIAA J.* **6**, 642 (1968).
129. R. H. Magarvey and C. S. MacLatchy, "The formation and structure of vortex rings," *Can. J. Phys.* **42**, 678 (1964).
130. T. Maxworthy, "The structure and stability of vortex rings," *J. Fluid Mech.* **51**, 15 (1972).
131. T. Maxworthy, "Some experimental studies of vortex rings," *J. Fluid Mech.* **81**, 465 (1977).
132. J. E. Broadwell, W. J. A. Dahm, and M. G. Mungal, "Blowout of turbulent diffusion flames," in *Twentieth Symposium (International) on Combustion* (The Combustion Institute, Pittsburgh, 1984) p. 303.
133. R. Chevray, "Entrainment in turbulent flows: Mechanisms and implications," in *Turbulence and Chaotic Phenomena in Fluids* (Elsevier Science Publishers, New York, 1984, T. Tatsumi (Ed.)), p. 365.
134. M. C. Drake, R. W. Pitz, and W. Shyy, "Conserved scalar probability density functions in a turbulent jet diffusion flame," *J. Fluid Mech.* **171**, 27 (1986).
135. E. Effelsberg and N. Peters, "A composite model for the conserved scalar PDF," *Combust. Flame* **50**, 351 (1983).
136. A. R. Kerstein, R. W. Schefer, and M. Namazian, "A conditional similarity concept for turbulent shear flow, with application to mixing in a round jet," *Phys. Fluids* **6**, 642 (1994).
137. G. K. Batchelor and A. E. Gill, "Analysis of the stability of axisymmetric jets," *J. Fluid Mech.* **14**, 529 (1962).
138. W. J. A. Dahm, P. E. Dimotkis, and J. E. Broadwell, "Nonpremixed turbulent jet flames," *AIAA Paper* 84-0369 (AIAA, New York, 1984).
139. R. W. Schefer and R. W. Dibble, "Rayleigh scattering measurements of mixture fraction in a turbulent nonreacting propane jet," *Sandia Report SAND85-8837* (November, 1985).
140. G. K. Batchelor and A. A. Townsend, "The nature of turbulent motion at large wave-numbers," *Proceed. Roy. Soc. A* **199**, 238 (1949).
141. A. Y.-S. Kuo and S. Corrsin, "Experiments on internal distribution functions in fully turbulent fluid," *J. Fluid Mech.* **50**, 285 (1971).
142. B. F. Magnussen, "An investigation into the behavior of soot in a turbulent free jet C_2H_2-flame," in *Fifteenth Symposium (International) on Combustion* (The Combustion Institute, Pittsburgh, 1975), p. 1415.

143. B. F. Magnussen, B. H. Hjertager, J. G. Olsen, and D. Bhaduri, "Effects of turbulent structure and local concentrations on soot formation and combustion in C_2H_2 diffusion flames," in *Seventeenth Symposium (International) on Combustion* (The Combustion Institute, Pittsburgh, 1979), p. 1383.
144. C.-H. P. Chen and R. F. Blackwelder, "Large-scale motion in a turbulent boundary layer: a study using temperature contamination," *J. Fluid Mech.* **89**, 1 (1978).
145. R. S. Burlington and D. C. May, Jr., *Handbook of Probability and Statistics with Tables* (McGraw-Hill, New York, 1970), pp. 123-124.
146. A. A. Townsend, *The Structure of Turbulent Shear Flow*, (Cambridge University Press, Cambridge, 1976), pp.339-340.
147. R. A. Antonia, A. J. Chambers, D. Britz, and L. W. B. Browne, "Organized structures in a turbulent plane jet: topology and contribution to momentum and heat transport," *J. Fluid Mech.* **172**, 211 (1986).
148. R. A. Antonia and L. W. B. Browne, "Assessment of local isotropy using measurements in a turbulent plane jet," *J. Fluid Mech.* **163**, 67 (1983).